# ELECTROHYDRODYNAMIC (EHD) DROPLET FORMATION, DISPERSION AND MASS TRANSFER IN A VISCOUS DIELECTRIC LIQUID

By

WUHAI HE, M.ENG.

A Thesis
Submitted to the School of Graduate Studies
in Partial Fulfilment of the Requirements
for the Degree
Doctor of Philosophy

McMaster University

# ELECTROHYDRODYNAMIC (EHD) DROPLET FORMATION, DISPERSION AND MASS TRANSFER

DOCTOR OF PHILOSOPHY (1993) McMASTER UNIVERSITY

(Chemical Engineering) Hamilton, Ontario

TITLE: Electrohydrodynamic (EHD) Droplet Formation, Dispersion and Mass Transfer in a Viscous Dielectric Liquid

AUTHOR: WUHAI HE

DIPL.CHEM.ENG. (Zhejiang University, China)

M.ENG. (Institute of Fragrance and Flavor Industry, China)

SUPERVISORS: DR. MALCOLM H.I. BAIRD

DR. JEN-SHIH CHANG

NUMBER OF PAGES: xxi, 206

# Abstract

Electrohydrodynamics (EHD) is an interdisciplinary engineering science which has been known for more than a century and has been more intensively developed in last two decades with the concern of the interaction between electric fields and fluids. The investigations of EHD droplet formation, dispersion and mass transfer in a viscous dielectric liquid are the main subjects of study for mass transfer enhancement in liquid-liquid extraction operations by an imposed DC electric field.

The droplet formation and dispersion of water in a high viscosity mineral oil have been studied at the conditions of low droplet Reynolds numbers with and without the presence of an electric field. The droplets formed at a hollow electrode with uniform size and spherical shape have been observed; the droplet size reduction and mutual repulsion can be controlled by the applied voltages. The droplet velocity near the hollow electrode is also significantly enhanced in the presence of the non-uniform DC electric field. The model for EHD droplet formation has been derived with the inclusion of electric force component based on the force balance upon droplet detachment from the hollow electrode.

Mass transfer of benzoic acid from droplets in this two-phase liquid-liquid system has been studied with and without the presence of an imposed DC non-uniform electric field. Total mass transfer efficiency can be significantly enhanced in the presence of the applied electric field. The results obtained from droplet mass transfer investigation indicate that the mass transfer mechanisms of these electrically

charged droplets during the droplet formation and its subsequent free fall are similar to those of droplets in the absence of electric field and these results can be correlated using the existing mass transfer models. The increased specific interfacial area and the accelerated drop initial velocity in the presence of electric field are the main contributions to the enhanced efficiency of mass transfer in the present investigation.

In parallel to the experimental investigations, the numerical modelling of electric field profiles inside the experimental cell has been performed based on the axial symmetric approximation and with the appropriate coordinate transformations. A finite difference algorithm with the control volume approach has been used to conduct numerical calculations. The numerical results obtained from the electric field profiles and predictions of the EHD force components on the droplet can provide much useful information to support the results obtained from experimental investigation.

The mechanisms of electric field induced current flow and electrification of droplets during EHD droplet formation and dispersion have been postulated and discussed based on the observed current-voltage characteristics of the system, the electric charge acquired by the droplet and the results from numerical electric field modelling.

The mechanism of EHD droplet formation and dispersion from hollow electrode is proposed based on the modified Vonnegut & Neubauer model where an effective dielectric constant of a liquid-liquid two-phase system has been defined. The electrically charged droplets formed at hollow electrode under high electric field intensity would all reach their maximum charge limit which determines and controls the uniform size of dispersed multi-droplets. Then the EHD force generated at high electric field intensity would contribute to the dispersion and acceleration of these electrically charged droplets. Thus the initial velocities of these droplets are significantly enhanced.

# Acknowledgements

The author would like to express his sincere gratitude to those who have contributed, in one way or another, to the successful completion of this thesis. He is particularly indebted to: his research supervisors, Dr. M.H.I. Baird and Dr. J.S. Chang for their insight, encouragement and profound advice and interest throughout the course of this study; his Ph.D. supervisory committee member, Dr. R. H. Pelton for providing encouragement and help; the fellow graduate students and researchers in both Dr. Baird's group and Dr. Chang's group whom he has had the pleasure of working with over the years; his wife, Minhua, for her understanding, support and forbearance throughout the study.

The author is also grateful for being selected as a recipient of Sherman Graduate Scholarship, Shell Canada Graduate Research Fellowship and the Yates Scholarship Fund during the period of his thesis study. This project is supported by the Natural Sciences and Engineering Research Council of Canada.

# Contents

# List of Figures

# List of Tables

# List of Notation

Except where otherwise specified the following symbols are used throughout this thesis.

## Roman

| | |
|---|---|
| $a$ | droplet radius, or the length defined in Appendix B, [m] |
| $a_i$ (i = E, W, S, N) | coefficients in numerical model defined in Equation (4.38) |
| $A$ | function defined in Equation (4.43) |
| $A_{av}$ | time averaged drop surface area for the duration of its forming, [$m^2$] |
| $b$ | the length defined in Appendix B, [m] |
| $B$ | constant defined in Equation (4.20) |
| $C_D$ | coefficient of viscous drag |
| $C_i$ (i=0, 1, 2, 3) | drop phase benzoic acid concentration, [$kg/m^3$] |
| $C^*$ | equilibrium benzoic acid concentration in drop phase, [$kg/m^3$] |
| $C$ | constant defined in Equation (7.15), [$s^{-1/2}$] |
| $C'$ | constant defined in Equation (7.21), [$s^{-1/2}$] |
| $d$ | droplet diameter, [m] |
| $d_0$ | outside diameter of hollow nozzle (electrode), [m] |
| $d_e$ | minimum droplet diameter limit at zero flow rate, [m] |
| $d_t$ | instant droplet diameter during formation period, [m] |

| | |
|---|---|
| $D_i$ (i=e, w, s, n) | functions derived for numerical model, see Equations (4.44)-(4.47) |
| $\mathcal{D}_i$ (i=c, d) | molecular diffusivity of benzoic acid, [$m^2/s$] |
| $\mathcal{D}_e$ | charge diffusion constant, [$m^2/s$] |
| $\mathbf{D}$ | electric displacement, [$C/m^2$] |
| $e$ | electronic charge ($= 1.602 \times 10^{-19}$ [$C$]) |
| $E_i$ (i=t, df, ff, dc) | drop mass transfer efficiency |
| Eo | Eötvös number, $g\Delta\rho d^2/\sigma$ |
| $\mathbf{E}$, $\mathbf{E}_i$ (i=c, d) | electric field intensity, [V/m] |
| $\mathbf{E}_0$ | the electric field intensity at $\eta_0$, defined in Appendix B, [V/m] |
| $f$ | drop forming frequency, [$s^{-1}$] |
| $\mathbf{f}_e$, $\mathbf{f}_{e1}$, $\mathbf{f}_{e2}$ | electrohydrodynamic (EHD) forces density, [$N/m^3$] |
| $F_i$ (i=e, w, s, n) | functions derived for numerical model, see Equations (4.48)-(4.51) |
| $\mathbf{F}_i$ (i=d, g, s, eg) | force component on the forming drop, [N] |
| $\mathbf{F}_{stokes}$ | drag force on the drop moving steadily, [N] |
| $\mathbf{g}$, $g$ | gravity, [$m/s^2$] |
| $H$ | distance for drop free fall in the continuous phase, [m] |
| $I$, $I_a$, $I_b$ | electric current measured at hollow electrode, [A] |
| $\mathbf{I}$ | unit tensor |
| $\mathbf{J}$ | electric charge flux or current density, [$C/m^2 \cdot s$] or [$A/m^2$] |
| $k$ | Boltzmann constant ($= 1.381 \times 10^{-23}$ [J/K]) |
| $k_c$ | film mass transfer coefficient based on continuous phase, [m/s] |
| $K_i$ (i=df, ff, od) | overall mass transfer coefficient based on dispersed phase, [m/s] |
| $l$ | the length defined in Appendix B, [m] |
| $L_1, L_2, L_3$ | the lengths defined in Chapter 4 (see Figure 4.2), [m] |
| $m$ | equilibrium distribution constant of benzoic acid concentration |
| $m_d$ | mass of the formed droplet, [kg] |
| M | Morton number, $g\mu^4\Delta\rho/\rho^2\sigma^3$ |
| $p$, $p_i$ (i=d, e, p, s) | pressure terms, [$N/m^2$] |

| | |
|---|---|
| $\mathbf{p}$ | electric field induced polarization, [C/m$^2$] |
| $P_i$ (i=e, w, s, n) | functions derived for numerical model, see Equations (4.39)–(4.42) |
| $\mathrm{Pe}_c$ | droplet Peclet number based on continuous phase, $dv_t/\mathcal{D}_c$ |
| $q$ | electric charge acquired on the forming droplet, [C] |
| $Q$ | drop phase flow rate, [m$^3$/s] |
| $Q'$ | dimensionless drop phase flow rate, defined in Equation (5.39) |
| r, $r$ | radial direction in cylindrical or spherical coordinates |
| $r_1, r_2$ | the radius defined in Chapter 4 (see Figure 4.1), [m] |
| $\bar{\mathrm{r}}$, $\bar{r}$ | transformed radial coordinate for numerical simulation |
| $R$ | universal gas constant, relative mass transfer efficiency |
| $\mathrm{Re}_d$ | droplet Reynolds number based on continuous phase, $d\,v_t/\nu_c$ |
| $s$ | charge decay coefficient defined in Equation (4.64) |
| $S$ | drop moving distance during its forming stage, [m] |
| $\mathrm{Sc}_c$ | droplet Schmidt number based on continuous phase, $\nu_c/\mathcal{D}_c$ |
| Sh | droplet Sherwood number based on continuous phase, $k_c\,d/\mathcal{D}_c$ |
| $t, t_i$ (i=df, ff) | instant of time during drop formation, droplet durations, [s] |
| $T$ | absolute temperature, [K] |
| $\mathbf{T}_e$ | electric stress tensor, [N/m$^2$] |
| $U_{tip}$ | measured drop velocity near the tip of hollow electrode, [m/s] |
| $\mathbf{U}$ | fluid velocity field, [m/s] |
| $v_0$ | undisturbed velocity far away from a rigid sphere or drop, [m/s] |
| $v_r$, $v_\theta$ | velocity components in spherical coordinates, [m/s] |
| $v_t$ | drop terminal velocity, [m/s] |
| $V$, $V_0$ | applied electric voltage, [V] |
| $V'$ | dimensionless drop volume, defined in Equation (5.40) |
| $V_i$ (i=d, av) | droplet volume, [m$^3$] |
| $W$ | distance between two consecutive drops, [m] |
| z, $z$ | axial direction in cylindrical coordinates |

| | |
|---|---|
| $\bar{z}$, $\bar{\bar{z}}$ | transformed axial coordinate |
| $\mathcal{Z}$ | dimensionless constant defined in Equation (7.14) |
| $A$, $B$, $C$, $D$, | constants defined in Equation (5.8) |

## Greek

| | |
|---|---|
| $\beta$ | stretch constant in axial coordinate transformation |
| $\gamma$ | surface tension, [N/m] |
| $\varepsilon$, $\varepsilon_i$ (i=c, d) | dielectric constant, [F/m] |
| $\varepsilon_0$ | dielectric constant of free space ($= 8.854 \times 10^{-12}$ [F/m]) |
| $\varepsilon_s$ | specific dielectric constant (relative permittivity), $\varepsilon = \varepsilon_s \cdot \varepsilon_0$ |
| $\varepsilon_{eff}$ | effective dielectric constant defined in Equation (2.17), [F/m] |
| $\eta$, $\eta_0$ | prolate spheroidal coordinates |
| $\theta$ | inclination angle of the hollow electrode, [°] |
| $\theta'$ | inclination angle of the resultant force, $F_{eg}$, [°] (see Figure (6.2)) |
| $\kappa$ | ratio of the viscosities, $\mu_d/\mu_c$ |
| $\mu$, $\mu_i$ (i=c, d) | dynamic viscosity, [Pa · s] |
| $\mu'$ | dimensionless viscosity, defined in Equation (5.41) |
| $\mu_e$ | ionic mobility, [$m^2/V \cdot s$] |
| $\nu$ | kinematic viscosity, [$m^2/s$] |
| $\pi$ | $= 3.1415\cdots$ |
| $\rho$, $\rho_i$ (i=c, d) | mass density, [$kg/m^3$] |
| $\rho_e$ | net volume electric charge density, [$C/m^3$] |
| $\rho_{ed}$ | electric charge density based on drop volume, [$C/m^3$] |
| $\rho_{ei}$ | local electric charge density, [$C/m^3$] |

| | |
|---|---|
| $\sigma$ | interfacial tension, [N/m] |
| $\tau$ | stretch constant in radial coordinate transformation |
| $\phi$, $\phi_0$ | electric potential, [V] |
| $\psi$, $\psi_d$ | stream function |
| $\eta$, $\theta$, $\Psi$ | prolate spheroidal coordinates |

## Subscript

| | |
|---|---|
| 0, 1, 2, 3 | drop phase at the various stages as defined in Chapter 7 |
| *av* | time averaged value for the duration of drop formation |
| *c* | continuous phase |
| *d* | dispersed phase, due to viscous drag |
| *dc* | during drop coalescence period |
| *df* | during drop formation period |
| *e* | electric field applied |
| *eg* | due to combined gravity and electric field |
| *ff* | during drop free fall period |
| *g* | due to gravity |
| *n* | normal component |
| *od* | over all and based on drop phase |
| *p* | polarization |
| *s* | electrostrictive, due to interfacial tension |
| *t* | total, tangential component |
| P, E, W, N, S | representing the present point and its four neighbouring grid points |
| *e*, *w*, *n*, *s* | representing the four boundaries of the control volume |

# Chapter 1

# Introduction

## 1.1 Background and Origins of the Subject

In chemical processing industry, the efficiency of the operation performance is generally based either on the energy input or on the external forces applied. The majority of conventional chemical processing operations applies mechanical or thermal energy in combination with pressure or gravity forces. The application of superimposed electric fields to improve several separation processes has been well known and also widely used for many years (He and Chang, 1993). The familiar industrial applications range from solid-solid separation in the beneficiation of ores in the mining industry, cleaning of exhaust gases from solid particles in energy and other industries, to coalescence of "water-in-oil" emulsions in the petroleum industry. Recently, an extensive effort has been directed to explore the potential application of using electric fields to enhance mass transfer efficiency in liquid-liquid extraction processes.

### 1.1.1 Fundamentals of liquid-liquid extraction

*Liquid-liquid extraction*, some times known as *solvent extraction* or merely *extraction*, is a separation process that depends on the transfer of the component to be separated (the consolute component) from one liquid phase to a second liquid phase which is immiscible or partially miscible with the first. Applications of liquid-liquid extraction fall into several categories: those where extraction is in direct competition with other separation methods and those where it seems uniquely qualified (Treybal, 1980).

The laboratory technique of liquid-liquid extraction has been known for over a century. Basically, the feed solution is shaken with the solvent until equilibrium is reached, then the two liquid phases are allowed to settle into two clear layers which can be separated. The whole operation is carried out batchwise. When liquid-liquid extraction began to be applied widely in processing industries, continuous operation superseded batch operation. Industrial application of liquid-liquid extraction has increased rapidly over the last 50 years. The unique ability of liquid-liquid extraction to achieve separation according to chemical type rather than physical characteristics has led to its broad application in processing industries which range from nuclear fuel enrichment and reprocessing to fertilizer manufacture, and from petroleum refining to food processing. Research and development in hydrometallurgical extraction processes have been continued on the extraction of non-ferrous metals such as copper, nickel, cobalt *etc.* using new commercially-developed extraction reagents. More recently, liquid-liquid extraction has been used in many environmental applications, both for the economic recovery of valuable materials from waste streams and for treatment to comply with statutory requirements (Lo and Baird, 1980; Lo *et al.*, 1983).

Whether an extraction process is carried out in the laboratory or industry, it always involves contact of the liquid phases with an approach towards equilibrium, and separation of the contacted liquid phases. Equilibrium is one of the most important

aspects of liquid-liquid extraction fundamentals. For a given system, equilibrium sets the thermodynamic limits of the extraction process. The rate at which equilibrium is reached in a liquid-liquid system usually depends strongly on specific interfacial area, since liquid-liquid extraction involves direct contact between a dispersed phase in the form of droplets and another immiscible liquid in the form of continuous phase. Like many other chemical engineering unit operations, the mass transfer rate in liquid-liquid extraction is therefore proportional to the specific interfacial area and to the overall mass transfer coefficient.

### 1.1.2 Potential applications of electrohydrodynamic (EHD) techniques in liquid-liquid extraction

Electrohydrodynamics abbreviated EHD is the engineering science of the interaction between electric fields and fluids. Many of the most interesting problems in EHD involve both an effect of the fluid motion on the applied electric fields and an influence of the applied electric fields on the fluid motion.

Interaction of drops, bubbles and particles with electric fields is prevalent in nature and is important in many technological applications (Moore, 1973; Crowley, 1986; Cross, 1987; Chang, 1988). Electric fields have already been used in applications related to separation processes for many years. One of the earliest and best known applications are the removal of particles from the gas phase and the coalescence of the fine water droplets in the crude oil emulsions (Waterman, 1965; Moore *et al.*, 1973; Crowley, 1986; Cross, 1987). The use of electric fields was also contemplated as a means of improving liquid-liquid extraction processes (Stewart and Thornton, 1967; Thornton, 1968). More recently the effects of electric fields upon liquid-liquid systems have been increasingly the focus of research mainly to investigate the electric forces effects on droplet formation, dispersion, oscillation and break up, as well as effects on liquid-liquid mass transfer. Among the large amount of published work, several

review papers and short articles have summarized most of the research carried out to date (Thornton, 1968; Baird, 1983; Chang, 1987; Scott, 1989; Weatherley, 1992; Ptasinski and Kerkhof, 1992).

The application of an electric field in a liquid-liquid extraction process is expected to increase the specific interfacial area and to enhance the mass transfer coefficient as well, with the enhancement in terms of energy input much more efficient than other methods. The general idea of directly using an electric field to improve the performance of mass transfer in liquid-liquid extraction was initially described by Stewart and Thornton (1967). As emphasized by Scott (1989), recent results in this area suggest that liquid-liquid extraction driven by electric field may produce systems that are an order of magnitude more effective than the traditional means.

Although there is so far no industrial scale application of electrically enhanced mass transfer in liquid-liquid extraction (Scott, 1989; Weatherley, 1992), investigations on some industrially related systems have been carried out. For example, extraction of nickel, copper, uranium and rare earths (Bailes, 1977, 1981; Bailes and Wade, 1980; Martin *et al.*, 1983; Hund and Lancelot, 1986), and extraction of penicillin G and other products from whole fermentation broths (Millar and Weatherley, 1989; Weatherley *et al.*, 1990) have been reported.

## 1.2 Review of the Previous Work

### 1.2.1 Droplet formation and dispersion under electric fields

#### Behaviour of droplet in the presence of electric fields

When an electric field is applied across a dielectric fluid medium, in which a droplet of a conductive liquid is suspended, the droplet behaviour will be influenced by the

applied electric field. Taylor (1964), Garton and Krasucki (1964) have shown that a neutral droplet immersed in a dielectric liquid in DC electric field elongates due to polarization in a nearly prolate spheroid shape, whose major axis lies parallel to the electric field lines. Another kind of electrostatic disintegration can also occur when a droplet acquires charge, for example, by contacting a charged electrode. Rayleigh (1882) showed that a charged drop in the air becomes unstable if the charge on the drop exceeds the critical charge limit, and the unstable drop ejects some charged daughter drops.

Many investigations have been conducted (Thornton, 1968; Bailes and Thornton, 1971; Takamatsu *et al.*, 1981; 1982; 1983a, b; Perona and Byers, 1987; Byers and Perona, 1988) on droplet formation at nozzles or orifices which are connected to a high voltage source and immersed in dielectric liquids. The force balance during drop formation may be satisfied by the interfacial tension, gravitational, and electrostatic forces, although inertial forces must also be considered at high rates of formation. At the drop interface, the tangential stress component must be balanced by viscous shear stress due to droplet surface motion (Allan and Mason, 1962; Taylor, 1966). If the electric field strength is low and the electrostatic and gravitational forces act in the same direction, single drops are formed with smaller volume than those formed at the no-field condition. At high field strength the electric stresses can dominate and the discrete droplet regime is changed into the dispersion-regime (jetting) and a continuous stream of very small droplets is produced (Bailes, 1981).

The second method of droplet generation is the direct use of strong electrical stresses to rupture a liquid-liquid interface. High-intensity pulsed electric fields are most efficient for the creation of a very large interfacial area by means of droplet rupture into extremely small size droplets, even as small as 5 $\mu m$ (Scott, 1987; Scott and Sisson, 1988).

Another approach to a direct liquid dispersion is based on the electric field

induced instability of a flat liquid-liquid interface (Yoshida *et al.*, 1986; 1988). The dispersion of a water phase has been achieved from a water film which flowed down an inclined plate electrode into a continuous dielectric liquid phase.

### Single droplet formation from a nozzle electrode under uniform DC electric field

The experimental techniques for single droplet formation in a dielectric fluid under high voltage DC uniform electric field are basically almost the same as reported by several investigators (Stewart and Thornton, 1967; Bailes and Thornton, 1971; Harker and Ahmadzadeh, 1974; Tsukada *et al.*, 1987; Takamatsu *et al.*, 1982; Carleson and Fuller, 1987). An apparatus is arranged with parallel flat plate electrodes geometry and a nozzle for droplet formation. The electric field is produced by connecting a high voltage DC power supply unit to the upper electrode and nozzle, and maintaining the lower electrode at zero potential, although sometimes the opposite arrangement was used (Austin *et al.*, 1971; Freeman and Laurizio, 1986). Both the electrode separation distance (or electrode gap distance) and the applied voltage can be varied so that the droplet size can be controlled. The typical gap distance is only about 5 cm. The interaction of the electrically charged drop with the applied electric field results in an electrical body force acting in the same direction as gravity and generates smaller drops. Several investigations observed a reduction in droplet size with increasing field strength. This can be explained by considering the force balance on the forming droplet. It is noted that there are differences between the derived force balances in droplet formation given by different investigators, due to different approximations of the droplet formation process.

### Single droplet formation from a nozzle electrode under non-uniform electric fields

The formation of a single droplet in a liquid-liquid two-phase system under non-uniform electric fields has been studied by few investigators (Takamatsu *et al.*, 1983a; Byers and Perona, 1988) due to the far more complex nature of the non-uniform field compared to the uniform case.

According to Takamatsu and his co-worker (1983a), droplet sizes generated under the non-uniform field are much smaller than those under the uniform field at the same value of applied voltage. This means that the efficiency of use of electrical energy for drop formation under a non-uniform field is higher than that in the uniform field, due to the field strength around a pendant drop being extremely enhanced in the former situation. These authors carried out a theoretical analysis based on many assumptions as well as providing an empirical correlation for the droplet volume. Based on their results the theoretical predictions are not as good as the empirical correlations, but the empirical expressions only can be applied in their restricted situations, and for the particular system used.

### Effect of applied electric field on the droplet velocity

Once the droplet has detached from the nozzle, its motion is also influenced by the applied electric field. A considerable enhancement in droplet velocity due to the additional electric forces has been observed. The forces causing the droplet motion are opposite in direction to those due to drag. The force balance for a droplet moving steadily in another liquid under the effect of an electric field has also been investigated (Bailes, 1981; Yang and Carleson, 1990; Vu and Carleson,1986; Takamatsu *et al.*, 1983b).

Two correlation models based on the balance of forces have been proposed

(Yang and Carleson, 1990; Vu and Carleson, 1986). Another approach was proposed by Takamatsu *et al.* (1983b), who successfully correlated their results using the Hu-Kintner empirical model (Hu and Kintner, 1955), in which the effective density and effective interfacial tension were used for correlating the charged droplet velocity, instead of the physical density and physical interfacial tension.

### 1.2.2 Electric field effect on liquid-liquid mass transfer

#### Specific interfacial area enhanced by imposed electric fields

The majority of studies on enhancing interfacial area using electric fields has been devoted to the droplet formation and dispersion of relatively conductive droplets in dielectric liquids, as summarized above. The drops formed at a nozzle or orifice will acquire a certain amount of induced charge on the droplet which depends on the imposed electric field strength and the geometries of the electrode. The droplet size is determined by the balance of interfacial tension, gravitational, electrical and drag forces. Since the additional electrical forces act on the opposite direction to the interfacial tension forces, the result is the formation of droplets with reduced size. Therefore, for the same flow rate of dispersed phase through the nozzle or orifice, the smaller but more numerous drops give a larger specific interfacial area. In addition, depending upon the charge density and the field strength, a wide range of drop sizes can be produced from the same nozzle (Bailes, 1981).

#### Enhancement of mass transfer coefficient by electric fields

It is generally known that the mass transfer coefficient depends on the physicochemical properties of a system, as well as on the hydrodynamic state at the liquid-liquid interface. The available theoretical analyses suggest that the enhancement of the mass transfer coefficient is mainly due to a higher degree of turbulence within and

around dispersed droplets as the result of the interactions between the electric field and the interface. On the other hand, the effect of electric fields on the reduction of interfacial tension of a system has also been investigated (Iyer and Sawistowski, 1974; Sato and Saki, 1976), although the electric field effects on other physicochemical properties of a system have usually been ignored.

Theoretical and experimental investigations have shown that interfacial instability and interfacial turbulence can be induced by means of an electric potential gradient. Most of the results were obtained from the systems of low viscous continuous phase and some of the studies were merely based on the numerical simulations without experimental verification. The mechanisms which have been suggested are all based on promotion of interfacial motion by the presence of an electric field as summarized below:

- higher droplet velocities resulting from electric forces of repulsion exerted on the charged drops in the direction of motion (Thornton, 1968; Bailes, 1981; Takamatsu *et al.*, 1983b; Yamaguchi *et al.*, 1985; Vu and Carleson, 1986);
- enhanced circulation inside and around droplets due to the tangential component of the electric forces exerted on the droplet surface (Morrison, 1977; Griffiths and Morrison, 1979; Chang *et al.*, 1982; Chang and Berg, 1983);
- droplet oscillations induced by electric field due to the droplet deformation effect (Thornton, 1976; Wham and Byers, 1987; Scott and Byers, 1989; Basaran *et al.*, 1989; Scott *et al.*, 1990; Yang and Carleson, 1991);
- flow induced by the local variations in the effective interfacial tension due to the presence of space charges on the droplet (Austin *et al.*, 1971; Iyer and Sawistowski, 1974; Carleson and Berg, 1984; Chang and Berg, 1985a; 1985b; Carleson and Fuller, 1987).

## 1.3 Objective and Scope of the Present Work

In spite of the potential advantages of the application of electric field in liquid-liquid extraction processes, only rather limited theoretical studies have been conducted on the subject. Most of the work was conducted in a uniform electric field either confined to the interpretation of total mass transfer performance or restricted to the discrete droplet regime; and all systems selected had low viscosities. In most cases, therefore, the mechanisms of electrically enhanced mass transfer were still not clearly understood and the reported results were very much system dependent.

The work reported in this thesis is mainly to study the effect of a non-uniform DC electric field on a liquid-liquid two-phase system of which the dispersed phase is relatively electric conductive (distilled water) while the continuous phase is relatively viscous and dielectric (mineral oil). Benzoic acid has been used as a mass transfer species which is initially quantitatively dissolved into the dispersed phase, with the mass transfer direction towards the continuous phase. The objective of this work is to gain a better understanding of electrohydrodynamics (EHD) in a liquid-liquid two-phase system as well as EHD enhanced liquid-liquid mass transfer effects. This will include investigations on EHD droplet formation, dispersion and mass transfer in a quiescent dielectric continuous phase with high viscosity under an imposed non-uniform electric field. The research work has been carried out through the following approaches:

- First, experimental investigation on droplet formation, motion and mass transfer has been conducted in the absence of electric field. Attention has been concentrated on the low dispersed phase flow rate region where discrete droplets form directly at the hollow electrode tip and the droplet Reynolds number is low, in the creeping flow mode. Since the hydrodynamics of low Reynolds number flow is already well understood, the results obtained from this investigation

can be thought of as the background with which the results with the electric field applied can be compared.

- Then, experimental investigation on droplet formation, dispersion and mass transfer has been conducted in the presence of electric field. In addition to the droplet size and velocity, the mass transfer efficiency and the electrical parameters, attention has also been focused on the drop size uniformity, since this not only simplifies data analysis but also provides a special feature for the potential industrial applications.

- In parallel to the experimental investigations, numerical modelling on electric field distribution inside the experimental cell and prediction of the EHD force components on droplet have also been carried out, since it is impossible to measure the electric potential distribution experimentally without interference of the field.

The main independently varied parameters involved in this investigation are the dispersed phase flow rate, inclined angle of the hollow nozzle (as hollow electrode when electric field is applied), diameter of the hollow nozzle, the original concentration of benzoic acid in the dispersed phase, the applied electric voltage and the connection mode of the electrodes.

## 1.4 Thesis Summary

Chapter Two presents the fundamentals of quasi-electrostatics and dielectric fluids which follow from Maxwell's equations and the principles of conservation with appropriate constraints:

- magnetic induction is negligible;

- Joule heating and energy dissipation effects are ignored;
- dielectric fluids are linear, incompressible, Newtonian with uniform material properties;
- bulk charge density is zero therefore the Laplace's equation can be used to solve the electric potential as well as electric field.

Chapter Two provides the theoretical background of electrohydrodynamics (EHD) and the basic equations of EHD from which the EHD forces acting on a spherical drop are derived with the effective permittivity being introduced. The maximum charge acquired on a drop in the EHD drop formation process is also discussed and an equation based on "Rayleigh instability limit" is suggested. These fundamental concepts and equations will be discussed and used in the following several chapters.

Chapter Three describes the apparatus and procedures for the experimental investigations. The parameters being measured and the system properties are also included in this chapter.

The numerical modelling of electric field in the experimental cell and the prediction of EHD forces acting on the droplet are the main subjects of Chapter Four. The numerical field model has been derived from the equations in Chapter Two and from the experimental conditions in Chapter Three with the axial symmetric assumption and with the appropriate coordinate transformations. A finite difference algorithm with the control volume approach has been used to conduct numerical calculations. The numerical results are also compared with the approximate analytical models. The results of the numerical modelling are later used and discussed in Chapters Six and Seven along with the experimental results in order to understand the mechanisms and draw some conclusions of EHD enhanced droplet dispersion and mass transfer.

The main subject of Chapter Five is the formation and motion of a single droplet in a high viscosity continuous phase in the absence of electric field. Since none of the models currently available for droplet formation can be selected to use in this work with confidence, new models have been derived based on the force balance.

Chapter Six has mainly focussed on the droplet hydrodynamics under an imposed electric field. Both drop size and velocity were experimentally determined. The model for droplet formation has been derived based on the inclusion of electric force in the model described in Chapter Five. The current-voltage characteristics of the system, and the electric charge acquired by the droplet during formation and its subsequent dispersion are also presented in this chapter.

The investigation on mass transfer both in the absence and in the presence of electric field are described in Chapter Seven. The results presented are based on a two stage mass transfer mechanism: the drop formation stage and the drop free fall stage are considered, with the effect during drop coalescence stage being ignored. The EHD enhanced mass transfer mechanism has also been discussed.

Chapter Eight contains the conclusions of this work while Chapter Nine gives the recommendations for further work. Appendix A includes the derived equations of the reverse coordinate transformation which have been used in Chapter Four for the numerical model. Appendix B includes the derivations for two approximate analytical solutions of Laplace's equation with which the results of numerical electric field modelling have been compared in Chapter Four. The FORTRAN program for the numerical electric field modelling described in Chapter Four is attached in Appendix C and some of the numerical results are given in Appendix D. Appendix E summarizes the contributions of this work to knowledge where the papers have been published or have been accepted for publication based on this work are listed.

# Chapter 2

# Electrohydrodynamics (EHD): Liquid-Liquid Two Phase System

## 2.1 Introduction

Electromagnetic field and fluid interactions abound in nature and in technology. Three distinct disciplines have emerged from among the numerous studies and applications:

- *Magnetohydrodynamics* — the engineering science of the interaction between magnetic fields and fluid conductors of electricity (*e.g.* Hughes and Young, 1966; Eringen and Maugin, 1990) and the best established of the three;
- *Electrohydrodynamics* — the engineering science of the interaction between electric fields and fluids (*e.g.* Chu, 1959; Melcher and Taylor, 1969; Melcher, 1981; Chang, 1986; Eringen and Maugin, 1990) and the subject of concern in this chapter; and

- *Ferrohydrodynamics* — the engineering science of the interaction between magnetic fields and man-made colloidal magnetic liquids called ferrofluids (*e.g.* Rosensweig, 1979; Eringen and Maugin, 1990).

As an interdisciplinary subject of study, electrohydrodynamics abbreviated EHD, can be regarded as a branch of *fluid mechanics* concerned with electrical force effects. It can also be considered as a branch of *electrodynamics* which is involved with the influence of moving media on electric fields. Actually, it is both of these areas combined, since many of the most interesting problems in EHD involve both an effect of the fluid motion on the fields and an influence of the fields on the fluid motion (Melcher and Taylor, 1969).

The effect of EHD forces on the fluid flow can be categorized as (Chang, 1987)

- micro and bulk convections;
- multi-phase interfacial instabilities;
- enhancement of entrainment generations;
- electrostatic adhesive forces in between solid particles.

Although this area of research includes single phase fluids as well as liquid-liquid, gas-liquid and solid-in-fluid dispersions, the discussions in this chapter will be mainly restricted to liquid-liquid systems. First one must understand the effect of an electric field and a charge density upon a single stagnant liquid. Once these fundamental relationships are in place one can then proceed to determine the effect of electric field and charge at a discontinuity of electrical properties — an interface between two immiscible liquids. Generally speaking, these interfacial effects manifest themselves as a resultant force or shear stress that can include a static deformation of the interface and even steady or transient liquid motion. It is the understanding of the nature of the electric-field-induced forces that arise at liquid-liquid interfaces which forms the

basis for exploration of potential application of electric fields in liquid-liquid mass transfer operations.

## 2.2 Fundamental Laws of Electrostatics and Dielectrics

Electrohydrodynamics (EHD) is concerned with interactions of electric fields and free and/or bound (polarization) charges in fluids. The electrical conductivity of fluids may range from very low values of dielectric fluids (*e.g.* $10^{-9}$ S/m of mineral oils) to high values of electric conducting fluids (*e.g.* $10^{0}$ S/m of sea water). However, the distinguishing feature is that most of the electromagnetic effects on the system may be described by a quasi-static electric field model: the dynamics of electric current is normally slow and the influence of the magnetic induction therefore is negligible. The assumptions of isotropy of the fluid at constant temperature and linearity of the constitutive relations have been made for the following sections.

### 2.2.1 Maxwell's equations for a quasi-static electric field system

Maxwell (1892) showed how these basic laws can be transformed into field equations and postulated the existence of a displacement current term in Ampere's law. The set of four equations, which are known as Maxwell's equations, is the starting point of all theoretical analyses that involve electromagnetic fields.

In the case of quasi-static electric field, Maxwell's equations reduce to Gauss' law which relates the free charge density, $\rho_e$ (C/m$^3$) to the electric displacement, $\mathbf{D}$ (C/m$^2$)

$$\text{div}\,\mathbf{D} = \nabla \cdot \mathbf{D} = \rho_e \tag{2.1}$$

and to Faraday's law

$$\text{curl}\,\mathbf{E} = \nabla \times \mathbf{E} = \mathbf{0} \tag{2.2}$$

where $\mathbf{E}$ (V/m) is the electric field intensity. According to Equation (2.2), the irrotational nature of the electric field intensity indicates that there is a scalar function $\phi$ (electric potential) related with the electric field intensity, *i.e.*

$$\mathbf{E} = -\nabla\phi \tag{2.3}$$

The charge conservation equation is written as

$$\frac{\partial \rho_e}{\partial t} + \nabla \cdot \mathbf{J} = 0 \tag{2.4}$$

where $\mathbf{J}$ (A/m$^2$) is the electric current density.

### 2.2.2 Constitutive relations

#### Electric displacement

The electric field in a polarizable dielectric liquid involves contributions from the free charges and from the induced polarizations:

$$\mathbf{D} = \varepsilon_0\mathbf{E} + \mathbf{p} \tag{2.5}$$

where the polarization $\mathbf{p}$ is the induced dipole moment per unit volume and $\varepsilon_0$ is the dielectric constant or permittivity of free space. Hence, the electric displacement takes into account the "background electric field" as well as electric field contributions from induced polarization of the dielectric fluid media. The expression for isotropic and linear dielectrics indicates

$$\mathbf{p} = (\varepsilon - \varepsilon_0)\mathbf{E} = \varepsilon_0(\varepsilon_s - 1)\mathbf{E} \tag{2.6}$$

where $\varepsilon_s$ is the specific dielectric constant or relative permittivity. Therefore the constitutive relationship for electric displacement, $\mathbf{D}$, is written in terms of the electric

field:

$$\mathbf{D} = \epsilon \mathbf{E} \tag{2.7}$$

where the dielectric constant $\epsilon$ (F/m) depends on the fluid density and the temperature but it does not depend on the electric field. The dielectric constant can be thought of as a measure of the polarizability of the material.

### Electric current

The mechanisms of electrical conduction in liquids and gases are quite different from those in solids in many instances. Generally, the conduction in dielectric liquids occurs by means of positive or negative ions. The ions in a dielectric liquid may arise from dissociation of the host medium or from impurities. The ions may also be injected into the dielectric liquid from one or both electrodes at high applied electric fields (Kitahara, 1984). If an electric field is applied to the dielectric liquid, the positive ions (cations) and negative ions (anions) will move towards different electrode terminals. Since ions are much larger than electrons, they have much more difficulty getting through the liquid than do electrons in most good solid conductors.

For the case of liquid in motion, the total current density measured from a stationary frame of reference is given by (Lam, 1964)

$$\mathbf{J} = \rho_{ei}\mathbf{U} \pm \rho_{ei}\mu_e\mathbf{E} - \mathcal{D}_e\nabla\rho_{ei} \tag{2.8}$$

where $\rho_{ei}$ is defined as the local charge density which may include both positive and negative ions. The first term in Equation (2.8) is due to convection of ions by the velocity field. This term influences the charge density via the charge conservation law, which in turn modifies the velocity field as well. The second term in Equation (2.8) gives the contribution of the ions moving under the influence of the electric field with a drift velocity, $\mu_e\mathbf{E}$ (m/s) relative to the fluid. The term $\mu_e$ ($m^2$/Vs) is the ion mobility. The third term in Equation (2.8) accounts for charge diffusion with diffusion

constant $\mathcal{D}_e(\mathrm{m}^2/\mathrm{s})$ which can often be estimated from mobility by Einstein's relation:

$$\mathcal{D}_e \simeq \frac{\mu_e kT}{e} \tag{2.9}$$

where $k$ and $T$ are Boltzmann constant ($= 1.381 \times 10^{-23}$ J/K) and absolute temperature respectively, $e$ is the absolute value of the electronic charge ($= 1.602 \times 10^{-19}$ C).

## 2.3 Basic Equations of Electrohydrodynamics

### 2.3.1 Electric field and potential in dielectric liquids

The study of electric field effects on dielectric liquids requires a knowledge of the distribution of electric field as well as electric potential. In principle the electric potential distribution within the system under applied electric fields may be determined using Poisson's equation, which can directly be derived from Equations (2.1), (2.3) and (2.7), provided that the dielectric constant is held constant:

$$\nabla^2\phi = -\frac{\rho_e}{\varepsilon} \tag{2.10}$$

There is no net bulk free charge density in dielectric fluids unless a given element of dielectric liquid can be traced via its stream line to a source of charge (Melcher and Taylor, 1969). If this is the case then the Poisson's equation is reduced to Laplace's equation:

$$\nabla^2\phi = 0 \tag{2.11}$$

### 2.3.2 Electrohydrodynamic (EHD) forces

The EHD forces acting on dielectric fluids stressed in the electric field can be unified and expressed (Landau and Lifshitz, 1960) as:

$$\mathbf{f}_e = \rho_{ei}\mathbf{E} - \frac{1}{2}E^2\nabla\varepsilon + \nabla[\frac{1}{2}\rho E^2(\frac{\partial\varepsilon}{\partial\rho})_T] \tag{2.12}$$

where $\rho_{ei}$ is the local space charge density as defined in Equation (2.8), $\mathbf{E}$ is the electric field, $\varepsilon$ is the dielectric constant, $\rho$ is the density and $T$ is the temperature. The first term in Equation (2.12) is the force due to the local space charges, the second term represents the force due to the dielectric property change and the third term gives the force due to the inhomogeneity of electric field strength and is called the "electro-strictive" force.

Equation (2.12) indicates that the electrically induced forces will exist wherever there are spatial variations in either $\varepsilon$ or $E^2$, or both. Therefore the stress created at boundaries and in regions of non-uniform fields can play an important role in determining the stress distribution within a dielectric liquid.

Alternatively, $\mathbf{f}_e$ can also be expressed in terms of divergence of the stress tensor as:

$$\mathbf{f}_e = \nabla\cdot\mathbf{T}_e = \nabla\cdot[-(p_p + p_s)\mathbf{I} + \mathbf{DE}] \tag{2.13}$$

where $p_p$ is the fluid polarization pressure,

$$p_p = \frac{1}{2}\varepsilon E^2 \tag{2.14}$$

$p_s$ is the electrostrictive pressure,

$$p_s = -\frac{1}{2}\rho(\frac{\partial\varepsilon}{\partial\rho})_T E^2 \tag{2.15}$$

and $\mathbf{I}$ is the unit tensor.

## 2.4 Electrohydrodynamic Forces in Liquid-Liquid Two-Phase System

### 2.4.1 Electric field around an immersed dielectric droplet

Consider a spherical droplet of radius $a$ and dielectric constant $\varepsilon_d$ moving in a continuous phase of dielectric liquid with dielectric constant $\varepsilon_c$ to which a non-uniform electric field, $\mathbf{E}_c$, is applied. The translational motion of the droplet caused by the non-uniform field-induced polarization effects is defined as *dielectrophoresis*; while the motion caused by the response to free charge on the drop is defined as *electrophoresis*. A quantitative theory of dielectrophoresis as well as electrophoresis requires a knowledge of the electric field around a dielectric body immersed in another dielectric liquid. Also dielectrophoresis occurs only in a spatially non-uniform electric fields.

Since the droplet size is relatively small, then making the approximation that the field, although non-uniform enough to produce appreciably different force on the positive and negative polarization charges, does not vary strongly enough to sensibly alter the degree of polarization and hence the size of the dipole throughout the volume of the droplet sphere. Therefore the electric field can be assumed uniform over the dimensions of the droplet. In addition the interference to the external applied electric field by charged droplet due to the extra field in the droplet is considered negligible; then Laplace's equation (Equation (2.11)) can be used to calculate the electric field as well as potential in a two-phase dielectric liquid-liquid system, and the solutions should satisfy the boundary conditions:

- The tangential component of the electric field must be continuous at the interface separating two dielectric liquids, *i.e.* $\mathbf{E}_{c,t} = \mathbf{E}_{d,t}$.
- The normal component of the electric flux-density, or displacement, must be continuous across an uncharged interface separating two dielectric liquids, *i.e.*

$$\varepsilon_c \mathbf{E}_{c,n} = \varepsilon_d \mathbf{E}_{d,n}.$$

The electric field, $\mathbf{E}_d$, in a dielectric spherical droplet immersed in a continuous phase of another immiscible dielectric liquid which is in an imposed non-uniform electric field, $\mathbf{E}_c$, has been found in the literature (Kao, 1961):

$$\mathbf{E}_d = \frac{3\varepsilon_c}{2\varepsilon_c + \varepsilon_d}\mathbf{E}_c \tag{2.16}$$

The electric field in the droplet obviously is different from the applied electric field at the location of the droplet, except for the case where $\varepsilon_c = \varepsilon_d$. It is noted also from Equation (2.16) that when $\varepsilon_d$ is very large, $\mathbf{E}_d$, the electric field in the droplet is very small, corresponding to the case where the droplet is electrically conductive.

### 2.4.2 EHD forces acting on spherical droplet immersed in dielectric liquid

The behaviour of a droplet in another dielectric liquid which is subject to an electric field is quite complex due to the electric stresses created at the interface. This section is intended to clarify and to define the EHD forces acting on a spherical droplet which is immersed in another dielectric liquid and is electrohydrodynamically stressed in a non-uniform electric field, $\mathbf{E}_c$. On the other hand, as has been described in Equation (2.16), there is a local electric field, $\mathbf{E}_d$, due to the difference in the properties between the droplet phase and continuous phase, especially the difference in dielectric constant. Therefore we may define an *effective dielectric constant*, $\varepsilon_{eff}$ as:

$$\varepsilon_{eff} = (\varepsilon_d - \varepsilon_c) \cdot \left(\frac{3\varepsilon_c}{\varepsilon_d + 2\varepsilon_c}\right) = \frac{3\varepsilon_c(\varepsilon_d - \varepsilon_c)}{\varepsilon_d + 2\varepsilon_c} \tag{2.17}$$

The EHD forces acting on a spherical drop may be obtained from Equation (2.13) with the introduction of effective dielectric constant, $\varepsilon_{eff}$:

$$\mathbf{f}_e = -\nabla p_e + \mathbf{f}_{e1} + \mathbf{f}_{e2} = -\nabla p_e + \rho_{ed}\mathbf{E}_d + (\mathbf{p} \cdot \nabla)\mathbf{E}_c \tag{2.18}$$

where $\rho_{ed}$ is the drop volume charge density, $p_e$ is defined as the total EHD pressure component acting on the droplet, $\mathbf{f}_{e1}$ is the electrophoretic force component acting on the droplet and $\mathbf{f}_{e2}$ is the dielectrophoretic force component acting on the droplet. $\mathbf{E}_c$ and $\mathbf{E}_d$ in Equation (2.18) are the external applied electric field and the local electric field generated in the droplet respectively.

### Total EHD pressure, $p_e$, acting on the droplet

The total EHD pressure, $p_e$, acting on the droplet may be directly obtained from Equations (2.14) and (2.15) with the substitution of effective dielectric constant, $\varepsilon_{eff}$:

$$p_e = p_p + p_s = \frac{1}{2}\varepsilon_{eff}E_c^2 - \frac{1}{2}\rho_c(\frac{\partial\varepsilon_{eff}}{\partial\rho})_T E_c^2 \tag{2.19}$$

where the effective dielectric constant has been defined in Equation (2.17). Following Ogata *et al.* (1985), the electrostrictive pressure component in Equation (2.19) can be obtained by the Clausius-Mossotti equation, *i.e.*

$$\rho_c(\frac{\partial\varepsilon_{eff}}{\partial\rho})_T = \frac{1}{3}\varepsilon_d(\varepsilon_c/\varepsilon_d + 2)(\varepsilon_c/\varepsilon_d - 1) \tag{2.20}$$

Therefore the total EHD pressure term, $p_e$, acting on the droplet can be obtained:

$$p_e = \frac{3}{2}[\frac{\varepsilon_c(\varepsilon_d - \varepsilon_c)}{\varepsilon_d + 2\varepsilon_c}]E_c^2 + \frac{1}{6}[\varepsilon_d(\varepsilon_c/\varepsilon_d + 2)(\varepsilon_c/\varepsilon_d - 1)]E_c^2 \tag{2.21}$$

### Electrophoretic force, $\mathbf{f}_{e1}$, acting on the droplet

According to Equations (2.12) and (2.16), the force directly exerted on the droplet due to electrophoretic component in Equation (2.18), $\mathbf{f}_{e1}$, may be expressed as:

$$\mathbf{f}_{e1} = \rho_{ed}\mathbf{E}_d = (\frac{3\varepsilon_c}{2\varepsilon_c + \varepsilon_d})\rho_{ed}\mathbf{E}_c \tag{2.22}$$

**Dielectrophoretic force, $f_{e2}$, on the droplet**

The dielectrophoretic component in Equation (2.18), $f_{e2}$, acting on the droplet is derived following Pohl (1973) and Equation (2.16):

$$f_{e2} = \mathbf{p} \cdot \nabla \mathbf{E}_c = [(\varepsilon_d - \varepsilon_c)\mathbf{E}_d] \cdot \nabla \mathbf{E}_c = \frac{3}{2}[\frac{\varepsilon_c(\varepsilon_d - \varepsilon_c)}{\varepsilon_d + 2\varepsilon_c}]\nabla E_c^2 \tag{2.23}$$

It should be mentioned that the EHD force components on the droplet derived above are expressed as the force density ($N/m^3$) based on the volume of droplet. Therefore the total force is equal to the product of force density and droplet volume.

## 2.5 Maximal Charge Acquired during Electrohydrodynamic Droplet Formation

A droplet can be formed by a number of mechanisms including application of an electric field and by forcing liquid through an orifice electrode or hollow nozzle electrode. If droplet is electrically charged during its formation, the charge resides on the droplet and exerts an outward electric force which counteracts the surface tension force. For the droplets formed in the atmosphere with such a process, there are several equations correlating total charge on a droplet or specific charge (charge-to-mass ratio) of a droplet with its radius. The equation well known as the ***Rayleigh instability limit*** represents the maximum charge that can be held by a stable droplet of given radius (Rayleigh, 1882):

$$q = 8\pi(\varepsilon_0 \gamma a^3)^{1/2} \tag{2.24}$$

or expressed as the charge-to-mass ratio:

$$\frac{q}{m_d} = \frac{6}{\rho_d}(\frac{\varepsilon_0 \gamma}{a^3})^{1/2} \tag{2.25}$$

where $m_d$ is the mass of the droplet, $\rho_d$ is the drop-phase density, $\varepsilon_0$ is the dielectric constant of free space, $\gamma$ is the surface tension of the liquid and $a$ is the droplet

radius. Other correlations derived from the approach based on minimum energy state assumption (Vonnegut and Neubauer, 1952; Pfeifer and Hendricks, 1967; Ogata *et al.*, 1978) have the similar forms as Rayleigh instability model but with lower coefficient values compared to those in Equations (2.24) and (2.25). For example, the Vonnegut's model has only one half of the coefficient value but with exact the same form as Equation (2.24) or (2.25). The validity of these equations have also been confirmed by experimental investigations (Hendricks, 1962; Ogata *et al.*, 1976; Roth and Kelly, 1983).

On the other hand, since the situation governing the maximum charge on the droplet in liquid-liquid systems is more complex no general correlation equation has been proposed to estimate the maximal charge limit on the forming droplet in liquid-liquid two-phase systems and some times Rayleigh instability model was still referred to compare with experimental results (*e.g.* Stewart and Thornton, 1967; Thornton, 1968).

It is noted that Equations (2.24) and (2.25) apply to the maximum charge that a relatively conductive dielectric droplet can hold before it will split into smaller droplets in the air. In the case of one dielectric liquid being dispersed into a second dielectric liquid medium due to the effect of an applied electric field, Equations (2.24) and (2.25) as well as other correlations mentioned above should be modified before they can be used to predict the maximum charge limit for the dispersed droplets in a liquid-liquid system:

- dielectric constant or permittivity of free space in Equations (2.24) and (2.25) should be replaced by the effective dielectric constant, $\epsilon_{eff}$, defined in Equation (2.17);
- instead of using the surface tension of dispersed liquid, the interfacial tension between dispersed liquid phase and continuous liquid phase should be used.

The modified Rayleigh instability limit equation therefore can be expressed as follows:

$$q = 8\pi(\varepsilon_{eff}\sigma a^3)^{1/2} = 8\pi\{[\frac{3\varepsilon_c(\varepsilon_d - \varepsilon_c)}{2\varepsilon_c + \varepsilon_d}]\sigma a^3\}^{1/2} \tag{2.26}$$

or expressed as the form of charge-to-mass ratio:

$$\frac{q}{m_d} = \frac{6}{\rho_d}(\frac{\varepsilon_{eff}\sigma}{a^3})^{1/2} = \frac{6}{\rho_d}\{[\frac{3\varepsilon_c(\varepsilon_d - \varepsilon_c)}{2\varepsilon_c + \varepsilon_d}]\frac{\sigma}{a^3}\}^{1/2} \tag{2.27}$$

where $\varepsilon_{eff}$ is the effective dielectric constant of the two dielectric liquid system determined by Equation (2.17) and $\sigma$ is the interfacial tension between dispersed and continuous phases.

# Chapter 3

# Experimental Apparatus and Procedures

## 3.1 Experimental Apparatus

The experimental apparatus used in this work is shown schematically in Figure 3.1. It consists essentially a rectangular cell equipped with planar electrodes on both sides of the cell, one hollow electrode on the top end of the cell and a flow system for droplet formation, a Faraday cup for droplet charge measurement as well as for collecting samples of dispersed phase, and a DC high voltage electric power supply.

### 3.1.1 Experimental cell

The experimental cell is made of transparent LUCITE plastic and is 38 cm long and 10 cm × 10 cm in width. The planar electrode plates are mounted along the two opposite sides and in parallel onto the cell as schematically shown in Figure 3.1.

Droplets of dispersed phase are formed at a hollow nozzle (as hollow electrode

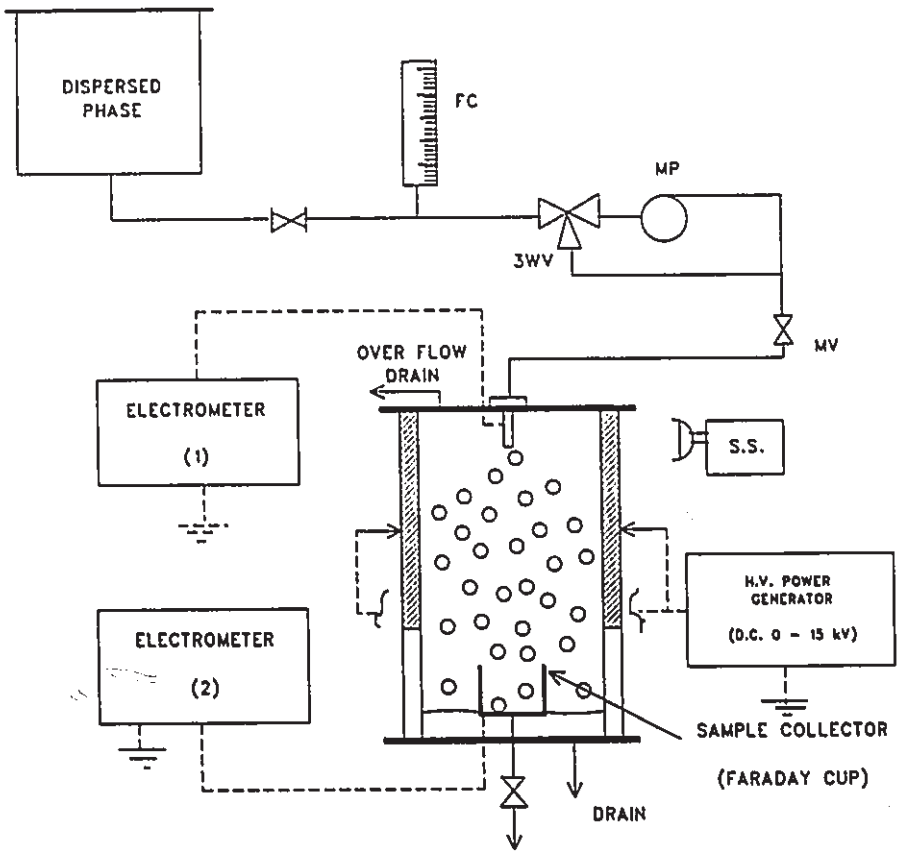


S.S.–stroboscope; MV–metering valve;
3WV–3 way valve; FC–flow rate calibration;
MP–micro pump

Figure 3.1: Schematic diagram of apparatus

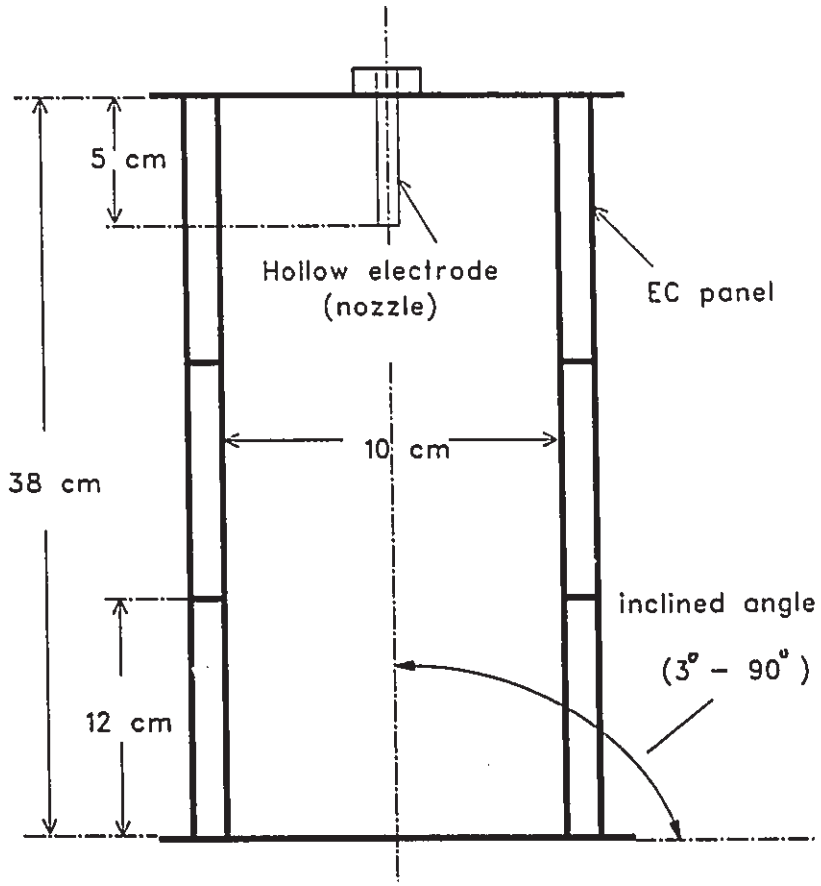


Figure 3.2: Configuration of the experimental cell

when electric field is applied) mounted at the top end of the cell and inserted about 5 cm from the end plate as described in Figure 3.2. The diameter of the two hollow nozzles used in this work are described in Table 3.1.

The cell could be operated with its axis at an inclined angle between 3° and 90° to the horizontal. As the droplets of dispersed phase are fed via the (nozzle) hollow electrode, displaced oil is allowed to exit through an open overflow as shown in Figure 3.1. Periodically a drain valve is opened to remove accumulated dispersed phase from the bottom of the cell.

### 3.1.2 Planar electrode plate

The detailed structure of the EC electrode panel (Masuda *et al.*, 1972) is schematically shown in Figure 3.3. The multi-electrode-wires are covered with a layer of ceramic type dielectric material. This layer serves to inhibit electric breakdown between the electrodes as well as to inhibit the direct contact between the electrodes and two liquid phases. There are 6 such planar electrodes equipped on the experimental cell with 3 on each side as shown in Figure 3.2, although only 4 of those are connected to the electric circuit in most of the time during experiment of this work to avoid leaking of current down streams.

### 3.1.3 Faraday cup

As seen in Figure 3.1, the Faraday cup is located in the centre bottom of the cell. It is electrically connected to a Multi-Range Electrometer (Keithley Model 610BR) through a shielded cable for charge measurement. It is also used as a drop phase sample collector during mass transfer experiment. The detailed structure of the Faraday cup is schematically shown in Figure 3.4. The cylindrical cup is made of aluminum with inner cup of 5 cm diameter and outer cylinder of 7 cm diameter insulated with

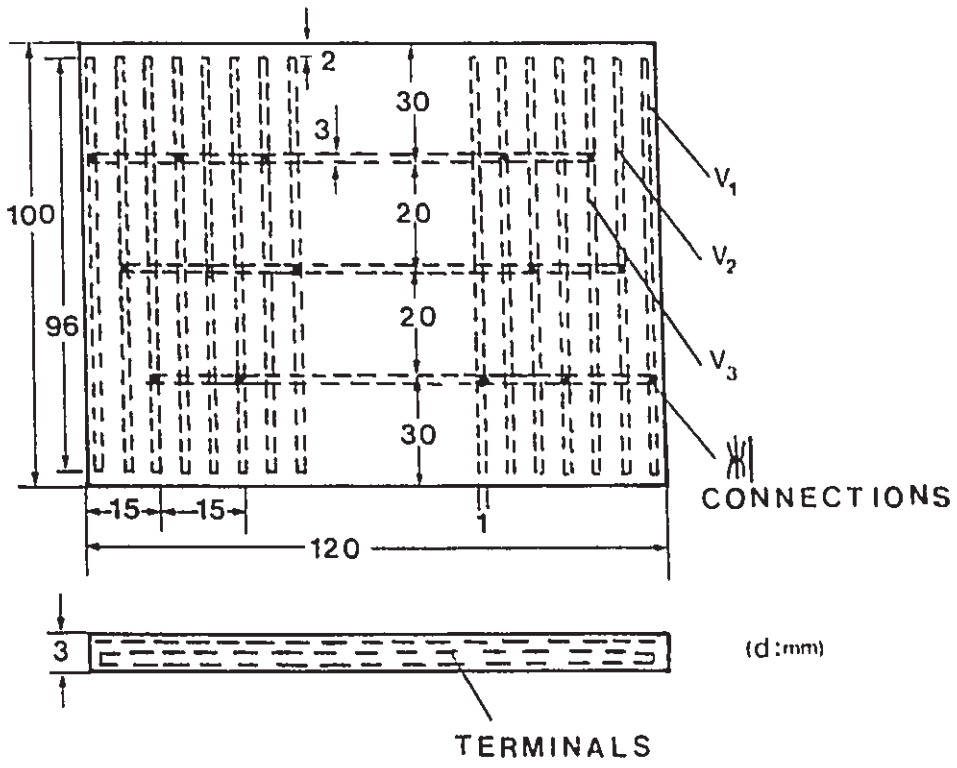


Figure 3.3: Configuration of planar electrode plate

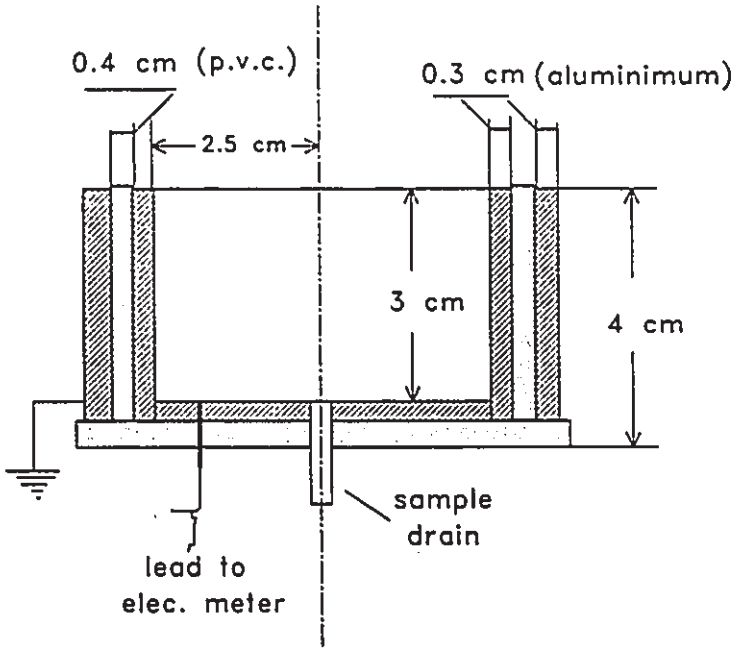


Figure 3.4: Configuration of Faraday cup

an annular layer of PVC in between. There is an outlet access of 0.5 cm in diameter at the bottom of the Faraday cup, where the collected droplet phase sample is released to the sample bottle through a connecting tube.

### 3.1.4 DC electric power supply

High voltage electric field is generated using a DC electric power supply (Universal Voltronics Corp.) with an output range of 0–15 kV (voltage) and 0–5 mA (current). The geometry of the experimental setup and the connections with the electric power source ensure that conduction current is very low in the circuit even at very high applied voltages. Detailed Current-Voltage characteristics of the system will be discussed in Chapter 6.

## 3.2 Experimental Procedures

The experiment was conducted at the ambient temperature ($22 \pm 2\ ^{\circ}C$). The dispersed phase flow rate was carefully calibrated before each run of the experiment; the continuous phase was quiescent except for slight overflow due to the replacement of dispersed droplets during the experiment. The dispersed phase was fed from an overhead tank through a metering valve and a micropump, with a measuring column in the circuit to allow calibration and checking of the flow rate. The continuous phase was a pure paraffin hydrocarbon mineral oil which has very low vapor pressure and no additives. The high viscosity of the oil ensured that the drops moved in the creeping flow regime, which allowed for simple calculation of the relationship between drag force and velocity.

The run duration for every experiment at steady state was varied from 30 min. to 3 hrs. with different flow rates of dispersed phase in order to collect enough samples

to analyze the concentration of benzoic acid. Two repeated runs were conducted at a different time schedule for every experimental condition, therefore the results reported in the following chapters are the data averaged from two repeated runs. Generally the relative percentage difference for mass transfer efficiency between the two repeated runs was within 10%.

Two different electrode connection modes were used in this work mainly to compare the differences in time-averaged current-voltage (I-V) characteristics from which the efficiency of the energy input can be determined:

- hollow electrode is grounded and planar electrode plates are connected to the high voltage power supply;
- hollow electrode is connected to the high voltage power supply and planar electrode plates are grounded.

### 3.2.1 Droplet formation and dispersion experiment

Distilled water was chosen as the droplet phase. The continuous phase was a paraffin hydrocarbon mineral oil (Fisher Brand 01–184–150B). Properties are given in section 3.3 below. A series of experiments was conducted to investigate the effects of dispersed phase flow rate, inclined angle and (nozzle) hollow electrode size upon droplet formation and motion in the absence and in the presence of electric field. The ranges of experimental conditions for droplet formation and dispersion experiment are summarized in Table 3.1.

### 3.2.2 Mass transfer experiment

Distilled water was chosen as the droplet phase. Benzoic acid was dissolved in the distilled water at a concentration of 1.7–2.3 g/L (0.014 mol/L–0.019 mol/L) as the transferring solute. The continuous phase was the paraffin hydrocarbon mineral oil (Fisher Brand 01–184–150B). Analysis of benzoic acid concentration in the dispersed phase was carried out by titration with 0.01 mol/L sodium hydroxide using phenolphthalein as indicator.

A fresh batch of the continuous phase (mineral oil) was fed into the cell to replace the old one after every several experimental runs, so that the concentration of benzoic acid in the oil remained negligible. The solute transfer across the bulk interface inside the sample collector was ignored. the range of the experimental conditions for mass transfer experiment are summarized in Table 3.2.

### 3.2.3 Measurement of electrical parameters

The electrical parameters were either controlled or monitored using the oscilloscope (Tektronix Inc., Model 468), multi-range Electrometer (Keithley Model 610BR) and DC power supply (Universal Voltronics Corp.) when the experiments were carried out with the high voltage being applied. The parameters measured were as follows:

1. applied DC voltage (control variable):
   - read directly from the volt-meter equipped on the power supply;
   - using oscilloscope via a divider.
2. current at different locations in the circuit:
   - current at hollow electrode (a) — measured directly with multi-range electrometer connected in series between hollow electrode and ground, when

the power supply was connected to the planar electrode.

- current at hollow electrode (b) — read directly from the ammeter equipped on the power supply, when the power supply was connected to the hollow electrode.
- current at planar electrode — measured directly with multi-range electrometer connected in series between planar electrode and ground, when the power supply was connected to the hollow electrode.
- current carried by droplets collected at Faraday cup — determined indirectly from the slope of time dependence of the time-averaged charge measured from the collected droplets with multi-range electrometer connected in series between Faraday cup and ground. A chart recorder is also connected to the electrometer to obtain charge accumulation as shown in Figure 3.5.

3. determination of droplet electric charge (time averaged results):

- time averaged charge on a forming droplet detached from hollow electrode — measured indirectly from the excess hollow electrode current and the frequency of droplet detachment, *i.e.*

$$q = \frac{I_a - I_b}{f} \tag{3.1}$$

where $I_a$ is the current measured at the condition of drop phase flow with the applied voltage and $I_b$ is the background current measured at the condition without drop phase flow but with the same applied voltage.

- time averaged charge on a droplet collected in the Faraday cup — determined from the accumulated values of charge with multi-range electrometer and the total sample volume collected.

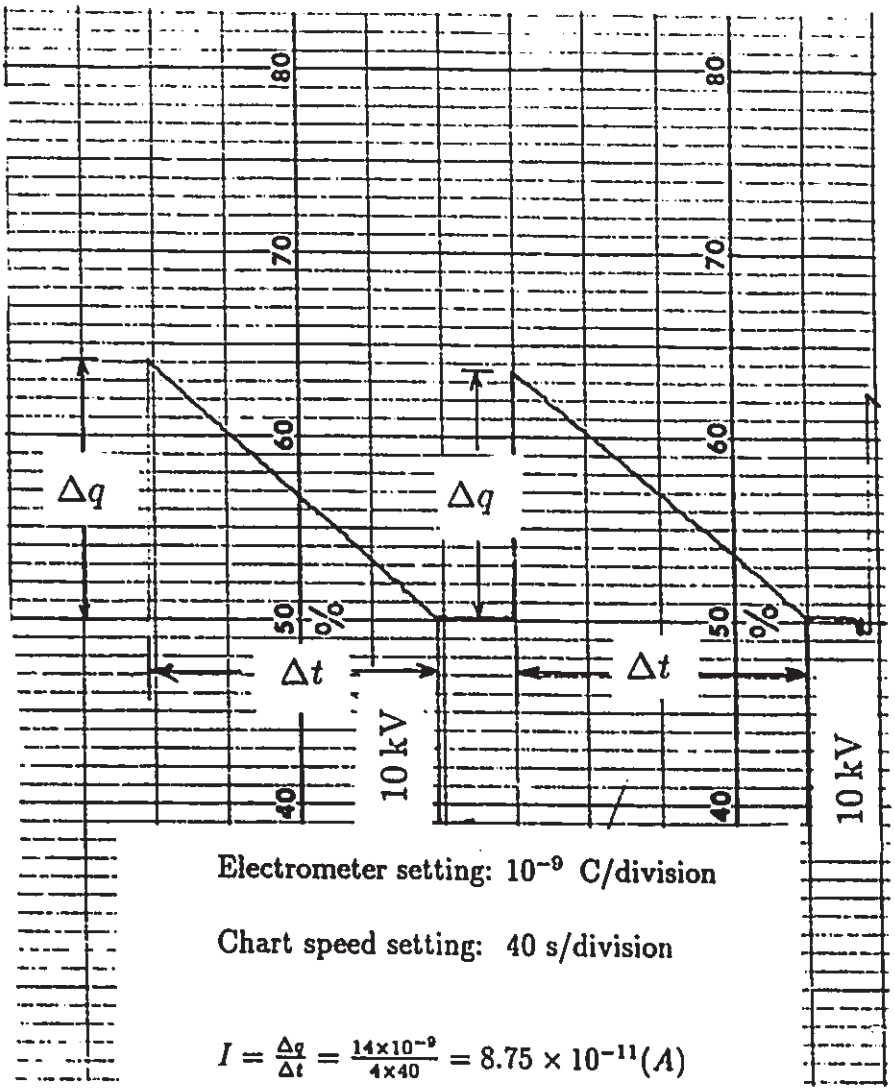


Figure 3.5: Typical charge accumulation measured by the Faraday cup

### 3.2.4 Measurement of droplet size and velocities

During experimental runs, a Sony Handy-Cam 9 video camera was used to record droplet formation and dispersion and still photographs were taken with an Olympus model Om-2 35 mm camera. Also the droplet detachment frequency, $f$, was measured by a digital stroboscope. During every experimental run the droplet detachment frequency was measured three times respectively at early, middle and later period of the experiment. The relative variation between these $f$ values was typically around 3–5%. Then the frequency was determined as the arithmetic mean of the three.

#### Measurement of droplet diameters

Since the droplets detached from the hollow electrode were uniform in size under the present experimental conditions, an equivalent spherical droplet diameter was calculated from the volumetric flow rate of dispersed phase, $Q$, through the hollow electrode and the droplet detachment frequency, $f$, which was measured by the digital stroboscope, *i.e.*

$$d = (6V_d/\pi)^{1/3} = (6Q/\pi f)^{1/3} \tag{3.2}$$

At the early experimental stage, the diameters of the droplets were also found from still photographs by slide projection and measurement with a ruler.

#### Measurement of droplet Velocities

1. Terminal velocity was measured by two methods:
   - using a stop watch, only when the experiment was run in the absence of electric field.
   - from recorded video images with frame by frame analysis.

2. Initial velocity ($U_{tip}$): $U_{tip}$ was also determined from recorded video images with frame by frame analysis. Then the drop velocity near the hollow electrode tip could be calculated from the measured separation distance $W$ between two successive drops.

$$U_{tip} = Wf = \frac{6QW}{\pi d^3} \tag{3.3}$$

The droplet initial velocities were generally measured over a distance of 1-3 cm from the hollow electrode tip. The assumption of one dimensionally radial dispersion with the origin at the hollow electrode tip was made.

### 3.2.5 Measurement of benzoic acid concentration

Analysis of benzoic acid concentration in the dispersed phase was carried out by titration with 0.01 mol/L sodium hydroxide using phenolphthalein as indicator.

### 3.2.6 Calibration of dispersed phase flow rate

The dispersed phase flow rate was calibrated by a volumetric glass tube connected in the flow circuit to ensure the steady constant flow rate within the duration of experimental run.

## 3.3 Determination of System Properties

The physical and chemical properties for the substances involved in this investigation were either experimentally determined or numerically evaluated using appropriate equations. Some of them are briefly described below. The summary of the system properties is shown in Table 3.3.

### Conductivity

The electrical conductivity of both dispersed phase and continuous phase were measured using a digital electrical conductivity meter (Model: CDM-83).

- The dispersed phase includes: (1) distilled water; (2) benzoic acid solution ($\sim 2$g/L).
- The continuous phase includes: (1) pure mineral oil; (2) recirculated mineral oil (dust contaminated and saturated with distilled water).

### Viscosity

The viscosities of the continuous phase pure as well as saturated with water were measured by two kinds of viscometer:

- **Rotary Viscometer** (Brookfield Eng. Labs. Inc. Model: LV), measuring additional torque required for the spindle, once immersed in a test liquid, to regain constant speed;
- **Glass Capillary Viscometer** (Cannon Instrument Co. model: Cannon-Fenske Routine), measuring efflux time for the test liquid through the capillary tube.

The viscosities obtained using these two methods agreed with accuracy within 5%.

### Molecular diffusivity

The quoted values of molecular diffusivity of benzoic acid were estimated from the Wilke and Chang (1955) equation, with the molecular weight of the oil being taken as 420 kg/kmol.

### Interfacial tension

Interfacial tension of the two liquid phases was measured using the drainage method (Baird and Nirdosh, 1981) and was also determined by the drop weight method during experimental runs when the flow rate of dispersed phase was controlled at very low values. The interfacial tension values obtained from these two approaches are quite close.

### Equilibrium distribution coefficient of benzoic acid

The equilibrium distribution of benzoic acid between the mineral oil and distilled water was measured at room temperature ($22 \pm 2\ ^{\circ}C$) by the usual method (Ritcey and Ashbrook, 1979) prior to the mass transfer experiments. The results, as shown in Figure 3.6, are in terms of the equilibrium concentrations in both phases expressed as grams per litre.

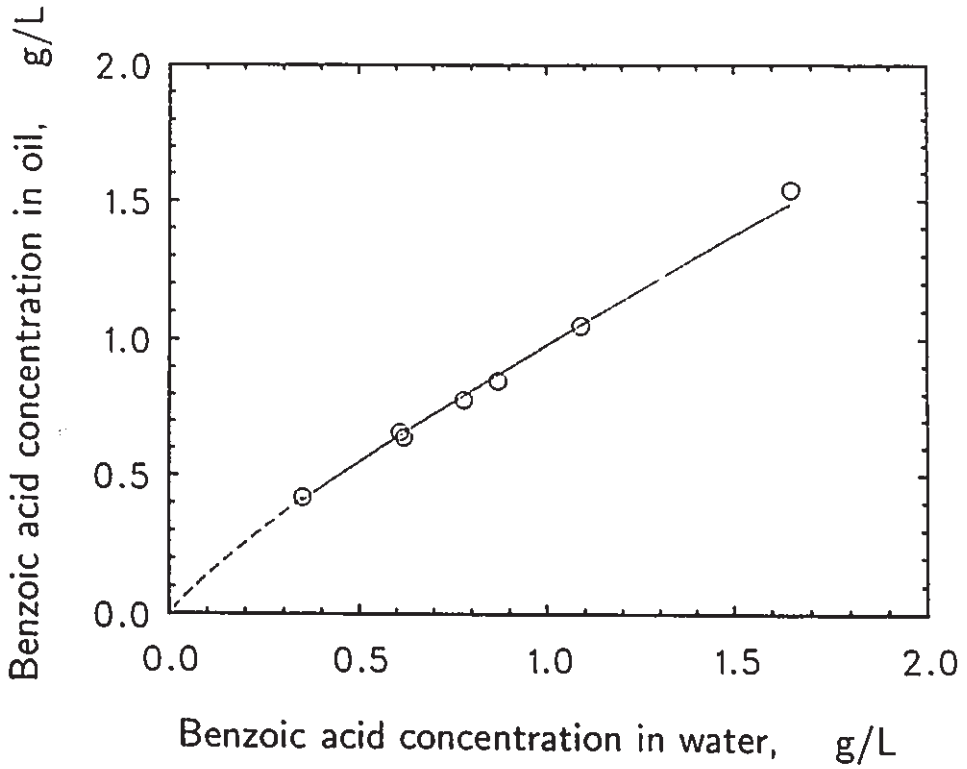


Figure 3.6: Equilibrium distribution characteristics of benzoic acid between oil and water (at room temperature $22 \pm 2°C$)

Table 3.1: Variables for droplet formation and dispersion experiment

| | |
|---|---|
| **Flow rate of dispersed phase** [$\mu$L/s] | 0.08 ~ 27 |
| **Inclination angle** [°] | 3, 30, 60, 90 |
| **Hollow electrode diameter** [mm] | (1) 0.29 (i.d.); 0.56 (o.d.)<br>(2) 0.39 (i.d.); 0.71 (o.d.) |
| **Applied DC voltage** [kV] | 0 - 15 |

Table 3.2: Variables for mass transfer experiment

| | |
|---|---|
| **Flow rate of dispersed phase** [$\mu$L/s] | 1.16 ~ 34.4 |
| **Inclination angle** [°] | 90 (vertically oriented) |
| **Hollow electrode diameter** [mm] | 0.39 (i.d.); 0.71 (o.d.) |
| **Applied DC voltage** [kV] | 0 - 15 |
| **Initial concentrations of Benzoic Acid** [g/L] | 1.7 - 2.3 |

Table 3.3: Summary of system properties

| **Properties at ambient temperatures** ($22 \pm 2$ °C) | **Dispersed Phase** (distilled water) | **Continuous phase** (mineral oil) |
|---|---|---|
| **Electrical conductivity** [$\mu$S/m] | 15.5 (distilled water) | 0.15 (pure mineral oil) |
| | 463 (benzoic acid solution) | 1.82 (saturated with drop phase) |
| **Specific dielectric constant**[a] [–] | 80 | 2.2 |
| **Viscosity** [mPa · s] | 1.0 | 115 |
| **Density** [kg/m$^3$] | 998 | 874 |
| **Molecular diffusivity of benzoic acid**[b] [cm$^2$/s] | $0.80 \times 10^{-5}$ | $0.215 \times 10^{-6}$ |
| **Schmidt number,** ($\nu/\mathcal{D}$) [–] | $1.25 \times 10^{2}$ | $5.88 \times 10^{6}$ |
| **Equilibrium distribution coefficient of benzoic acid** [–] | $\sim 1.0$ (see Figure 3.5) | |
| **Interfacial tension** [mN/m] | 28.1 (between distilled water and oil) | |
| | 28.6 (between benzoic acid solution and oil) | |

*a*: literature data (Crowley, 1986).
*b*: estimated using Wilke and Chang Equation (1955).

# Chapter 4

# Numerical Modelling of the Electric Field and EHD Forces

## 4.1 Introduction

The study of EHD effects on the droplet formation, dispersion and mass transfer requires a knowledge of the distribution of non-uniform electric field at different locations of the experimental cell as well as the components of the EHD force acting on the droplet. The calculation of electric field, or equivalently of electric potential, is the subject of classical field theory. As discussed in Chapter 2, the electric potential is governed by Laplace's equation of Equation (2.11) with the appropriate assumptions.

In general due to the complicated boundary conditions involved, the potential field must be calculated by means of some approximation methods, of which the numerical calculation method has emerged as a leading computational tool. A control volume method using the fixed grid has been formed the basis of the numerical technique used to solve Laplace's equation. This methodology has gained widespread acceptance, and the details of its implementation are well documented in

such publications as Patankar (1980), Anderson *et al.* (1984) and Minkowycz *et al.* (1988).

From experimental observations, the electric field near the hollow electrode was much stronger than any other region of the experimental cell. Since the length of the rectangular cell is almost four times longer than its width, and planar electrodes are in parallel on both side of the cell, the cylindrical axisymmetric form of a two dimensional Laplace's equation has been used for numerical modelling by assuming the width of the cell being the diameter of the cylinder. In addition the effect of presence of charged droplets on the electric field is also ignored in the electric field modelling.

Section 4.2 presents the model equations in axisymmetric coordinates. The model equations include the governing Laplace's equation with the appropriate boundary conditions which are determined from the approximations on this work. Other quantities can be predicted once the Laplace's equation is solved. The implementation of the numerical modelling is described in Section 4.3. Since the solution will be symmetric about the axial line it is sufficient to perform the computation for one half of the domain lying on one side of the symmetric line. The results obtained from numerical modelling are summarized in section 4.4 with some discussions.

## 4.2 Model Equations

### 4.2.1 Governing equation and boundary conditions

Laplace's equation with axial symmetry in cylindrical coordinates can be written as

$$\nabla^2\phi = \frac{1}{r}\frac{\partial}{\partial r}(r\frac{\partial \phi}{\partial r}) + \frac{\partial^2 \phi}{\partial z^2} = 0 \qquad (4.1)$$

with the following two sets of boundary conditions based on the approximations in this work:

- hollow electrode is grounded and planar electrode plates are connected to the high voltage power supply as shown schematically in Figure 4.1.

$$\phi = 0, \quad \text{at} \quad z = 0 \quad \text{and} \quad r_2 < r \leq r_1 \tag{4.2}$$

$$\phi = 0, \quad \text{at} \quad z = L_1 \quad \text{and} \quad 0 \leq r \leq r_1 \tag{4.3}$$

$$\frac{\partial \phi}{\partial r} = 0, \quad \text{at} \quad r = 0 \quad \text{and} \quad L_2 \leq z \leq L_1 \tag{4.4}$$

$$\phi = \phi_0, \quad \text{at} \quad r = r_1 \quad \text{and} \quad 0 \leq z \leq L_3 \tag{4.5}$$

$$\phi = 0, \quad \text{at} \quad 0 \leq r \leq r_2 \quad \text{and} \quad 0 \leq z \leq L_2 \tag{4.6}$$

- hollow electrode is connected to the high voltage power supply and planar electrode plates are grounded as shown schematically in Figure 4.2.

$$\phi = 0, \quad \text{at} \quad z = 0 \quad \text{and} \quad r_2 < r \leq r_1 \tag{4.7}$$

$$\phi = 0, \quad \text{at} \quad z = L_1 \quad \text{and} \quad 0 \leq r \leq r_1 \tag{4.8}$$

$$\frac{\partial \phi}{\partial r} = 0, \quad \text{at} \quad r = 0 \quad \text{and} \quad L_2 \leq z \leq L_1 \tag{4.9}$$

$$\phi = 0, \quad \text{at} \quad r = r_1 \quad \text{and} \quad 0 \leq z \leq L_1 \tag{4.10}$$

$$\phi = \phi_0, \quad \text{at} \quad 0 \leq r \leq r_2 \quad \text{and} \quad 0 \leq z \leq L_2 \tag{4.11}$$

### 4.2.2 Equations for EHD force components

The EHD forces acting on spherical drop which is immersed in another dielectric liquid in an electric field have already been derived in Chapter 2, Equation (2.18):

$$\mathbf{f}_e = -\nabla p_e + \mathbf{f}_{e1} + \mathbf{f}_{e2} = -\nabla p_e + \rho_{ed}\mathbf{E}_d + (\mathbf{p} \cdot \nabla)\mathbf{E}_c \tag{4.12}$$

It includes three terms which have also been derived in Chapter 2, Equations (2.21)-(2.23):

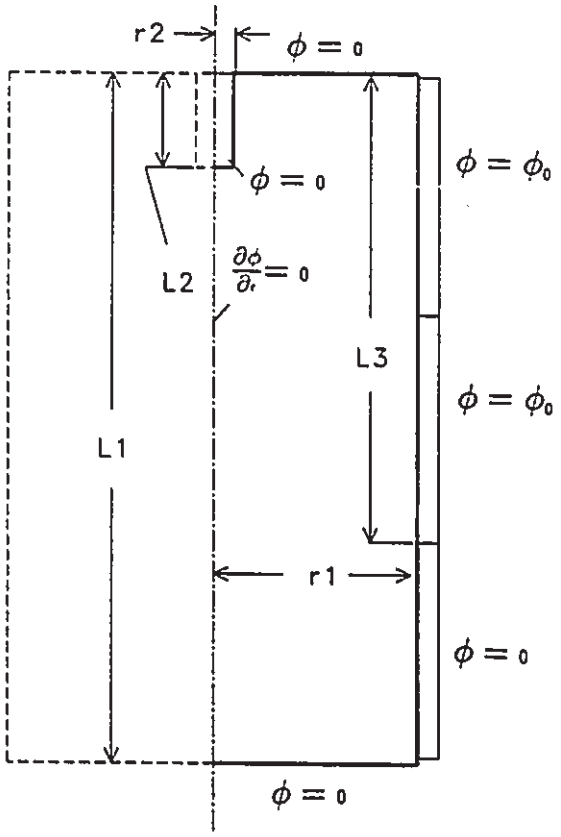


Figure 4.1: Configuration of the electrode connections – (1)

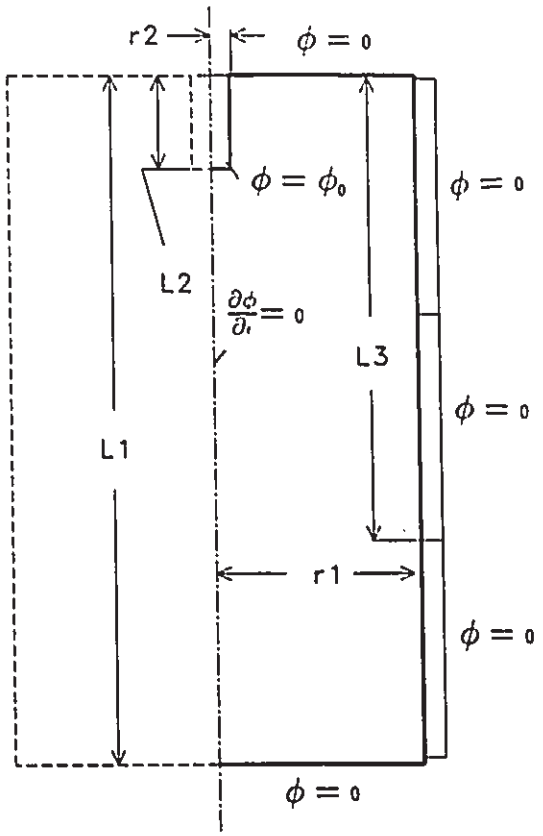


Figure 4.2: Configuration of the electrode connections - (2)

- the total EHD pressure term, $p_e$, acting on the droplet:

$$p_e = \frac{3}{2}[\frac{\varepsilon_c(\varepsilon_d - \varepsilon_c)}{\varepsilon_d + 2\varepsilon_c}]E_c^2 + \frac{1}{6}[\varepsilon_d(\varepsilon_c/\varepsilon_d + 2)(\varepsilon_c/\varepsilon_d - 1)]E_c^2 \tag{4.13}$$

- the electrophoretic component, $\mathbf{f}_{e1}$, acting on the droplet:

$$\mathbf{f}_{e1} = \rho_{ed}\mathbf{E}_d = (\frac{3\varepsilon_c}{2\varepsilon_c + \varepsilon_d})\rho_{ed}\mathbf{E}_c \tag{4.14}$$

  where $\rho_{ed}$ is the volume charge density of the droplet.

- the dielectrophoretic component, $\mathbf{f}_{e2}$, acting on the droplet:

$$\mathbf{f}_{e2} = \mathbf{p}\cdot\nabla\mathbf{E}_c = [(\varepsilon_d - \varepsilon_c)\mathbf{E}_d]\cdot\nabla\mathbf{E}_c = \frac{3}{2}[\frac{\varepsilon_c(\varepsilon_d - \varepsilon_c)}{\varepsilon_d + 2\varepsilon_c}]\nabla E_c^2 \tag{4.15}$$

Therefore the applied electric field, $\mathbf{E}_c$, the magnitude of the electric field square, $E_c^2$ and the gradient of the electric field square, $\nabla E_c^2$ should be calculated in order to predict the EHD force components acting on the spherical droplet. The subscript of $_c$ will be omitted for the sake of simplicity in the following descriptions. The axial symmetric form of these variables may be expressed as:

**Electric field**

$$\mathbf{E} = -\nabla\phi = -(\frac{\partial\phi}{\partial r}\mathbf{r} + \frac{\partial\phi}{\partial z}\mathbf{z}) \tag{4.16}$$

**Magnitude of the electric field square**

$$E^2 = (\frac{\partial\phi}{\partial r})^2 + (\frac{\partial\phi}{\partial z})^2 \tag{4.17}$$

**Gradient of the electric field square**

$$\nabla E^2 = \frac{\partial E^2}{\partial r}\mathbf{r} + \frac{\partial E^2}{\partial z}\mathbf{z} \tag{4.18}$$

## 4.3 Numerical Modelling

### 4.3.1 Transformations

In order to obtain the desired accuracy or "resolution" in this numerical modelling, grid points should be closely spaced near the hollow electrode where the gradients of electric potential are especially large, while relatively coarser grids are good enough at the region far away from the hollow electrode where the gradients of the electric potential are very small. This suggests that irregular mesh increments in the physical domain are appropriate for maintaining the level of accuracy of the results with relatively less computational effort. On the other hand, the solution algorithm can be greatly simplified by a well-constructed grid, *i.e.* the equal spaced and orthogonal grid, throughout the computational domain. Therefore coordinate transformation should be used such that unequal spacing in the original coordinate system becomes equal spacing in the new system, and the Equations (4.1)-(4.11) are also expressed in terms of the new coordinates. The algebraic transformation method (Anderson *et al.*, 1984) has been adapted to this work as described in the following sections.

**Transformation for $z$**

The transformation for independent variable $z$ is given by the following equations in order to cluster more points near $z = L_2$:

$$\bar{z} = B + \frac{1}{\tau}\sinh^{-1}\{[(z/L_2) - 1]\sinh(\tau B)\} \tag{4.19}$$

where

$$B = \frac{1}{2\tau}\ln[\frac{1 + (e^{\tau} - 1)(\frac{L_2}{L_1})}{1 + (e^{-\tau} - 1)(\frac{L_2}{L_1})}], \qquad 0 < \tau < \infty \tag{4.20}$$

In this transformation, $\tau$ is the selective stretching parameter which varies from zero (no stretching) to large values which produce the most refinement near $z = L_2$, as seen in Figure 4.3(a) where the selected $\tau$ value is 10.

### Transformation for $r$

The transformation for independent variable $r$ is given by the following equation in order to cluster more points near $r = 0$:

$$\bar{r} = 1 - \frac{\ln\{[\beta + 1 - (r/r_1)]/[\beta - 1 + (r/r_1)]\}}{\ln[(\beta + 1)/(\beta - 1)]}, \quad 1 < \beta < \infty \tag{4.21}$$

This stretching transformation clusters more points near $r = 0$ as the stretching parameter $\beta$ approaches 1, as seen in Figure 4.3(a) where the selected $\beta$ value is 1.01.

### Transformation of Laplace's equation and boundary conditions

The transformation of Laplace's equation (Equation (4.1)) may be written as:

$$\nabla^2\phi = (\frac{\partial\bar{r}}{\partial r})^2\frac{\partial^2\phi}{\partial\bar{r}^2} + (\frac{\partial\bar{z}}{\partial z})^2\frac{\partial^2\phi}{\partial\bar{z}^2} + [\frac{\partial^2\bar{r}}{\partial r^2} + \frac{1}{r}\frac{\partial\bar{r}}{\partial r}]\frac{\partial\phi}{\partial\bar{r}} + \frac{\partial^2\bar{z}}{\partial z^2}\frac{\partial\phi}{\partial\bar{z}} = 0 \tag{4.22}$$

by chain rule. The partial derivatives of the transformation as well as the inverse functions of the transformation in Equation (4.22) can be derived analytically and are presented in Appendix A.

The transformations for the first set of boundary conditions (Equations (4.2)-(4.6)) are formed as follows:

$$\phi = 0, \quad \text{at} \quad \bar{z} = 0 \quad \text{and} \quad \bar{r}_2 \le \bar{r} \le 1.0 \tag{4.23}$$

where

$$\bar{r}_2 = 1 - \frac{\ln\{[\beta + 1 - (r_2/r_1)]/[\beta - 1 + (r_2/r_1)]\}}{\ln[(\beta + 1)/(\beta - 1)]} \tag{4.24}$$

and

$$\phi = 0, \quad \text{at} \quad \bar{z} = 1.0 \quad \text{and} \quad 0 \le \bar{r} \le 1.0 \tag{4.25}$$

$$\frac{\partial\phi}{\partial\bar{r}} = 0, \quad \text{at} \quad \bar{r} = 0 \quad \text{and} \quad \bar{z}_2 \le \bar{z} \le 1.0 \tag{4.26}$$

where

$$\bar{z}_2 = B = \frac{1}{2\tau}\ln[\frac{1 + (e^{\tau} - 1)(L_2/L_1)}{1 + (e^{-\tau} - 1)(L_2/L_1)}] \tag{4.27}$$

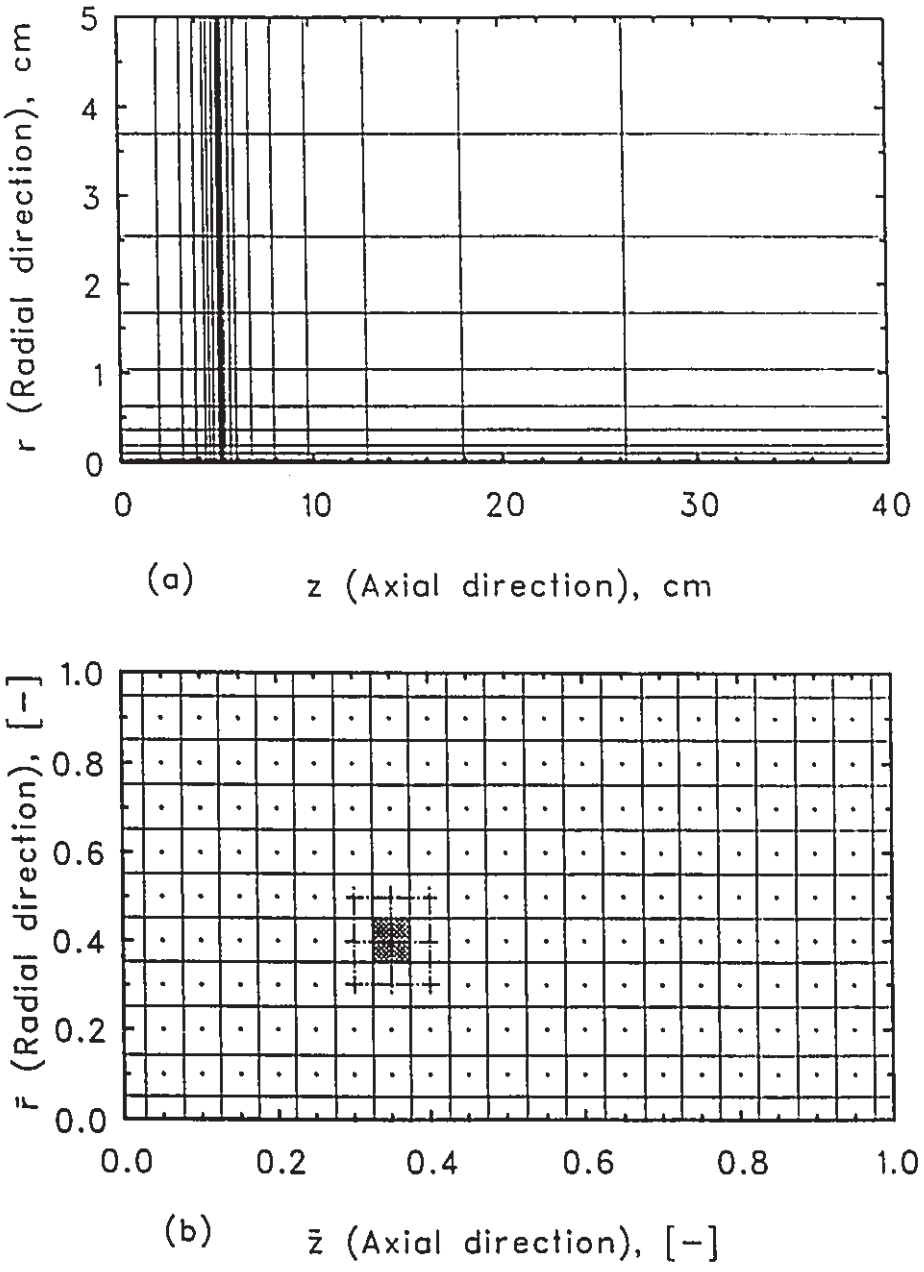


Figure 4.3: 11 × 21 Grid scheme for numerical model calculation ($\tau = 10$, $\beta = 1.01$)

(a) Physical Domain; (b) Computational Domain.

and

$$\phi = \phi_0, \quad \text{at} \quad \bar{r} = 1.0 \quad \text{and} \quad 0 \leq \bar{z} \leq \bar{z}_3 \tag{4.28}$$

where

$$\bar{z}_3 = B + \frac{1}{\tau}\sinh^{-1}\{[(L_3/L_2) - 1]\sinh(\tau B)\} \tag{4.29}$$

and

$$\phi = 0, \quad \text{at} \quad 0 \leq \bar{r} \leq \bar{r}_2 \quad \text{and} \quad 0 \leq \bar{z} \leq \bar{z}_2 \tag{4.30}$$

The transformations for the second set of boundary conditions (Equations (4.7)-(4.11)) are formed as follows:

$$\phi = 0, \quad \text{at} \quad \bar{z} = 0 \quad \text{and} \quad \bar{r}_2 \leq \bar{r} \leq 1.0 \tag{4.31}$$

where

$$\bar{r}_2 = 1 - \frac{\ln\{[\beta + 1 - (r_2/r_1)]/[\beta - 1 + (r_2/r_1)]\}}{\ln[(\beta + 1)/(\beta - 1)]} \tag{4.32}$$

and

$$\phi = 0, \quad \text{at} \quad \bar{z} = 1.0 \quad \text{and} \quad 0 \leq \bar{r} \leq 1.0 \tag{4.33}$$

$$\frac{\partial \phi}{\partial \bar{r}} = 0, \quad \text{at} \quad \bar{r} = 0 \quad \text{and} \quad \bar{z}_2 \leq \bar{z} \leq 1.0 \tag{4.34}$$

where

$$\bar{z}_2 = B = \frac{1}{2\tau}\ln[\frac{1 + (e^{\tau} - 1)(L_2/L_1)}{1 + (e^{-\tau} - 1)(L_2/L_1)}] \tag{4.35}$$

and

$$\phi = 0, \quad \text{at} \quad \bar{r} = 1.0 \quad \text{and} \quad 0 \leq \bar{z} \leq 1.0 \tag{4.36}$$

$$\phi = \phi_0, \quad \text{at} \quad 0 \leq \bar{r} \leq \bar{r}_2 \quad \text{and} \quad 0 \leq \bar{z} \leq \bar{z}_2 \tag{4.37}$$

### 4.3.2 The numerical model

In the numerical method to be described, the aim is to calculate the values of the relevant dependent variables ($\phi, \mathbf{E}, E^2$and $\nabla E^2$) at a set of chosen points called the grid

points. The algebraic equations for these values, the so called discretization equations, are derived by integrating the governing differential equation over a subdomain surrounding each grid point. These subdomains are referred to as control volumes. Figure 4.3(b) shows the computational domain for one of the grid schemes arranged in the present numerical field modelling. As seen in Figure 4.3(b), a typical control volume for an internal grid point is shaded and all internal grid points are located at the centers corresponding to their control volumes.

Conceptually, the method relies on the formation of linearized algebraic equations through the integration of governing differential equations that express the conservation of some quantities (typically mass, momentum, or electric potential energy in this case) over finite control volumes covering the problem domain.

### Grid and control volumes

For a given grid, the control volumes can be defined in different ways (Patankar, 1980). The practice chosen here is illustrated in Figure 4.3(b). A typical three dimensional control volume for an internal grid point in the cylindrical coordinate system is schematically illustrated in Figure 4.4(a). Since the axial symmetrical nature there is no variation of the dependent variables in coordinate $\theta$ direction. Therefore it can be treated as the same as that in a two dimensional cartesian coordinate system which is the shaded area shown in Figure 4.3(b) and is schematically illustrated in Figure 4.4(b).

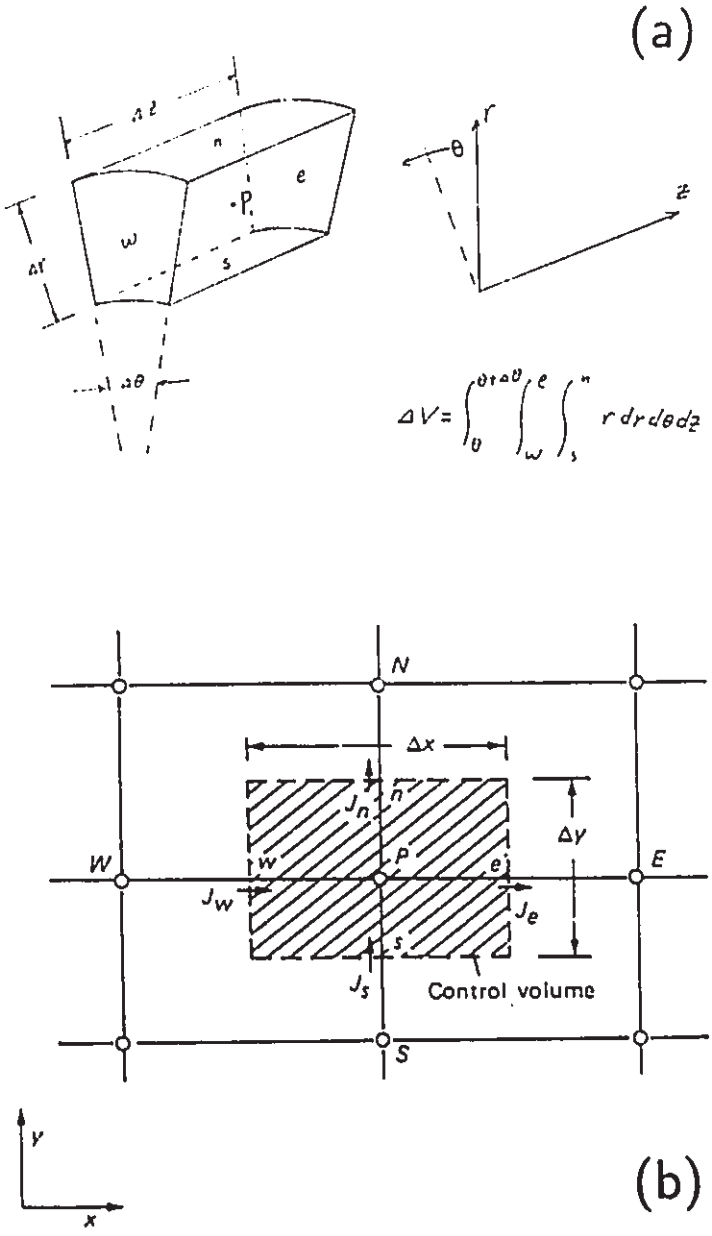


Figure 4.4: Typical control volume for an internal grid point

(a) Typical control volume in cylindrical coordinates
(b) Typical control volume in two dimensional cartesian coordinates

### Final discretization equation

Following Patankar's approach (Patankar, 1980) the integration of the Equation (4.22) over the control volume shown in Figure 4.4(b) leads to the final discretization equation as:

$$a_P\phi_P = a_E\phi_E + a_W\phi_W + a_N\phi_N + a_S\phi_S \tag{4.38}$$

where

$$a_E = D_e A(|P_e|) + \|F_e, 0\|, \qquad P_e = \frac{F_e}{D_e} \tag{4.39}$$

$$a_W = D_w A(|P_w|) + \| - F_w, 0\|, \qquad P_w = \frac{F_w}{D_w} \tag{4.40}$$

$$a_N = D_n A(|P_n|) + \|F_n, 0\|, \qquad P_n = \frac{F_n}{D_n} \tag{4.41}$$

$$a_S = D_s A(|P_s|) + \| - F_s, 0\|, \qquad P_s = \frac{F_s}{D_s} \tag{4.42}$$

and function $A(|P_i|)$ is defined from the power-law scheme (Patankar, 1980)

$$A(|P_i|) = \|0, (1 - 0.1|P|)^5\| \tag{4.43}$$

The $D_i$ and $F_i$ have been derived as follows:

$$D_e = (\frac{\partial \bar{z}}{\partial z})_e^2 \bar{r}_e \frac{\Delta \bar{r}}{(\delta \bar{z})_e} \tag{4.44}$$

$$D_w = (\frac{\partial \bar{z}}{\partial z})_w^2 \bar{r}_w \frac{\Delta \bar{r}}{(\delta \bar{z})_w} \tag{4.45}$$

$$D_n = (\frac{\partial \bar{r}}{\partial r})_n^2 \bar{r}_n \frac{\Delta \bar{z}}{(\delta \bar{r})_n} \tag{4.46}$$

$$D_s = (\frac{\partial \bar{r}}{\partial r})_s^2 \bar{r}_s \frac{\Delta \bar{z}}{(\delta \bar{r})_s} \tag{4.47}$$

$$F_e = (\frac{\partial^2 \bar{z}}{\partial z^2})_e \bar{r}_e \Delta \bar{r} \tag{4.48}$$

$$F_w = (\frac{\partial^2 \bar{z}}{\partial z^2})_w \bar{r}_w \Delta \bar{r} \tag{4.49}$$

$$F_n = [(\frac{\partial^2 \bar{r}}{\partial r^2}) + \frac{1}{r}(\frac{\partial \bar{r}}{\partial r})]_n \bar{r}_n \Delta \bar{z} \tag{4.50}$$

$$F_s = [(\frac{\partial^2 \bar{r}}{\partial r^2}) + \frac{1}{r}(\frac{\partial \bar{r}}{\partial r})]_s \bar{r}_s \Delta \bar{z} \tag{4.51}$$

where

$$(\delta \bar{z})_e = (\delta \bar{z})_w = \Delta \bar{z} \tag{4.52}$$

$$(\delta \bar{r})_n = (\delta \bar{r})_s = \Delta \bar{r} \tag{4.53}$$

$$\bar{r}_n = \bar{r}_p + \frac{1}{2}\Delta \bar{r} \tag{4.54}$$

$$\bar{r}_s = \bar{r}_p - \frac{1}{2}\Delta \bar{r} \tag{4.55}$$

$$\bar{r}_e = \bar{r}_w = \bar{r}_p \tag{4.56}$$

### Solution of the algebraic equations

It is noted that, while constructing the discretization equations, we cast them into a linear form but did not assume that a particular method would be used for their solution. Therefore, any suitable solution method can be employed at this stage. The direct methods (*i.e.*, those requiring no iteration) for solving the algebraic equations arising in two dimensional problems are much more complicated than those in one-dimensional situations, and require rather large amounts of computer memory as well as CPU time. Iterative methods are a more efficient alternative.

The iterative method for the solution of algebraic equations used in this work is the *Line Gauss-Seidel* (LGS) Solver combined with Alternating-Direction-Implicit (ADI) approach following the method by Raithby and Schneider (1988). That is, sweep from *west* to *east* on each line first and then change direction and sweep from *south* to *north* on each line using the Tri-Diagonal-Matrix-Algorithm (TDMA). Therefore one complete iteration would consist of two sweeps. The iterations are repeated until convergence of the solution has occurred as indicated by an acceptable residual between two sweeps in the last iteration.

### 4.3.3 The numerical modelling procedure

The following algorithm has been implemented to solve the discrete equations.

1. values of input data are available which include:
   - electric potential at boundary grid points;
   - parameters of the equipment cell (refer to Figures 4.1 and 4.2);
   - parameters for coordinates transformation (refer to Figures 4.3(a)(b));
   - grid arrangement scheme (grid points in both directions);
   - the criterion for iteration convergence.
2. iteration of electric potential in $r$ direction
3. iteration of electric potential in $z$ direction
4. comparison of the difference of the potential values summation between $r$ direction and $z$ direction with the preset criterion, *i.e.*$|\sum \phi^r_{i,j} - \sum \phi^z_{i,j}| \leq 10^{-6}$. If the difference meets the preset criterion, the next step will be attempted otherwise further iteration would be performed.
5. once the convergence of the iteration is reached, then begin to calculate the other quantities required, *i.e.* $\mathbf{E}, E^2$ and $\nabla E^2$ *etc.*
6. save the results in different files or print out these results for later analysis.

Figure 4.5 is the flow chart of the calculation procedure. A computer program in FORTRAN 77 to perform the numerical model calculation in this work is attached in Appendix C.

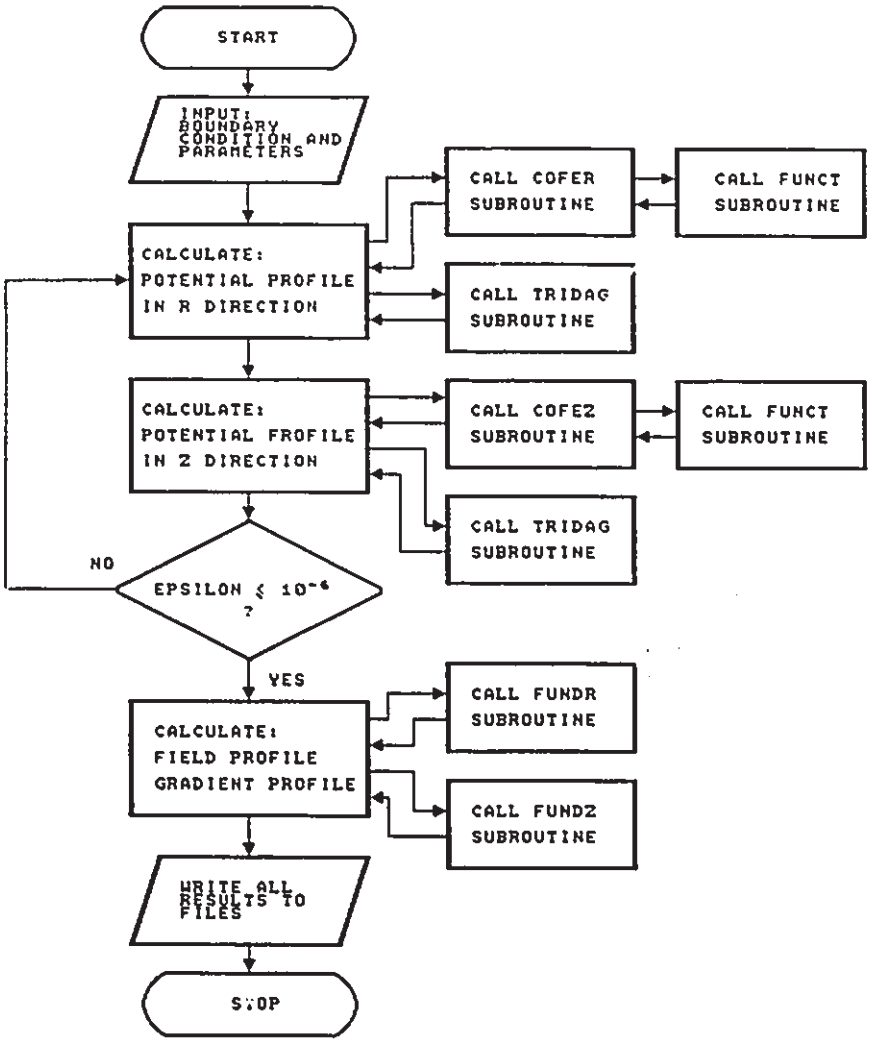


Figure 4.5: Flow chart of numerical modelling

## 4.4 Results of Numerical Modelling

The results of the numerical modelling are based on the preset parameters which can be classified as:

- parameters of equipment size: $L_1$, $L_2$, $L_3$, $r_1$, $r_2$, where $L_1$ is the total length of the cell, $L_2$ is the intrusion length of the hollow electrode, $L_3$ is the total connected length of the planar electrode, $r_1$ is the half width of the experimental cell and $r_2$ is the radius of the hollow electrode, (refer to Figures 4.1 and 4.2).
- parameters for $\beta$ and $\tau$: the proper values for $\beta$ and $\tau$ were determined by trial and error in order to cluster appropriate grid points at pre-determined positions in the physical domain (refer to Figure 4.3).
- other parameters such as grid schemes arrangement, the convergence criterion *etc.*

The values of these parameters used in the numerical modelling are summarized in Table 4.1.

### 4.4.1 Validation of the numerical model

To validate the numerical model derived for the prediction of the electric field in this work, three grid schemes have been arranged, *i.e.* 21 × 21, 21 × 41 and 11 × 21, since the solutions for an accurate numerical model should be converged on the final true values with increasing the grid points. With some approximations two analytical

Table 4.1: List of parameters for numerical modelling

| | |
|---|---|
| **Grid schemes arrangement** | $21 \times 21, \quad 21 \times 41, \quad 11 \times 21$ |
| **Stretch constant for transformation** | $\beta = 1.01, \qquad \tau = 10$ |
| **Geometric values** [cm] | $L_1 = 40, \quad L_2 = 5, \quad L_3 = 26$<br>$r_1 = 5, \quad r_2 = 0.035$ |
| **Convergence criterion*** | $\mid \sum \phi^r_{i,j} - \sum \phi^z_{i,j} \mid \leq 10^{-6}$ |

* $\phi^r_{i,j}$ are the grid iteration values along $r$ direction;
$\phi^z_{i,j}$ are the grid iteration values along $z$ direction.

solutions have also been derived near the hollow electrode for the second type of electrode connection (refer to Figure 4.2) for confirmation of the numerical results.

### Analytical electric field models

Suppose the hollow electrode used in this work is approximately considered as an isolated metal spheroid with surface potential $V_0$ in a free space, the general solution of Laplace's equation in *prolate spheroidal coordinates* can be expressed as (Moon and Spencer, 1961):

$$(\frac{\phi}{V_0}) = \frac{\ln \coth(\eta/2)}{\ln \coth(\eta_0/2)} \quad . \tag{4.57}$$

with the following boundary conditions applied:

$$\eta = \eta_0, \quad \phi = V_0 \tag{4.58}$$

and

$$\eta \to \infty, \quad \phi = 0 \tag{4.59}$$

The dimensionless electric field strength along $z$ axis is obtained from Equation (4.57):

$$(\frac{\mathbf{E}}{\mathbf{E_0}}) = \frac{\sinh^2 \eta_0}{\sinh^2 \eta} \tag{4.60}$$

where $\mathbf{E_0}$ is the electric field at $\eta_0$ and $\eta$ is the variable, in prolate spheroidal coordinates, from which the $z$ axis can be determined. Therefore the two models derived for different hollow electrode geometrical approximations in this work (Appendix B) give two different equations to calculate $z$ from $\eta$:

- **model 1**

$$z = \frac{L_2}{2}(1 + \cosh \eta) \tag{4.61}$$

- **model 2**

$$z = L_2 \cosh \eta \tag{4.62}$$

where $L_2$ is the length of hollow electrode. It is noted that $z \approx L_2$ when $\eta = \eta_0$, as the ratio of hollow electrode length over its radius is very large. The true electric field profiles near hollow electrode are expected to be in between these two models. The schematically derivations of these two models are presented in Appendix B.

### Comparison of numerical results with the analytical models

The numerical results for the second type electrode connection mode have been compared with the above analytical solutions both on the electric potentials and electric fields as shown in Figures 4.6–4.7. Figures 4.6(a) and 4.6(b) give the comparison of the electric potential profile along $z$ axis, where Figure 4.6(b) is obtained from Figure 4.6(a) after the shift of $z$ is made close to the origin. Figures 4.7(a) and 4.7(b) show the comparison of the electric field profile along $z$ axis, where Figure 4.7(b) is also obtained from Figure 4.7(a) after the shift of $z$ is made close to the origin. As seen in these Figures, the numerical solutions of three grid point arrangement are quite consistent. The maximum standard deviation of the numerical results obtained from 5 same grid points is less than 4% among the three different grid schemes up to 10 cm axial distance.

The comparison between the numerical solutions and two analytical solutions also verifies the numerical model as shown in these figures. Although the numerical solutions decay significantly fast compared with the analytical solutions over 10 cm distance along axial direction due to the different constraints of the boundary conditions used in these of models, a good agreement with these two analytical models within 10 cm distance along $z$ axis indicates the validation of the numerical model in the present calculation. The results shown in these figures also indicate that there is slight difference between two analytical solutions near the region very close to hollow electrode due to the geometry of electrode assumed in the two analytical models.

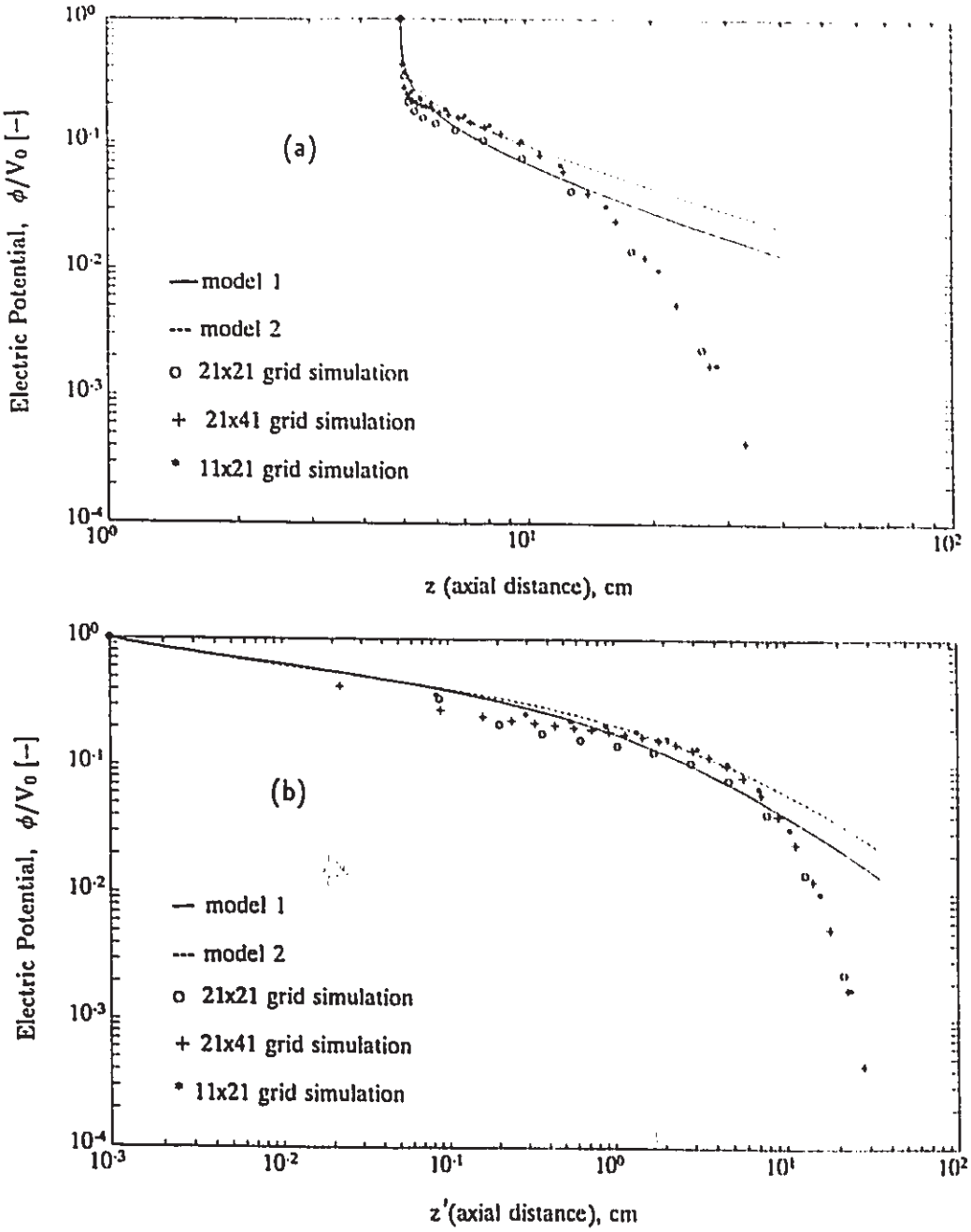


Figure 4.6: Comparison of normalized axial electric potential profile between numerical modelling & analytical solutions at the centre of cell ($r = 0$)

(a) general plot; (b) plot with $z$ shifting, $z' \approx z - L_2$

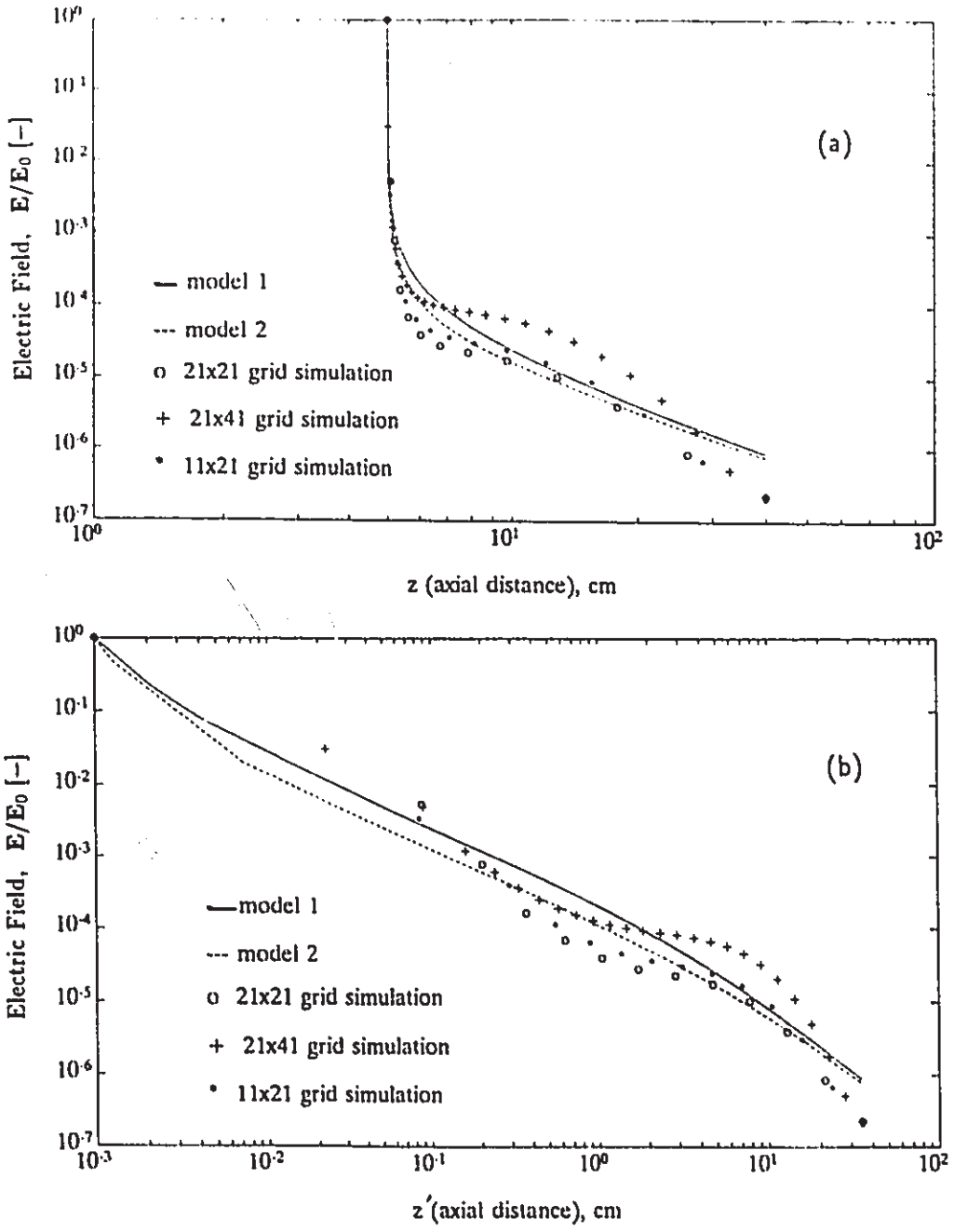


Figure 4.7: Comparison of normalized axial electric field profile between numerical modelling & analytical solutions at the centre of cell ($r = 0$)

(a) general plot; (b) plot with $z$ shifting, $z' \approx z - L_2$

### 4.4.2 Prediction of the applied electric field

The numerical modelling of the electric potential and field for the 21 × 41 grid arrangement are shown in Figures 4.8 and 4.9 respectively, for both electrode connection modes, *i.e.* (a) hollow electrode nozzle is connected to the ground while planar electrodes are connected to high voltage power supply source; (b) hollow electrode nozzle is connected to high voltage power supply source while planar electrodes are connected to the ground. The electric potential distribution for connection mode (a) is shown in Figure 4.8(a) while the electric potential distribution for connection mode (b) is shown in Figure 4.8(b). The magnitude of numerical electric field results are then can be calculated based on the electric potential distributions of these two different connection modes, as shown in Figure 4.9. The magnitude of electric field profiles for connection mode (a) is shown in Figure 4.9(a) while the magnitude of electric field profiles for connection mode (b) is shown in Figure 4.9(b).

The electric field near the hollow electrode is higher for connection mode (b) compared with the electric field for connection mode (a) based on the results shown in Figure 4.9(a) and Figure 4.9(b). However, for connection mode (b) there is only one high electric field intensity region which is near the hollow electrode; while for connection mode (b), there are two high electric field intensity regions: one is near the hollow electrode the other is located at planar electrodes which is connected to the 15 kV applied voltage. This can be seen more clearly from the figures in Appendix D where the comparison of these two different types of electric field profiles at various radial levels are plotted separately.

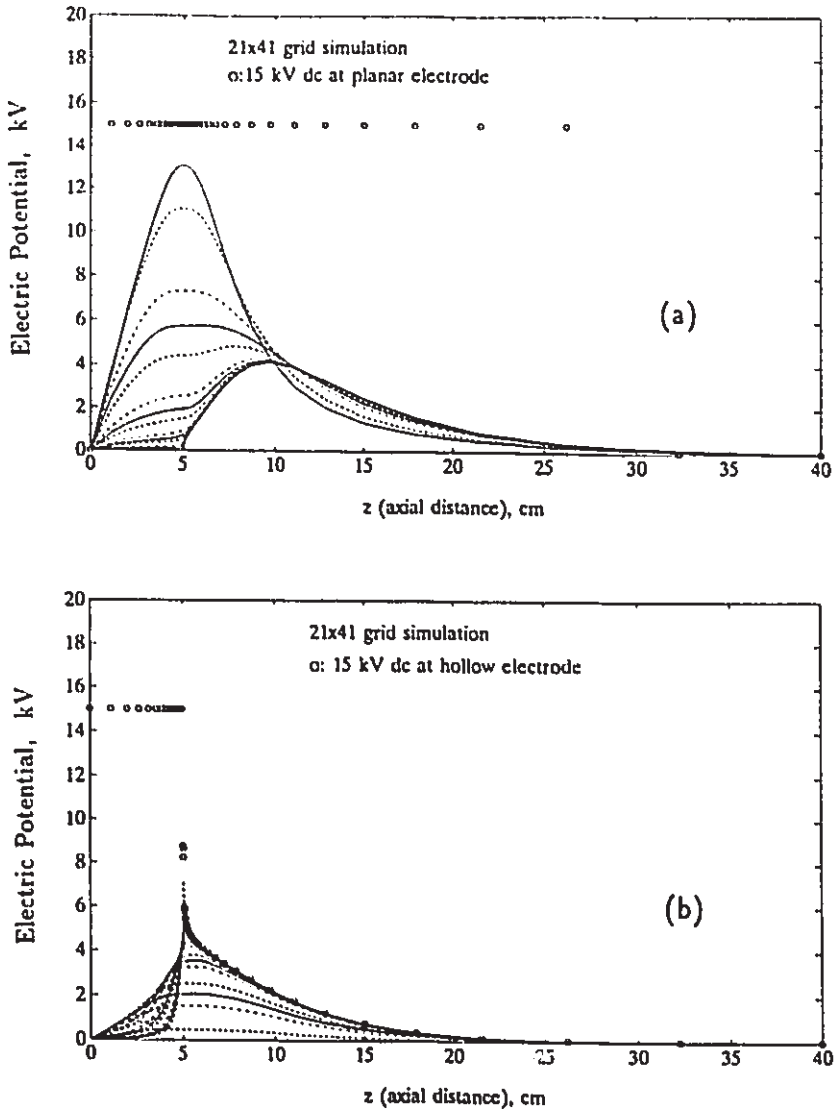


Figure 4.8: Axial electric potential profiles for various radial positions

(a) 15 kV dc applied to the planar electrode;
(b) 15 kV dc applied to the hollow electrode

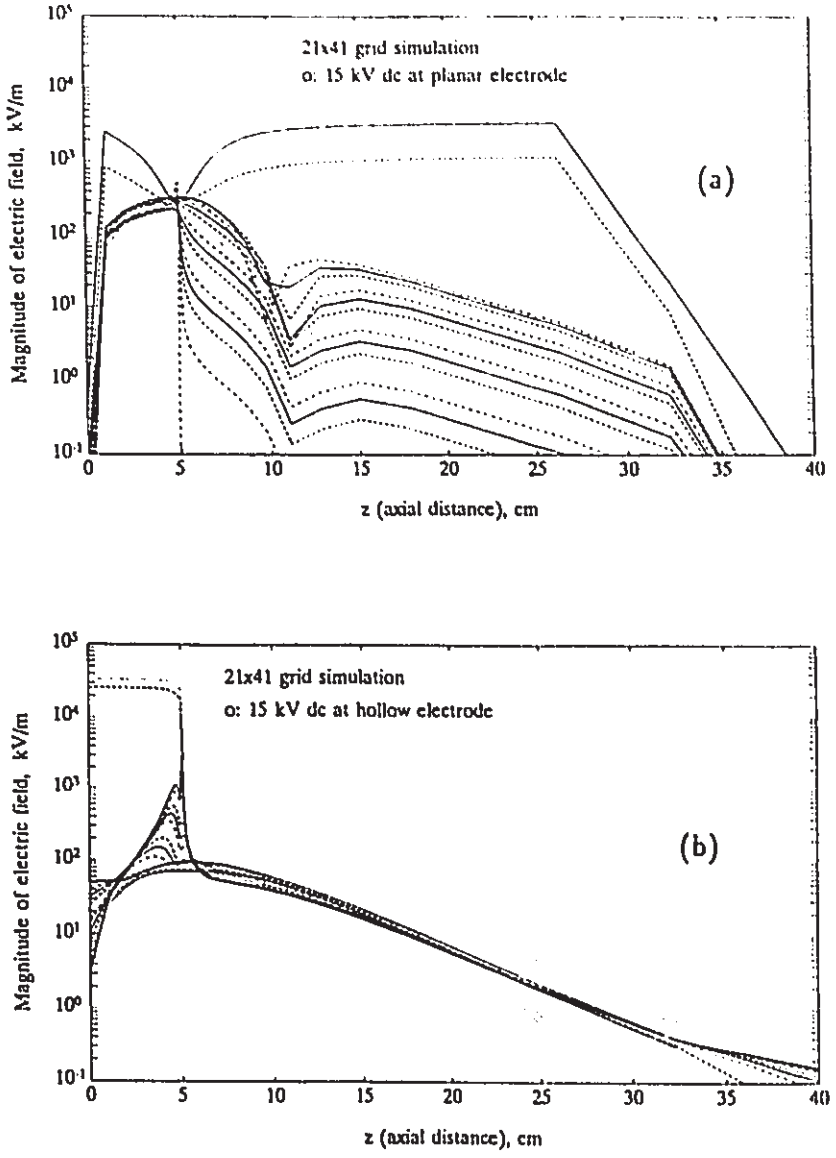


Figure 4.9: Magnitude of axial electric field profiles for various radial positions

(a) 15 kV dc applied to the planar electrode;
(b) 15 kV dc applied to the hollow electrode

### 4.4.3 Prediction of EHD forces on spherical droplets

The prediction of EHD forces on droplets can be performed using Equations (4.13)-(4.15), with an additional assumption on electric charge information, once the numerical results of the electric field and the gradient of field square are obtained. The EHD forces predicted in this work only consider the magnitude of the quantities from which the comparisons are made among three different components of EHD forces.

#### EHD force component: the gradient of electric pressure term

The first term in Equation (4.12) is EHD force on the droplet contributed by the gradient of electric pressure component, for a spherical drop with the dielectric constant values given in Table 3.3, which can be expressed based on Equation (4.13) as:

$$\{-\nabla p_e\}_{i,j} = 2.06 \times 10^{-10}\{\nabla E^2\}_{i,j} \quad [\mathrm{N/m^3}] \tag{4.63}$$

#### EHD force component: the electrophoretic term

The second term in Equation (4.12) is EHD force on the droplet contributed by the electrophoretic component which depends on the droplet charge as well as the local electric field intensity. The prediction of this EHD component is obtained with the following assumption made on droplet charge decay. Suppose a spherical droplet can acquire charge from hollow electrode with an initial volume charge density, $\rho_{ed}^{*}$. When the droplet carried with charge travels away from hollow electrode the droplet charge density is assumed to decay exponentially with the distance away by $\mathcal{R}_{i,j}$ from hollow electrode as:

$$\{\rho_{ed}\}_{i,j} = \rho_{ed}^{*}\, e^{-s\mathcal{R}_{i,j}} \tag{4.64}$$

where $s$ is the decay constant and can be determined from the charge carried by droplets at the position of the Faraday cup. $\mathcal{R}_{i,j}$, the distance away from hollow

electrode may be expressed as:

$$\mathcal{R}_{i,j} = \sqrt{(z_{i,j} - L_2)^2 + (r_{i,j} - r_2)^2} \tag{4.65}$$

where $z$ is the axial direction, $r$ is the radial direction, $L_2$ and $r_2$ are the length and radius of hollow electrode. This assumption is supported by the experimental observations which will be discussed in Chapter 6.

Thus for a spherical drop with the dielectric constant values given in Table 3.3 and from Equation (4.14), the second term in Equation (4.12) can be expressed as:

$$\{\mathrm{f}_{e1}\}_{i,j} = 0.0782\{\rho_{ed}\}_{i,j}\{\mathbf{E}\}_{i,j} \quad [\mathrm{N/m^3}] \tag{4.66}$$

**EHD force component: the dielectrophoretic term**

The third term in Equation (4.12) is EHD force on the droplet contributed by the dielectrophoretic component, for a spherical drop with the dielectric constant values given in Table 3.3, which can be expressed based on Equation (4.15) as:

$$\{\mathrm{f}_{e2}\}_{i,j} = 0.2693 \times 10^{-10}\{\nabla E^2\}_{i,j} \quad [\mathrm{N/m^3}] \tag{4.67}$$

It is noted that Equation (4.67) is similar to Equation (4.63) except that the constant in Equation (4.67) is almost eight times smaller than the constant in Equation (4.63). This means that the EHD force due to negative electric pressure gradient is almost eight times stronger than that due to dielectrophoretic force acting on a spherical droplet in the present system.

The numerical results of the EHD forces on spherical droplet based on the $21 \times 41$ grid arrangement are shown in Figures 4.10–4.12 respectively for both connection modes described previously. Figure 4.10 is the predicted EHD force magnitude profiles due to the component of negative electric pressure gradient. Figure 4.11 is the predicted EHD force magnitude profiles due to the electrophoretic component, where the drop volume charge density at hollow electrode tip, $\rho_{ed}^{*}$, is assumed to be

0.75 $C/m^3$ and the constant, $s$, is determined as 0.09 based on the averaged result of charge density measured at Faraday cup. Figure 4.12 is the predicted EHD force magnitude profile due to the dielectrophoretic component. In order to evaluate the relative importance of these EHD force components on droplet, the force due to gravity effect ($\Delta\rho g$), is also plotted with the horizontal lines shown in Figures 4.10–4.12. Several comments can be made from Figures 4.10–4.12 as summarized below.

- Compared with the effect of gravity, the EHD forces acting on droplet are dominant forces only near the hollow electrode region for the second type of electrode connection. This is consistent with the experimental observations.

- The magnitude of both electric pressure component and the dielectrophoretic component can compete with the electrophoretic component only at the hollow electrode tip because these two components decay very fast from the hollow electrode and immediately become negligible compared with the gravity effect. On the other hand, the electrophoretic component decay relatively slower, therefore this EHD force component is still dominant compared with the gravity effect up to certain distance (approximately 7-8 cm away from hollow electrode tip).

- As mentioned in the previous section, there is a second highest electric field region at the location near the planar electrode for connection mode (1). All three EHD force components at this region are also much higher (1–2 orders of magnitude higher than the gravity effect) and decay slowly before they become negligible. This means that the droplet in this location would be controlled by these EHD forces. This is also consistent with the experimental observations.

The relative importance of these EHD force effects can be seen more clearly in figures attached in Appendix D where the three EHD force components can be compared in figures at different radial levels along with the constant gravity effect.

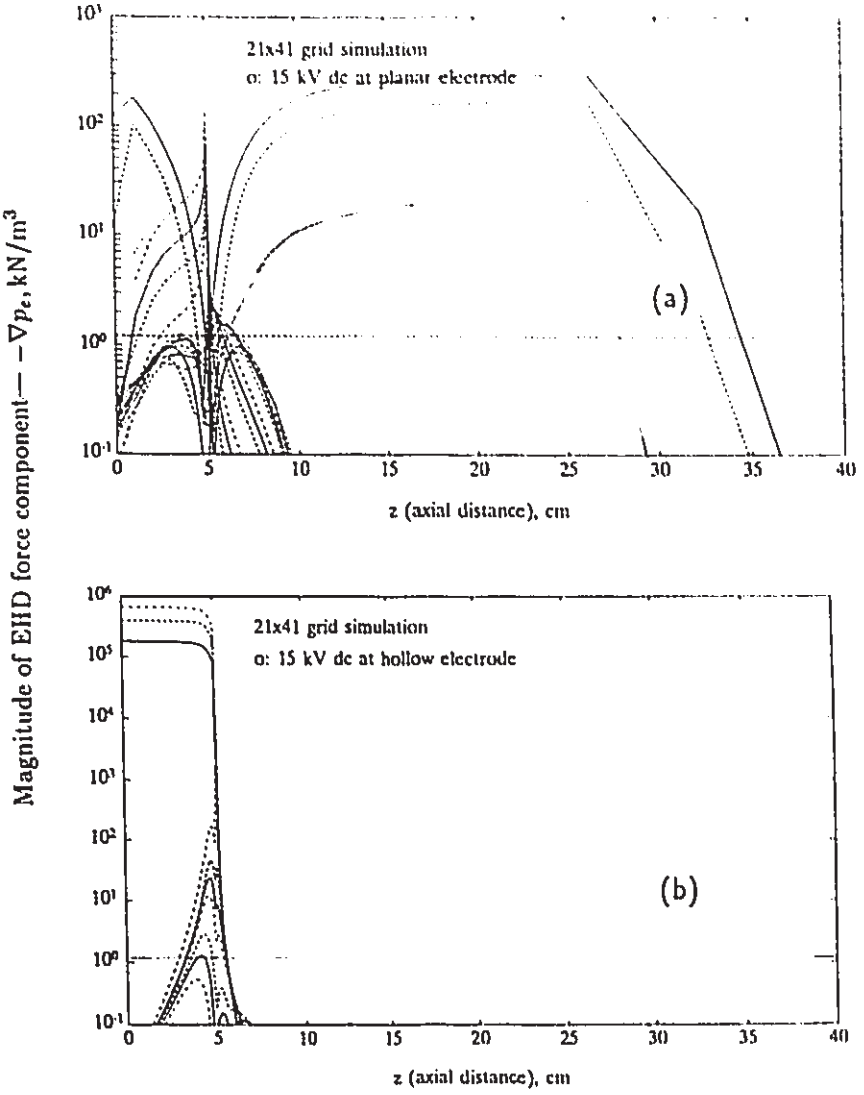


Figure 4.10: Magnitude of EHD force component: $-\nabla p_e$ along the axial distance for various radial positions

(a) 15 kV dc applied to the planar electrode;
(b) 15 kV dc applied to the hollow electrode

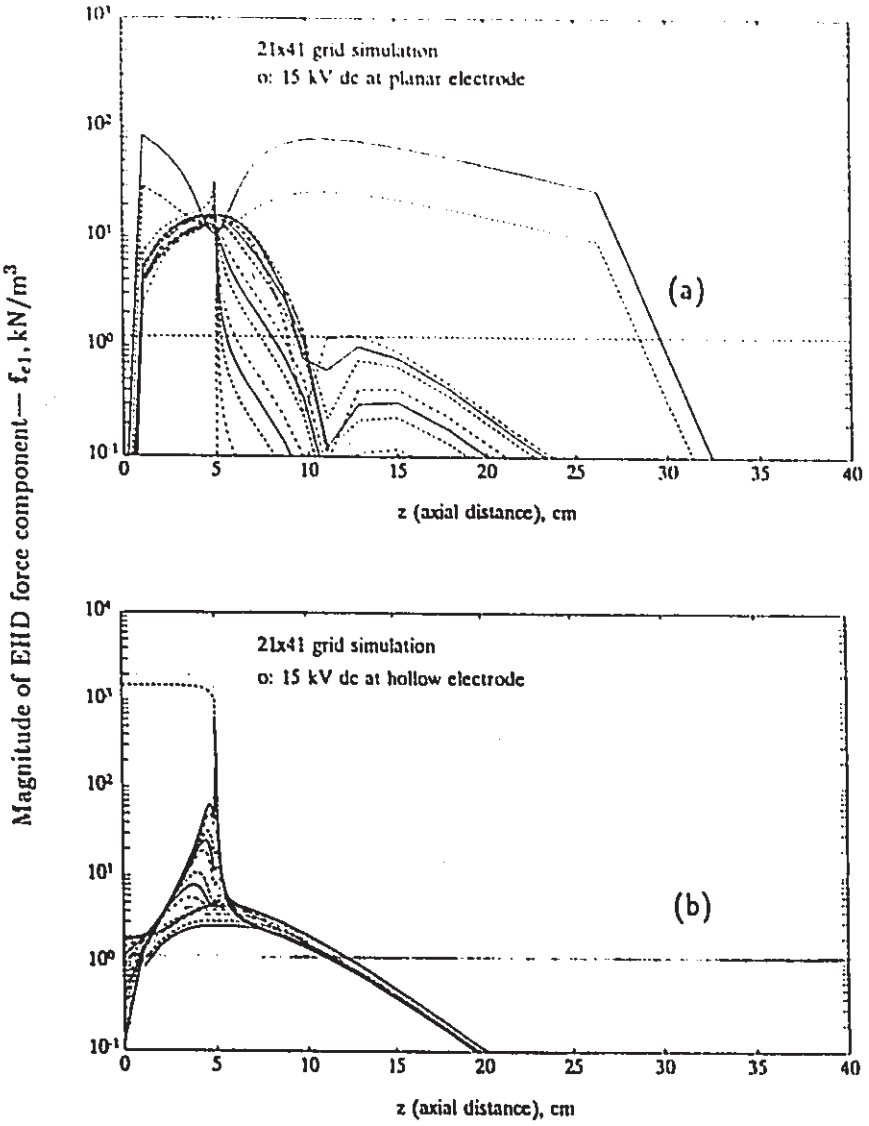


Figure 4.11: Magnitude of EHD force component: $f_{e1}$ ($\rho^*_{cd} = 0.75$ C/m$^3$; $s = 0.09$) along the axial distance for various radial positions

(a) 15 kV dc applied to the planar electrode;
(b) 15 kV dc applied to the hollow electrode

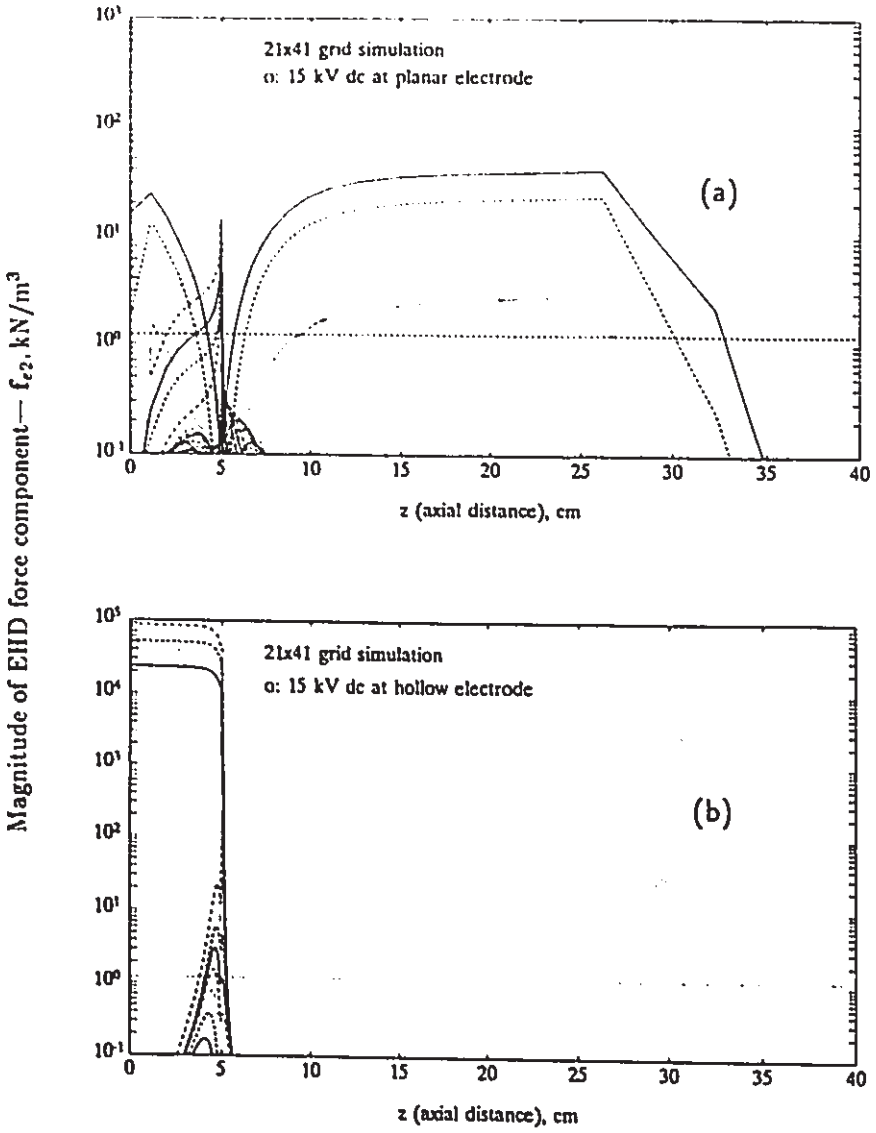


Figure 4.12: Magnitude of EHD force component: $f_{e2}$ along the axial distance for various radial positions

(a) 15 kV dc applied to the planar electrode;
(b) 15 kV dc applied to the hollow electrode

# Chapter 5

# Droplet Formation and Motion in an Inclined Cell in the Absence of Electric Field

## 5.1 Introduction

The mechanisms of droplet formation and motion in liquid-liquid systems, which are fundamental to any analysis of the rate of mass transfer and the separation processes between two liquid phases, have been studied by many authors over the decades. When a liquid of density $\rho_d$ issues steadily from a nozzle into an immiscible liquid of density $\rho_c$, drops may form directly at the tip of the nozzle or form at the end of a disintegrating cylindrical jet. In general, formation of drops occurs close to the nozzle tip at low flow rate while as the flow rate increasing a critical flow, $Q_{jet}$, is reached at which a jet forms. Studies on droplet formation have been mainly confined to the discrete drop regime and have been particularly concerned with the droplet release from a nozzle or orifice immersed in another quiescent liquid. The motion of a spherical droplet immersed in another immiscible liquid under steady state conditions

has also been studied extensively.

Four major forces can act on a drop during the process of drop formation at a nozzle submerged in another quiescent immiscible liquid: (Kumar and Kuloor, 1970)

- the buoyancy force due to the density difference between the two liquids;
- the inertial force associated with liquid flowing out of the nozzle which acts to separate the drop from the nozzle;
- the interfacial tension force at the nozzle tip, tending to keep the drop attached to the nozzle;
- the drag force due to the movement of the expanding drop also acting to keep the drop attached to the nozzle.

For drops formed very slowly, such that inertial and drag forces can be neglected, Harkins and Brown (1919) developed an expression for predicting the so-called "static drop volume". For drops formed more rapidly so that inertial and drag forces become significant, two types of correlations have been suggested to predict the droplet size from the mechanisms of formation of the droplets: the force balance model and the momentum balance model. The force balance model was defined by Hayworth and Treybal (1950). The momentum balance model was developed by Rao *et al.* (1966); Scheele and Meister (1968); Kagan *et al.* (1973); Kumar and Kuloor (1970); and Chazal and Ryan (1971). Unfortunately, none of the models available for drop formation can be selected for use with complete confidence (Clift *et al.*, 1978).

The flow around a spherical droplet moving steadily in a viscous fluid was obtained independently by Hadamard (1911) and Rybczynski (1911) for creeping flow and by Levich (1962) for potential flow. In the intermediate flow range, the characteristics of the flow were established mainly by approximate or numerical solutions

(Hamielec and Johnson, 1962; Hamielec *et al.*, 1963; Hamielec and Hoffman, 1967; Hamielec *et al.*, 1967; Yamaguchi *et al.*, 1974; Abdel-Alim and Hamielec, 1975).

The subject of this chapter is mainly the formation and motion of a single droplet in a viscous mineral oil in the absence of electric field at room temperatures. Attention is concentrated on the low dispersed phase flow rate region where single droplets form directly at the nozzle tip. The main independently varied parameters involved in this work are the dispersed phase flow rate, inclined angle of the nozzle and diameter of the nozzle. Since none of the models currently available for droplet formation can be selected to use in this work with confidence the new models have been derived from this work which include the buoyancy force, the interfacial tension force and the drag. Inertial force is ignored because of the low flow rate employed.

Section 5.2 summarizes the theory of low Reynolds Number flow (creeping flow) for the completeness of the subject. Models of droplet formation follow in section 5.3. Section 5.4 Presents discussions on drop size and velocity as well as the other effects on drop formation and motion based on the investigations in this work.

## 5.2 Theory of Low Reynolds Number Flow

### 5.2.1 Navier-Stokes equation

The fundamental physical laws governing formation and motion of droplets immersed in an immiscible fluid at constant temperature are Newton's second law and the principle of conservation of mass. Application of Newton's second law to an infinitesimal element of an incompressible Newtonian fluid of density $\rho$ and constant viscosity $\mu$, acted upon by gravity as the only body force, leads to the Navier-Stokes equation of motion (Bird *et al.*, 1960):

$$\rho\frac{D\mathbf{U}}{Dt} = \rho\mathbf{g} - \nabla p + \mu\nabla^2\mathbf{U} \tag{5.1}$$

The term on the left-hand side, arising from the product of mass and acceleration, can be expanded using the expression for the substantial derivative operator:

$$\frac{D}{Dt} = \frac{\partial}{\partial t} + \mathbf{U} \cdot \nabla \tag{5.2}$$

where the first term, called the local derivative, represents changes at a fixed point in the fluid and the second term, the convective term, accounts for changes following the motion of the fluid. On the right-hand side of Equation (5.1), the term $\rho \mathbf{g}$ is the gravity force acting on unit volume of the fluid; and the other two terms represent the surface force on the element of fluid. Application of the principle of conservation of mass to an incompressible fluid yields the overall continuity equation (Bird *et al.*, 1960)

$$\nabla \cdot \mathbf{U} = 0 \tag{5.3}$$

In principle, Equations (5.1) and (5.3) are sufficient for solution of the problem with appropriate boundary conditions. In practice, the solution to the complete Navier-Stokes equation for flows in two or three dimensions is very difficult due to the non-linear convective acceleration term, $\mathbf{U} \cdot \nabla \mathbf{U}$. However, for axial symmetric flows of incompressible fluids with constant $\rho$ and $\mu$, *e.g.* droplet moving in an unbounded medium, the equation of motion can be expressed in a relatively simple form by the introduction of the stream function, $\psi$. Therefore Equation 5.1 may be expressed as the stream function in spherical coordinate system with the origin placed at the centre of the sphere (Bird *et al.*, 1960):

$$\frac{\partial}{\partial t}(E^2\psi) + \frac{1}{r^2 \sin\theta}\frac{\partial(\psi, E^2\psi)}{\partial(r,\theta)} - \frac{2E^2\psi}{r^2 \sin\theta}\left(\frac{\partial \psi}{\partial r}\cos\theta - \frac{1}{r}\frac{\partial \psi}{\partial \theta}\sin\theta\right) = \nu E^4 \psi \tag{5.4}$$

where the operator, $E^2$ is

$$E^2 \equiv \frac{\partial^2}{\partial r^2} + \frac{\sin\theta}{r^2}\frac{\partial}{\partial \theta}\left(\frac{1}{\sin\theta}\frac{\partial}{\partial \theta}\right) \tag{5.5}$$

### 5.2.2 Creeping flow around a sphere

It has been known that the Reynolds number expresses the relative magnitude of inertial to viscous forces, consequently, for $Re << 1$ the inertial terms can be eliminated from the equation of motion, *i.e.* Equation (5.1) or (5.4). Generally, the Reynolds number for flow around a sphere, $\mathrm{Re}_d$ is defined by

$$\mathrm{Re}_d = \frac{v_t d}{\nu_c} \tag{5.6}$$

where $v_t$ is the steady-state (terminal) velocity of rise or fall of the droplet, $d$ is the diameter of the droplet, and $\nu_c$ is the kinematic viscosity of the continuous phase.

The subject of low Reynolds number flow also known as *creeping flow*, was introduced by Stokes (1851) in his study of flow past a rigid sphere. Stokes assumed to the first approximation that inertial effects in the fluid motion could be neglected compared to friction effects. Therefore the term on the right-hand side of Equation (5.4) dominates, so that the convective derivative may be neglected and the equation of motion may be simplified as

$$E^4\psi = 0 \tag{5.7}$$

Stokes found an exact solution of this equation to be:

$$\psi = (\frac{A}{r} + Br + Cr^2 + Dr^4)\sin^2\theta \tag{5.8}$$

**Stokes' solution for a rigid sphere**

The boundary conditions for steady creeping flow past a rigid sphere are described in terms of stream functions as (Bird *et al.*, 1960)

1. Uniform stream flow in the - z direction at large distances from the sphere:

$$\psi = -\frac{1}{2}v_0 r^2 \sin^2\theta \qquad \text{as } r \to \infty \tag{5.9}$$

2. The no-slip conditions at the surface of rigid sphere:

$$v_r = -\frac{1}{r^2 \sin\theta}\frac{\partial \psi}{\partial \theta} = 0 \qquad \text{at } r = a \tag{5.10}$$

$$v_\theta = +\frac{1}{r \sin\theta}\frac{\partial \psi}{\partial r} = 0 \qquad \text{at } r = a \tag{5.11}$$

The constants $A, B, C, D$ in General solution of Equation 5.8 can be determined using above boundary conditions and the final solution of stream function for fluid moving around a rigid sphere is

$$\psi = \frac{1}{2} v_0 r^2 [1 - \frac{3}{2}(\frac{a}{r}) + \frac{1}{2}(\frac{a}{r})^3] \sin^2\theta \tag{5.12}$$

All other properties of the flow can be obtained by using Equation (5.12) in the appropriate equations to determine the velocity components, the pressure distribution, and eventually the total drag force:

$$\mathbf{F}_{Stokes} = 6\pi\mu_c a v_0 = 3\pi\mu_c d v_0 \tag{5.13}$$

This expression is known as *Stokes' law*. The drag coefficient is therefore

$$C_D = \frac{24}{\mathrm{Re}_d} \tag{5.14}$$

The well known expression for the terminal velocity of a rigid sphere in creeping flow is obtained by equating the total drag of Equation (5.13) to the net gravity force, $\pi d^3 \Delta\rho g/6$, giving

$$v_t = \frac{\Delta\rho g d^2}{18\mu_c} \tag{5.15}$$

### Hadamard-Rybczynski solution for a spherical droplet

The behaviour of fluid spheres in low Reynolds Number flow in an infinite fluid medium can be analyzed, by introducing modifications to Stokes' solution for rigid spheres. Solutions by Hadamard (1911) and those done independently by Rybczynski (1911) using the Stokes solution have shown that the changes in boundary conditions

at the droplet interface yields a significant change in the velocity of a falling drop. A fluid sphere is considered, with its interface assumed to be completely free from surface-active contaminants, so that the interfacial tension is constant. It is assumed that both $Re$ and $\mathrm{Re}_d$ are small so that Equation (5.7) can be applied to both fluid, *i.e.*

$$E^4\psi = E^4\psi_d = 0 \tag{5.16}$$

The boundary conditions in the Hadamard-Rybczynski model are:

1. far from the drop the flow is undisturbed and parallel:

$$\psi = -\frac{1}{2}v_0 r^2 \sin^2\theta \qquad \text{as } r \to \infty \tag{5.17}$$

2. the normal components of the inner and outer velocities are zero at the drop interface, *i.e.* there is no flow across the interface:

$$\psi = \psi_d = 0 \qquad \text{at } r = a \tag{5.18}$$

3. tangential velocity components are continuous at the interface:

$$\frac{\partial\psi}{\partial r} = \frac{\partial\psi_p}{\partial r} \qquad \text{at } r = a \tag{5.19}$$

4. the tangential and the normal components of the viscous shear stress are continuous at the interface:

$$\frac{\partial}{\partial r}\left(\frac{1}{r^2}\frac{\partial\psi}{\partial r}\right) = \kappa\frac{\partial}{\partial r}\left(\frac{1}{r^2}\frac{\partial\psi_d}{\partial r}\right) \qquad \text{at } r = a \tag{5.20}$$

where $\kappa = \mu_d/\mu_c$ is the ratio of viscosity,

$$p - 2\mu_c\frac{\partial}{\partial r}\left(\frac{1}{r^2\sin\theta}\frac{\partial\psi}{\partial\theta}\right) + \frac{2\sigma}{a} = p_d - 2\mu_d\frac{\partial}{\partial r}\left(\frac{1}{r^2\sin\theta}\frac{\partial\psi_d}{\partial\theta}\right) \qquad \text{at } r = a \tag{5.21}$$

The solution of Equation (5.16) with boundary conditions, Equations (5.17 to (5.21) can be found as (Clift *et al.*, 1978)

- for the external liquid:

$$\psi = -\frac{v_0 r^2 \sin^2\theta}{2}[1 - \frac{2+3\kappa}{2+2\kappa}(\frac{a}{r}) + \frac{\kappa}{2+2\kappa}(\frac{a}{r})^3] \tag{5.22}$$

- and for the interior liquid:

$$\psi_d = \frac{v_0 r^2 \sin^2\theta}{4(1+\kappa)}[1 - (\frac{r}{a})^2] \tag{5.23}$$

These equations lead to the terminal velocity and drag coefficient for the droplet as

$$v_t = \frac{g d^2 \Delta\rho}{18\mu_c}(\frac{1+\kappa}{2/3+\kappa}) \tag{5.24}$$

and

$$C_D = \frac{24}{\mathrm{Re}_d}(\frac{2+3\kappa}{3+3\kappa}) \tag{5.25}$$

The solution predicts that all drops moving in the Stokes regime will have internal circulation. This has not been found experimentally; there appears to be a critical size below which circulation does not exist. Moreover, surface-active contaminants can cause significant changes in internal circulation.

An important result of the theory of creeping flow is that spherical assumption of the droplet is consistent with the other assumptions in the derivation. Once the creeping flow assumption is valid, *i.e.* the inertial forces can be ignored, drops or bubbles should be spherical in shape. Even the effect of surface-active contaminants on the shape of the drops is also negligible. Thus if Reynolds numbers are very low, bubbles and drops remain spherical no mater how small the surface tension forces. (Clift *et al.*, 1978)

Strictly, the theory of creeping flow is effective only when $\mathrm{Re}_d < 1$, and the theory of droplet motion for $\mathrm{Re}_d > 1$ has not been fully developed yet. However in practice, it can be used at Reynolds Number, $\mathrm{Re}_d$ substantially greater than unity since the characteristic laminar phenomena persist more or less unchanged up to about $\mathrm{Re}_d \simeq 50$ (Davies, 1972).

## 5.3 Models of Droplet Formation at Inclined Hollow Nozzles

The droplet formation process can be described by a modified version of the approach originally developed by Davidson and Schüler (1960) for the formation of gas bubbles at a nozzle or orifice in a viscous liquid. In this method, the growing bubble is assumed to form at a constant volume flow rate and to be spherical in shape. During the growth process, the centre of the bubble begins to move away from the nozzle. A dynamic balance of forces is written for the growing bubble, and detachment is assumed to occur as the rear surface of the bubble passes the centre of the nozzle.

Figure 5.1(a) is a photograph of a pendent droplet before detachment from the nozzle and Figure 5.1(b) is the illustration of the model for droplet formation. The interfacial tension effect on the droplet formation with different inclined angles may be expressed approximately as follows:

$$\mathbf{F}_s = \pi d_0 \sigma \sin\theta \tag{5.26}$$

based on the approximation of the nozzle geometry as shown in Figure 5.1(b).

In the model development, forces due to gravity (buoyancy), surface tension and drag are considered. Creeping flow is assumed, so inertial terms are ignored. Droplet growth at the nozzle is assumed to occur in two stages. In the initial stage, for which surface forces exceed gravity forces, the centre of the drop is assumed to remain stationary at the nozzle ($S = 0$), so there is no drag term. The volume of the drop is given by:

$$\frac{\pi d^3}{6} = Qt \tag{5.27}$$

The stationary growth period ends when the gravity and vertically acting surface forces balance:

$$\mathbf{F}_g = \mathbf{F}_s \tag{5.28}$$

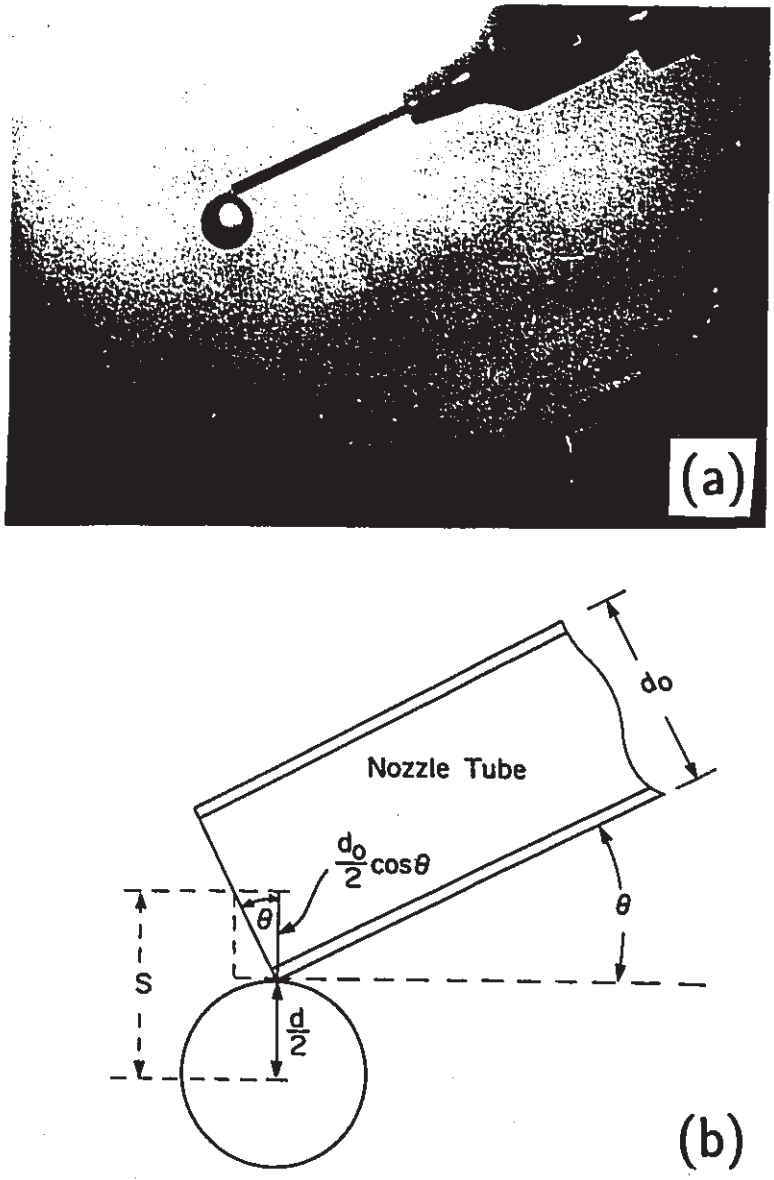


Figure 5.1: Drop detachment in the absence of electric field

(a) Photograph at 30° inclination
(b) Model sketch showing nomenclature

*i.e.*

$$\frac{\pi d^3 g \Delta\rho}{6} = \pi d_0 \sigma \sin\theta \tag{5.29}$$

The vertical component of the surface force takes account of the angle of inclination of the nozzle, $\theta$. Equation (5.29) permits calculation of the equilibrium droplet diameter:

$$d_e = (\frac{6 d_0 \sigma \sin\theta}{g\Delta\rho})^{\frac{1}{3}} \tag{5.30}$$

When $d > d_e$, the centre of the drop moves away from the centre of the nozzle; but the drop does not detach until the distance moved is given by

$$S = \frac{(d + d_0 \cos\theta)}{2} \tag{5.31}$$

This limit is shown in Figure 5.1(b) which is based upon the photograph in Figure 5.1(a). While the droplet is moving, there is a drag force $\mathbf{F}_d$ which opposes gravity, so the balance of forces becomes

$$\mathbf{F}_g = \mathbf{F}_s + \mathbf{F}_d \tag{5.32}$$

The terms $\mathbf{F}_g$ and $\mathbf{F}_s$ are those in Equation (5.29), while the drag force is calculated assuming creeping flow around a non-circulating sphere, i.e. Equation (5.13 is applied with the substitution of velocity by $dS/dt$:

$$\mathbf{F}_d = 3\pi\mu_c d(\frac{dS}{dt}) \tag{5.33}$$

Hence, from Equations (5.32) and (5.33)

$$\frac{dS}{dt} = \frac{g d^2 \Delta\rho}{18\mu_c} - \frac{d_0 \sigma \sin\theta}{3\mu_c d} \tag{5.34}$$

This equation can be transformed into a single variable equation by differentiation of Equation (5.27):

$$dt = d(\frac{\pi d^3}{6Q}) = (\frac{\pi d^2}{2Q})dd \tag{5.35}$$

Hence,

$$\frac{dS}{dd} = \frac{\pi g d^4 \Delta\rho}{36 Q \mu_c} - \frac{\pi d_0 \sigma d \sin\theta}{6 Q \mu_c} \tag{5.36}$$

Integration is carried out using the boundary condition $S = 0$ at $d = d_e$

$$S = \frac{\pi g \Delta\rho (d^5 - d_e^5)}{180 Q \mu_c} - \frac{\pi d_0 \sigma \sin\theta (d^2 - d_e^2)}{12 Q \mu_c} \tag{5.37}$$

At the point of drop detachment, $S$ is given by Equation (5.31). Equations (5.31) and (5.37) are both satisfied if:

$$\frac{6 Q \mu_c}{\pi} = \frac{[\frac{g\Delta\rho(d^5 - d_e^5)}{15} - (d_0 \sigma \sin\theta)(d^2 - d_e^2)]}{(d + d_0 \cos\theta)} \tag{5.38}$$

This equation gives the drop diameter at detachment as an implicit function of dispersed flow rate, nozzle diameter, angle of inclination and system properties. For the case of $Q = 0$ it reduces to $d = d_e$ according to Equation (5.30); but for finite flow rates, $d$ exceeds $d_e$ due to the viscous drag term.

An alternative, simpler model assumes that the motion of the centre of the growing drop begins as soon as it appears at the nozzle. According to Equation (5.36) this results in negative velocities when $d < d_e$, which is physically rather unrealistic; the drop centre can move outwards only when $d > d_e$. When the value of $d_e$ is set equal to zero in the simplified model, the drop diameter at detachment is the same as given by Equation (5.38).

## 5.4 Discussions

### 5.4.1 Spherical shape of the formed droplet

When drops are in free rise or fall in infinite media under the influence of gravity, their shape can be closely approximated as spherical if interfacial tension and/or viscous forces are much more important than inertial forces as mentioned in the section 5.2.

In the present investigation, the droplet formed at the nozzle at very low flow rates in the absence of an electric field is in the single droplet regime. The forming

droplet has dimensions significantly bigger than the size of the nozzle due to high viscosity of the continuous phase. It may be assumed that the interfacial tension and the viscous drag are much more important than the inertia during the slow drop formation period. The dominant effects of interfacial tension and viscous drag are evident from the uniformly spherical shapes of the droplets which were observed visually and measured from photographs under different experimental conditions. Figure 5.2 shows a typical image taken from experiments.

The spherical drop shapes are also confirmed by an application of the generalized graphical correlation (Clift *et al.*, 1978) for bubbles and drops in unhindered gravitational motion through liquids in terms of three dimensionless group numbers, *i.e.* the Eötvös number, Eo; the Morton number, M; and the Reynolds number, $Re_d$. For the experimental conditions used in the present study, Eo varies from 1 to 3; $Re_d$ is less than 0.22 and M is equal to 2.22. Thus, all the formed drops should be of spherical shape according to this generalized graphical correlation (see Figure 5.3).

### 5.4.2 Effect of nozzle sizes and inclined angles on the droplet formation

The results using two different nozzle sizes and four different inclined angles have been correlated in terms of dimensionless volume and dimensionless flow rate of dispersed phase and shown in Figure 5.4. This correlation was originally developed for bubble formation at vertical orifices under constant flow conditions (Clift et al., 1978).

The three dimensionless variables shown in Figure 5.4 are

- dimensionless flow rate, $Q'$:

$$Q' = (\frac{\rho}{d_0\sigma})^{\frac{3}{5}} g^{\frac{1}{5}} Q \tag{5.39}$$

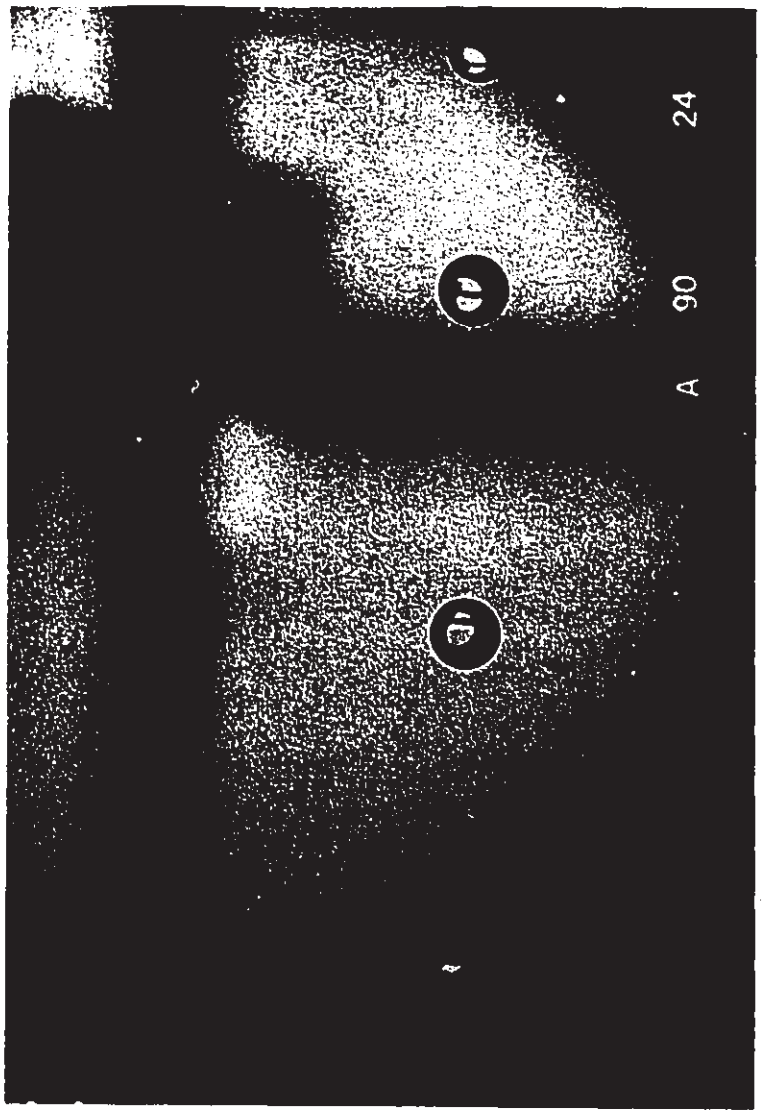


Figure 5.2: Single droplets formed in the absence of electric field

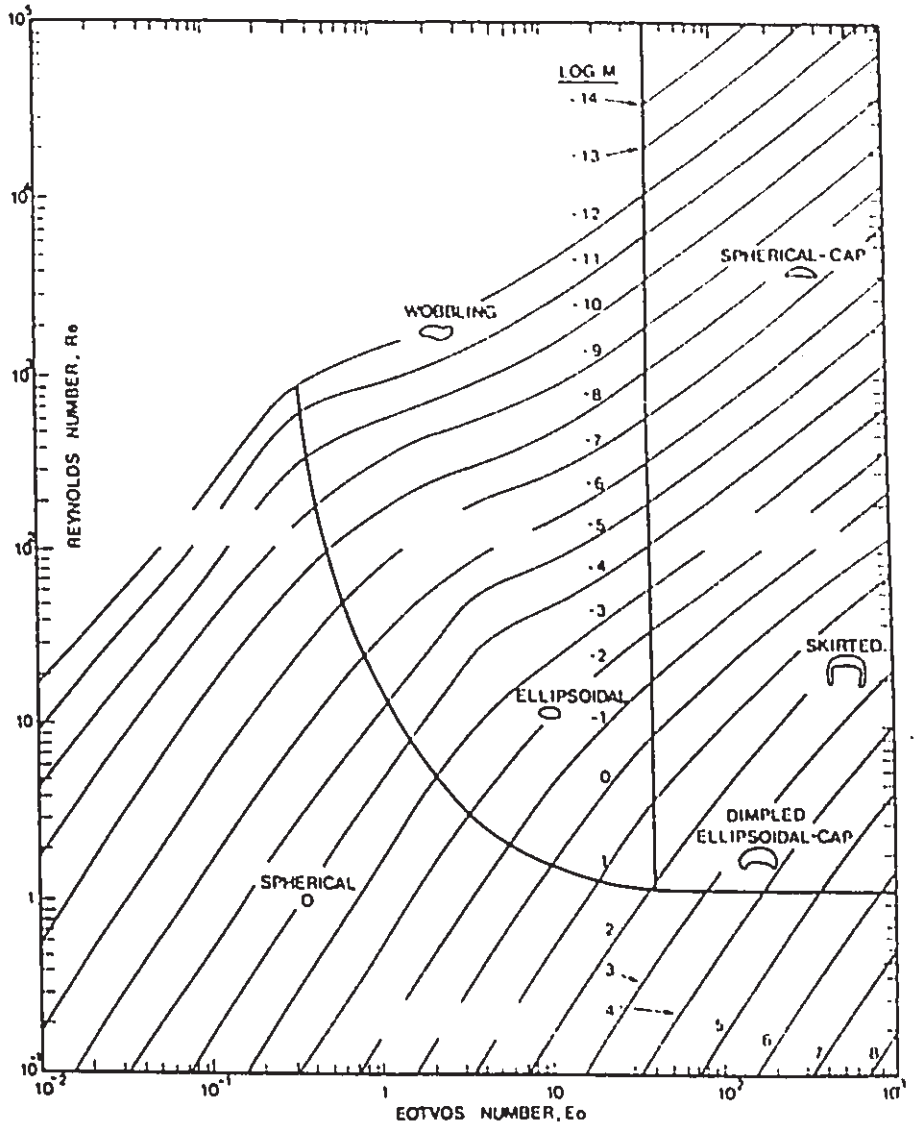


Figure 5.3: Shape regimes for bubbles and drops in unhindered gravitational motion through liquids (Clift *et al.*, 1978)

- dimensionless drop volume, $V'$:

$$V' = \frac{Vg\Delta\rho}{d_0\sigma} \tag{5.40}$$

- and dimensionless viscosity, $\mu'$:

$$\mu' = \frac{\mu_c}{(\rho d_0 \sigma)^{\frac{1}{2}}} \tag{5.41}$$

It is obvious that there is no evident effect due to nozzle size but a significant effect of inclined angles on the droplet formation. The lowest curve of Figure 5.4 indicates that there is no visible difference for two different sizes of nozzle at the minimum inclined angles of 3° (the hollow nozzle tube is almost in the horizontal position), though the droplet size increased with increasing flow rate. The other three curves in Figure 5.4 for the other inclined angles (30°, 60°, 90°) reveal that there is less effect from the flow rate on the formed droplet size at each of these fixed inclined angles. However there exists a large effect due to the inclined angle. Table 5.1 presents the relative effect for a particular droplet size between the buoyancy and the interfacial tension forces for different inclined angles of the nozzle based on Equations (5.26).

These results may be explained by the previous model assumptions of dominant interfacial tension and viscous drag during droplet formation. When the cell was inclined at 3°, there was almost no interfacial tension effect on the droplet formation. The term $\mathbf{F}_s$ in Equation (5.32) becomes relatively small. The drop sizes from two different nozzles are nearly identical as those shown in Figure 5.4 since for the cell at this position, the dominant forces are buoyancy and viscous drag. When the cell inclined angle was increased, the interfacial tension effect on the drop formation became more important and reached a maximum value at 90°. That is, the droplets would detach themselves less freely from the nozzle due to increasing effect of interfacial tension with increasing verticality, since contact length is augmented. This then would result in an increase in the droplet volume, although the flow rate does not change.

Table 5.1: Comparisons between the buoyancy and interfacial tension effect on droplet formation for a typical assumed drop diameter*

| **Inclined angles of hollow nozzle** [°] | **Interfacial tension force,** $\mathbf{F}_s$ $(10^{-5}[\mathrm{N}])$ | **Buoyancy force** $\mathbf{F}_g$ $(10^{-5}[\mathrm{N}])$ | $\mathbf{F}_s/\mathbf{F}_g$ |
|---|---|---|---|
| 3 | 0.328 | 1.72 | 0.19 |
| 30 | 3.134 | | 1.82 |
| 60 | 5.428 | | 3.16 |
| 90 | 6.268 | | 3.64 |

* Assuming droplet diameter is 3 mm; $\mathbf{F}_s$ is calculated by Equation (5.26) and $\mathbf{F}_g = \frac{\pi}{6} d^3 g \Delta\rho$.

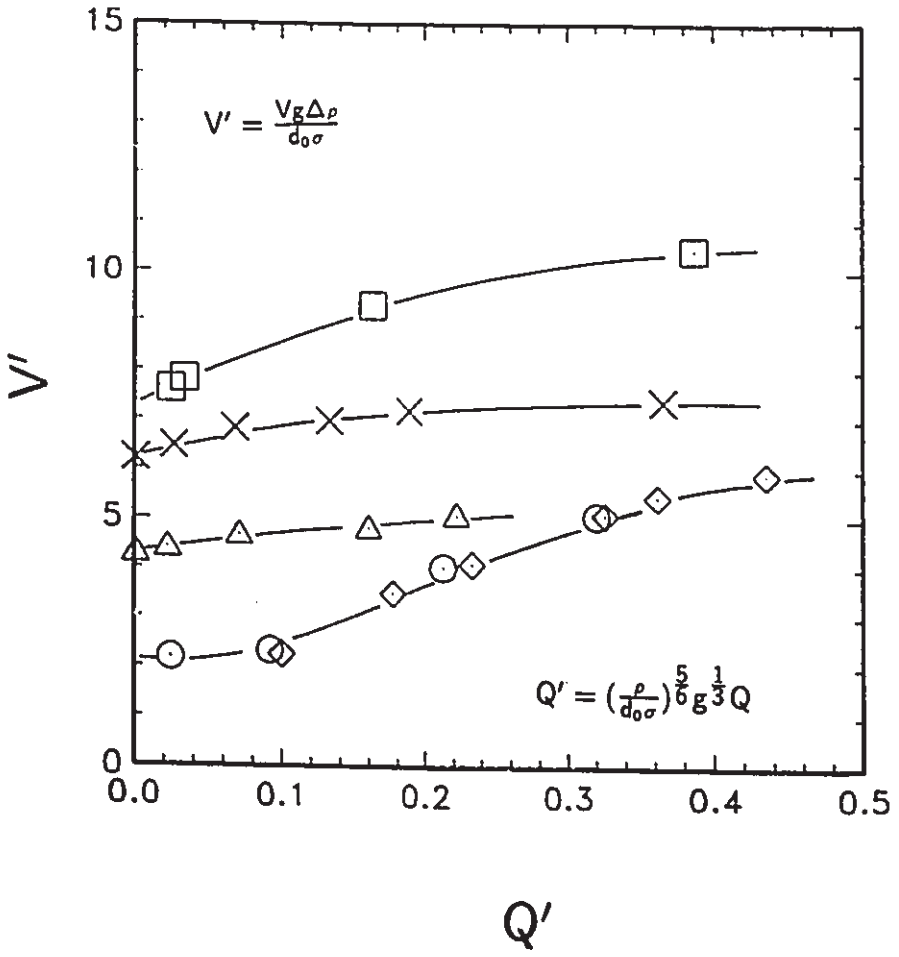


Figure 5.4: Dimensionless correlations for droplet formation

| Symbol: | ◇ | ○ | △ | × | □ |
|---|---|---|---|---|---|
| Inclination: | 3° | 3° | 30° | 60° | 90° |
| $d_0$ (mm) : | 0.56 | 0.71 | 0.71 | 0.71 | 0.71 |

### 5.4.3 Droplet size

Figure 5.5 shows drop diameter as a function of dispersed phase flow rate, for various inclination angles and nozzle diameters. Also shown are curves representing the two predictive models described above. At the shallowest inclination (3°) the two models, *i.e.* the detailed model (Equation (5.38)) and the simplified model where $d_e$ set to zero give virtually the same prediction, because in this case the contribution of surface forces is very small and $d_e$ is only 1.1 mm. Most of the results lie 5-10% higher than prediction. At steeper inclinations, the simpler model (ignoring $d_e$) predicts larger drops than the detailed model, Equation (5.38). At 30° and 60° inclination, the results favor the simpler model at low flow rates and the detailed model at high flow rates. At 90°, the simpler model is supported by the results at all flow rates. This is surprising, as the simpler model is less physically realistic than the detailed one.

The comparisons between experimental and calculated values of the droplet diameter with different nozzle sizes, various inclined angles and different flow rate are plotted as shown in Figure 5.6. The model derived for droplet formation covers all the experimental conditions with fair accuracy when experimental error is taken into account.

### 5.4.4 Drop velocity

Upon detachment, the drop quickly reaches its terminal velocity. According to the model of drop formation, the drop velocity at detachment is given by Equation (5.34); after detachment, the interfacial tension term which is relatively small in this case disappears. In the creeping flow regime ($Re_d < 1$) the terminal velocity will depend on whether the drop is circulating or not (Happel and Brenner, 1973). For a freely circulating drop with a fully mobile interface, the Hadamard-Rybezynski equation, *i.e.* Equation (5.24) applies. This is because internal circulation within the drops

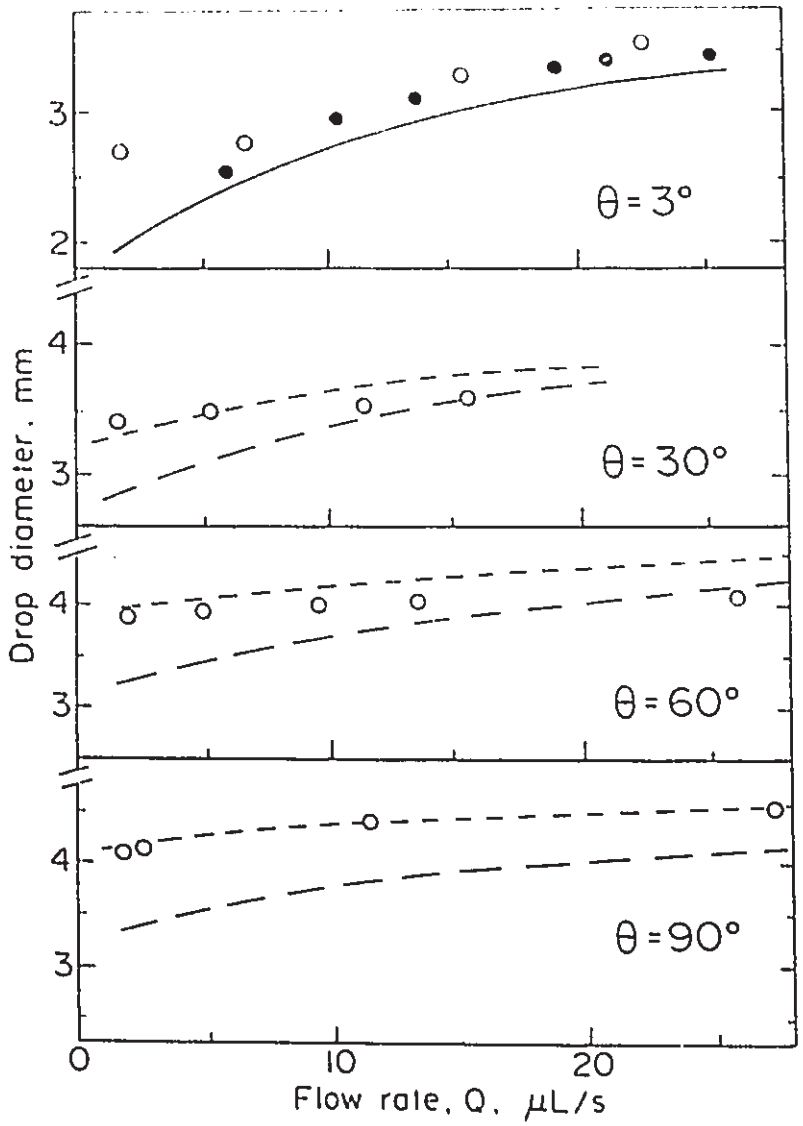


Figure 5.5: Effect of dispersed phase flow rate upon drop diameter, for different inclined angles

- • $d_0 = 0.56$mm ∘ $d_0 = 0.71$mm
- – – – Detailed model, Equation (5.38)
- · · · · Simplified model (with $d_e = 0$)
- —— Overlapping of two above predictions

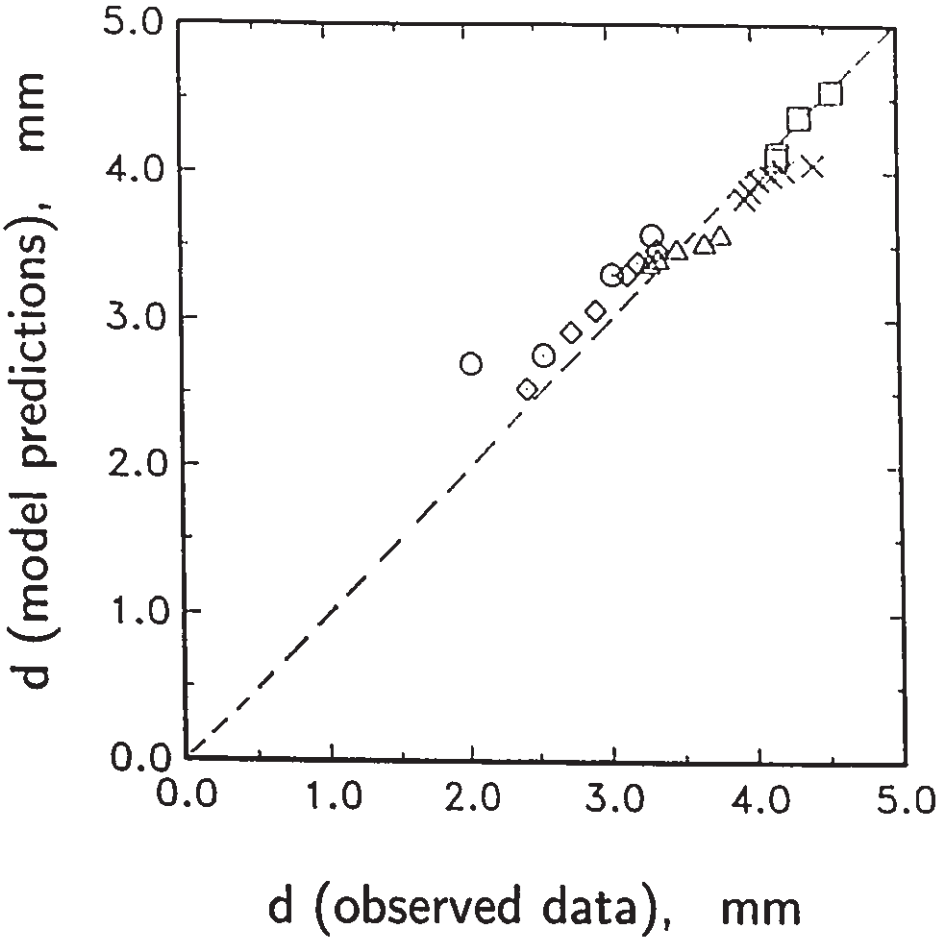


Figure 5.6: Comparisons between measured and calculated (using Equation (5.38)) droplet diameters at different inclined angles

| Symbol: | ◇ | ○ | △ | × | □ |
|---|---|---|---|---|---|
| Inclination: | 3° | 3° | 30° | 60° | 90° |
| $d_0$ (mm) : | 0.56 | 0.71 | 0.71 | 0.71 | 0.71 |

reduces the velocity gradients at the interface, and thus reduces the hydrodynamic drag. If the drop is not circulating, Stokes' law applies as assumed for the drop formation process. In this case, Equation (5.15) should be used. In both the above cases, the velocity is proportional to the square of the drop diameter; but the velocity for the circulating drop can exceed that for the rigid drop of the same diameter by as much as 50% if $\mu_d/\mu_c$ is small.

Figure 5.7 presents terminal velocity data for drops formed under different conditions. The highest Reynolds number is 0.22 which satisfies the requirement of $Re_d < 1$ for creeping flow. It is important to note that the results which agree well with Equation 5.24, *i.e.* those for the 0.56 mm nozzle at 3° inclination, were the first taken in the series of experiments. Thus they refer to a relatively pure system where the interface is likely to be mobile. The data at 90° inclination were the last taken in the series, and lie close to the rigid drop prediction. This is probably due to a build up in trace contaminants in the oil, which would lead to hindrance of surface motion (Levich, 1962).

The results at 30° and 60° inclination show an unexpectedly strong influence of drop diameter on velocity. Although the range of diameters investigated is small for these cases, it corresponds to a large range of water flow rates through the nozzle (see Figure 5.4) and it is possible that the flow rates contributed in some way to the measured velocity of the drops near the nozzle. This does not explain the existence of some velocities lower than predicted by Equation (5.15).

It is concluded that the formation and behavior of drops in the absence of electric field can be described fairly well using mechanistic models. These provide a basis for comparison with the results obtained in the presence of electric fields described in later chapters.

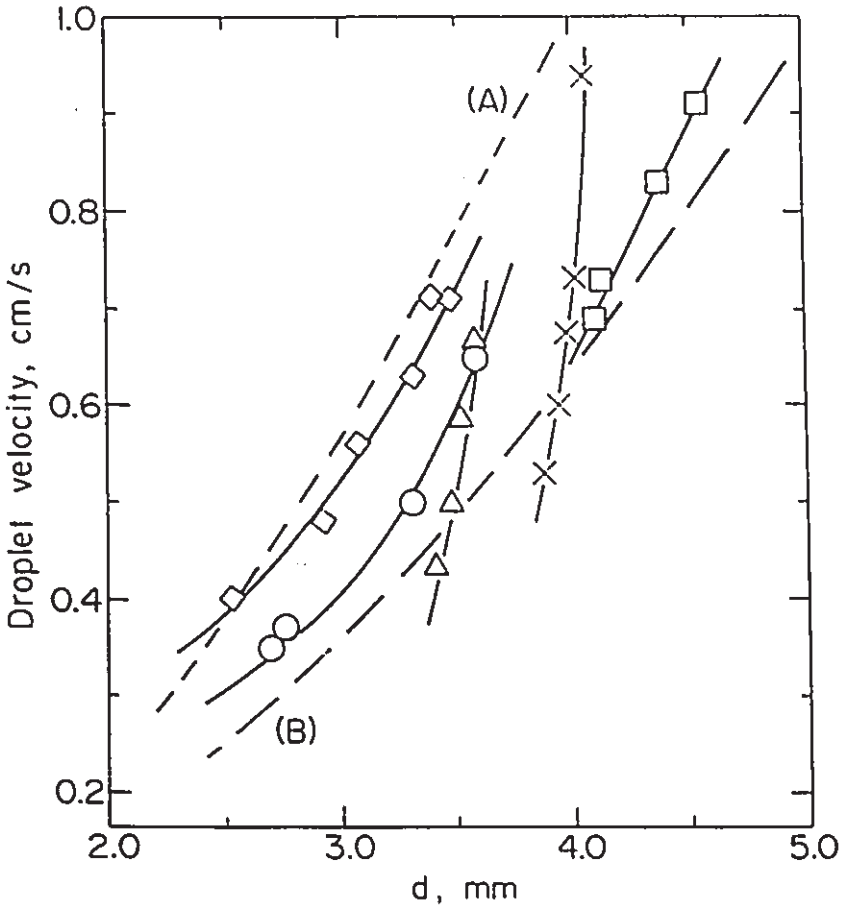


Figure 5.7: Droplet terminal velocity as a function of droplet diameter at different inclined angles

| Symbol: | ◇ | ○ | △ | × | □ |
|---|---|---|---|---|---|
| Inclination: | 3° | 3° | 30° | 60° | 90° |
| $d_0$ (mm) : | 0.56 | 0.71 | 0.71 | 0.71 | 0.71 |

(A) Hadamard-Rybczynski solution, Equation (5.24);
(B) Stokes solution, Equation (5.15)

# Chapter 6

# Droplet Formation and Dispersion in a DC Electric Field

## 6.1 Introduction

The formation and dispersion of drops in a non-uniform DC electric field provide the focus of this chapter. Section 6.2 is a qualitative description of droplet behavior observed in the electric field. The model for droplet formation is derived in section 6.3 while the droplet dispersion is described in section 6.4. Section 6.5 describes the voltage-current characteristics of the system. The electric charge acquired by the droplet during formation and its subsequent dispersion is presented in section 6.6. As a conclusion of the chapter, the mechanisms of EHD droplet formation and dispersion at different applied voltages are suggested in section 6.7.

## 6.2 Droplet Behavior in a Non-uniform DC Electric Field

Typical still photographs are shown in Figure 6.1. Figure 6.1(a) represents the applied voltages of 2 to 7 kV, featuring smaller droplets and higher detachment frequencies than those observed in the absence of electric field (described in Chapter 5). The detached drops did not move off vertically but showed alternating diverging paths. At applied voltages above 7 kV, a multi-droplet dispersion occurred in which many small droplets moved off from the hollow electrode at high velocities, then decelerated a few cm away from the hollow electrode where the field strength was lower. The result, shown in Figure 6.1(b), was a fine dispersion of drops which were slow to settle.

## 6.3 Droplet Formation by Hollow Electrode with Applied Electric Field

### 6.3.1 Droplet formation model

The effects of electric force on drop formation have usually been represented by an equilibrium balance of forces acting upon the drop at the moment of detachment (Stewart and Thornton, 1967; Ogata *et al.*, 1976; Takamatsu *et al.*, 1981; Carleson and Berg, 1983; Vu and Carleson, 1986):

$$\mathbf{F}_g + \mathbf{F}_e = \mathbf{F}_s \tag{6.1}$$

The terms $\mathbf{F}_g$ and $\mathbf{F}_s$ correspond to those given in Equation (5.28).

The electrical force $\mathbf{F}_e$ is a complex function of the charge trapped within the drop, drop shape, and the local field strength near the hollow electrode, which is determined by the equipment geometry. Table 6.1 summarizes expressions suggested

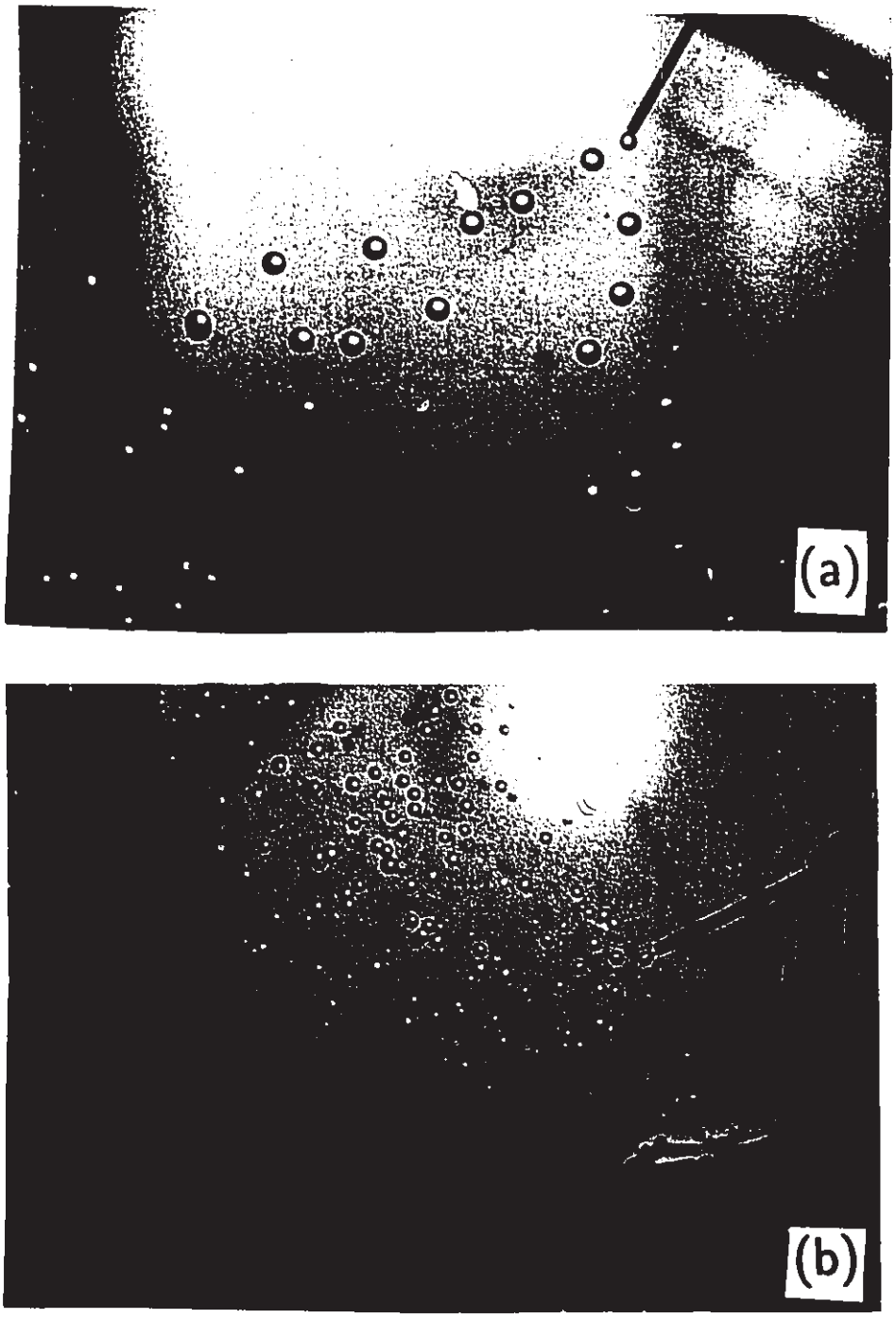


Figure 6.1: Typical photographs of droplet in the non-uniform electric field:

(a) applied voltage 2 to 7 kV; (b) applied voltage > 7 kV

Table 6.1: Previous work on electric force ($F_e$) acting upon a detaching drop

| Source | Experimental Conditions | Expression for $F_e$ |
|---|---|---|
| Ogata et al. (1976) | Water or ethanol/water drops formed in air at nozzle with positive voltage. (non-uniform field) | $2\pi \epsilon_o V^2/\ln(8L/d_o)$ |
| Takamatsu et al. (1981) | Water or furfural drops formed at nozzle with positive voltage, 5 cm from grounded electrode. | $4\pi\epsilon \beta r^2 E_o^2$ |
| Carleson & Berg (1983) | Water drops formed in gas phase with $SO_2$ absorption. Field strength up to 8 kV/cm | $nd^2$ CqE |
| Takamatsu et al. (1983) | Water drops formed at nozzle in atmosphere and insulating liquids. (non-uniform field) | $4\pi\epsilon(0.0634)(1 + r/2L)^2 V^2$ |
| Byers and Perona (1988) | Water drops formed in cyclohexane at horiz. orifice plate. (non-uniform field) | $9.8\times 10^{-5}(V/1000)^2 \nu^{0.54}$ |
| Vu and Carleson (1986) | Glass column, 0.45 m height Cont.phase; pentane, hexane | $\epsilon A E^2$ |

in the literature for the electric force acting on the detaching drop. As can be seen, there are considerable variations between the proposed expressions. Field strength E can be included as a variable only when it is made uniform by adding a guard plate around the nozzle or orifice at which drops are formed. For non-uniform fields, the applied voltage $V$ must be used in place of field strength; the electric force is generally found proportional to the square of voltage, with a constant included to take account of the geometry of the cell used. The effect of drop diameter (or radius) on electric force in the expressions in Table 6.1 varies. In this work the geometry of the hollow electrode as well as planar electrodes is not simple, so a square law dependence is assumed based on EHD forces described in Chapter 2. This is consistent with three of the equations in Table 6.1. The empirical equation of Byers and Perona (1988) implies a 1.62 power dependence of force on drop diameter which comes quite close to square law dependence.

Thus the following expression for electrical force is used in the present model:

$$\mathbf{F}_e = kd^2V^2 \tag{6.2}$$

This force is assumed to act in the axial direction, *i.e.* at angle $(90 - \theta)^\circ$ to the vertical.

Gravity force acts vertically downwards on the drop, so that the resultant force $\mathbf{F}_{eg}$ of gravity and electrical forces is inclined at an angle $\theta'$ as shown in Figure 6.2. The balances of forces in the vertical and horizontal directions are respectively given by:

$$\mathbf{F}_{eg}\sin\theta' = \mathbf{F}_g + \mathbf{F}_e\sin\theta \tag{6.3}$$

$$\mathbf{F}_{eg}\cos\theta' = \mathbf{F}_e\cos\theta \tag{6.4}$$

where

$$\theta' = \arctan\left(\frac{\mathbf{F}_g}{\mathbf{F}_e\cos\theta} + \tan\theta\right) \tag{6.5}$$

The dynamic balance of forces in the direction of motion of the drop centre can now

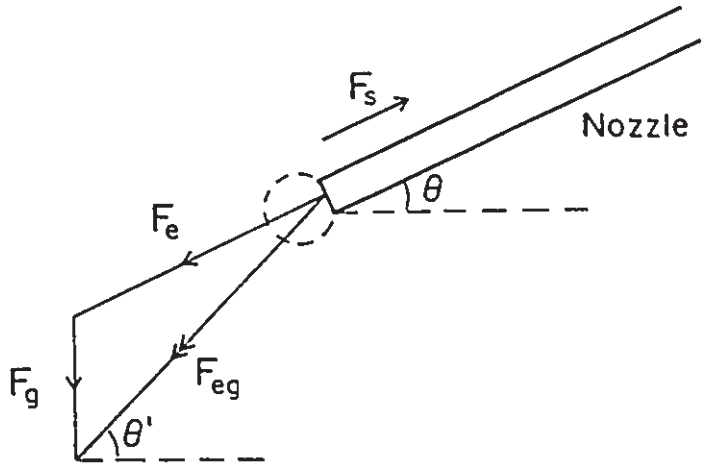


Figure 6.2: Schematic diagram showing directions of forces acting upon growing drop in the presence of electric field

be written, analogous to Equation (5.32), as

$$\mathbf{F}_{eg} - \pi d_o \sigma \cos(\theta' - \theta) = \mathbf{F}_d \tag{6.6}$$

or in expanded form,

$$[\frac{(\pi d^3 g \Delta\rho/6) + (kd^2 V^2 \sin\theta)}{\sin\theta'}] - [\pi d_o \sigma \cos(\theta' - \theta)] = 3\pi d\mu(\frac{dS}{dt}) \tag{6.7}$$

Although drops may circulate in the presence of an electrical field (Taylor, 1966; Chang and Berg, 1985), the Stokes Law drag expression is retained here. Hence an equation analogous to Equation (5.34) is obtained:

$$\frac{dS}{dt} = [\frac{(d^2 g \Delta\rho/18) + (kd^2 V^2 \sin\theta/3\pi)}{\mu \sin\theta'}] - [\frac{\pi d_o \sigma \cos(\theta' - \theta)}{3d\mu}] \tag{6.8}$$

The time variable is transformed to drop diameter using the same method as in obtaining Equation (5.36):

$$\frac{dS}{dd} = [\frac{(\pi g d^4 \Delta\rho/36) + (kd^3 V^2 \sin\theta/6)}{Q\mu \sin\theta'}] - [\frac{\pi d_o \sigma d \cos(\theta' - \theta)}{6Q\mu}] \tag{6.9}$$

This equation can be integrated numerically until the distance of movement $S$ corresponds to

$$S = \frac{d + d_o sin(\theta' - \theta)}{2} \tag{6.10}$$

The integration has been carried out assuming that $d_e = 0$, *i.e.* that drop motion can initially occur towards the tip of the hollow electrode. As discussed in Chapter 5, this simplified model gave good agreement with the results in the absence of electric field.

At very high applied voltages, the buoyancy forces and the interfacial forces are negligible compared to the electric and drag forces. So Equation (6.9) can be simplified to the form

$$\frac{dS}{dd} = \frac{kd^3 V^2}{6Q\mu} \tag{6.11}$$

This can be integrated subject to the boundary condition $S = 0$ when $d = 0$ to give

$$S = \frac{kd^4 V^2}{24Q\mu} \tag{6.12}$$

At detachment, $S$ is equal to $d/2$ so that the diameter of the formed drop is given by

$$d = (\frac{12Q\mu}{kV^2})^{1/3} \tag{6.13}$$

Thus in the limiting case of negligible gravity and surface effects, the drop diameter is expected to vary as the $-2/3$ power of the applied voltage.

### 6.3.2 Effect of inclination angles on droplet formation

Figure 6.3 shows the effect of applied voltage and inclination angle upon measured drop size, compared with values predicted from the integration of Equation (6.9). The value of $k$ was obtained by fitting to the data at high voltages. It is seen that the model curves follow the data points quite well at high voltages, but the agreement in the range 0 to 2 kV is less satisfactory. At 3° and 30° inclination, the model predicts maxima in the drop size/voltage plot. At high voltages, $d \propto V^{-2/3}$ as suggested by Equation (6.13) and this supports the assumptions made in Equation (6.2) about the nature of the electric force.

### 6.3.3 Effect of dispersed phase flow rate on droplet formation

Figure 6.4 shows the effect of water flow rate upon the diameter/voltage plots at 3° inclination. As in Figure 6.3, the model predicts maxima in the drop size plot in the region of 1 kV applied voltage. Maxima were observed but they are much shallower than predicted. Fitting of the data with respect to $k$ was done on the basis of the higher voltage results and it was found that a single value of $k$ did not give a satisfactory fit at all flow rates; it was necessary to apply a different value of $k$ at each flow rate, as shown in the caption of Figure 6.4. The effect of flow rate upon $k$ corresponds to the relationship

$$k \propto Q^{-0.57} \tag{6.14}$$

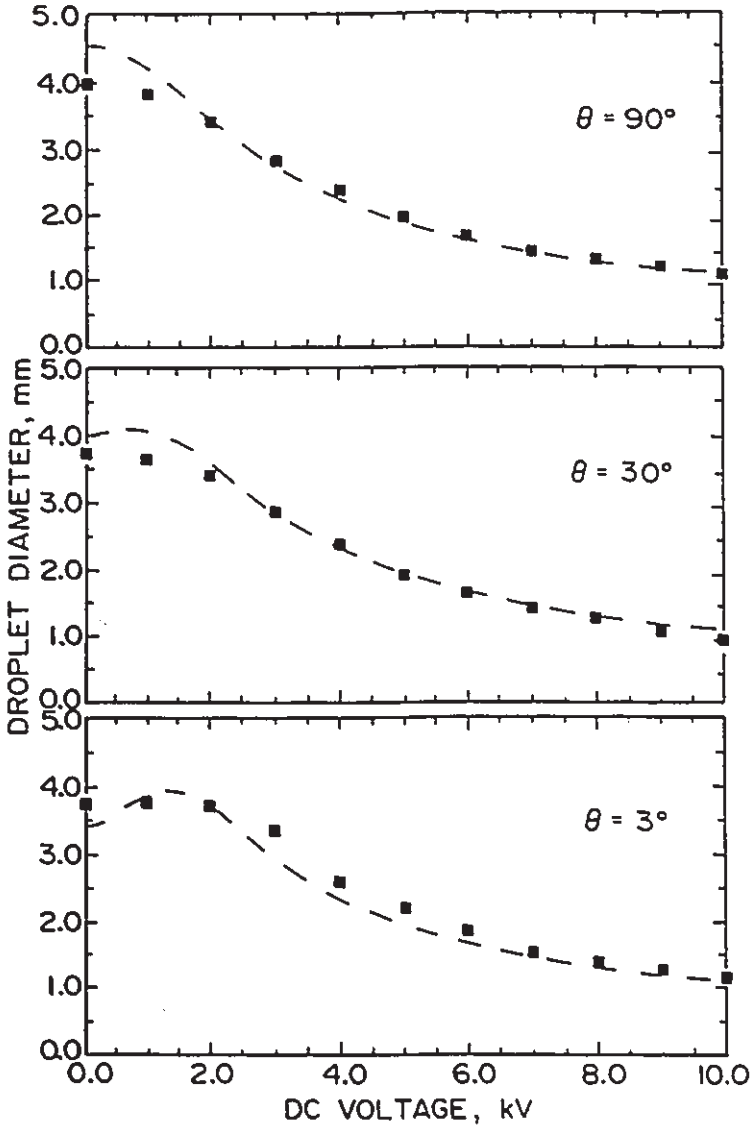


Figure 6.3: Effect of applied voltage and inclined angle upon drop diameter

□ — Observed data at 26.0 $\mu$L/s
- - - - Model predictions ($k = 0.66$ N/m$^2 \cdot$ kV$^2$)

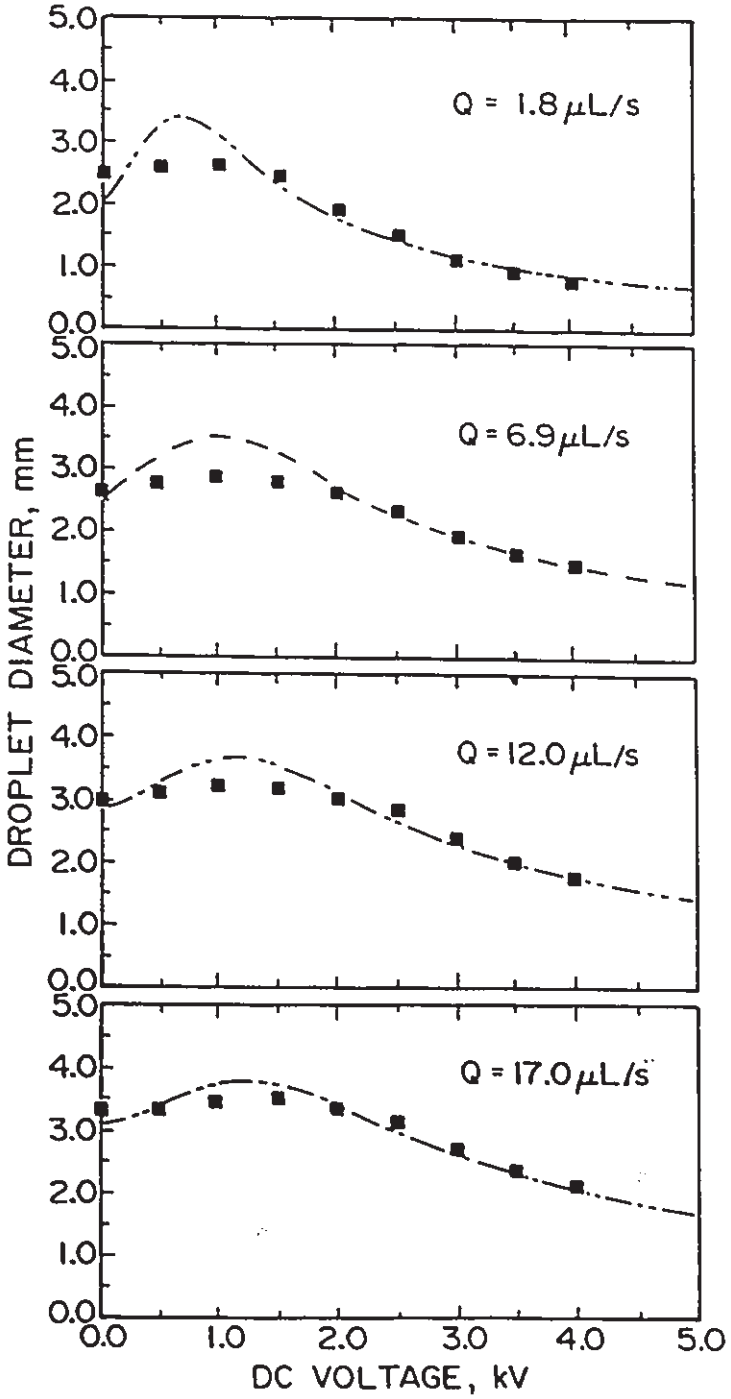


Figure 6.4: Effect of applied voltage upon diameter at inclination angle 3°, model curves are fitted as dashed lines for the following value of $k$:

| $Q$ (μL/s): | 1.8 | 6.9 | 12.0 | 17.0 | 26.0* |
|---|---|---|---|---|---|
| $k$ (N/m$^2$ · kV$^2$): | 3.0 | 1.32 | 1.00 | 0.80 | 0.66 |

*see lower section of Figure 6.3

This means that the flow rate of dispersed phase will influence the EHD force generated through the $k$ values as expressed in Equation (6.14) due to the coupling between electric field and velocity field. This effect can also be derived from fundamental EHD equations described in Chapter 2 with following assumptions.

- The droplet forming from hollow electrode is considered as a single-phase process. Therefore, the second and third term of Equation (2.12) are ignored because of the uniform dielectric constant as well as the incompressible feature of the liquid, *i.e.*

$$\mathbf{f}_e = \rho_{ei}\mathbf{E}_d \tag{6.15}$$

- The electric current is mainly due to convection of charge by the velocity field of the dispersed phase. Then, the effect of charge diffusion and charge mobility on current is considered negligibly small. Therefore, the second and third term of Equation (2.8) are also ignored, *i.e.*

$$\mathbf{J} = \rho_{ei}\mathbf{U} \tag{6.16}$$

Hence from Equations (6.15) and (6.16), we can obtain

$$\mathbf{f}_e = \rho_{ei}\mathbf{E}_d = \frac{\mathbf{J}\mathbf{E}_d}{\mathbf{U}} \tag{6.17}$$

In the situation of a growing drop as shown in Figure 6.1, it is assumed that $\mathbf{f}_e$ is proportional to $\mathbf{F}_e/d^2$, the current per unit area is also proportional to $V/d^2$, and the electric field strength $\mathbf{E}$ is proportional to $V/L$, where $L$ is a linear dimension of the apparatus. The Velocity $\mathbf{U}$ is proportional to $Q/d^2$. When these proportionalities are substituted in Equation (6.17) the following expression can be derived.

$$\mathbf{F}_e \propto \frac{V^2 d^2}{QL} \tag{6.18}$$

This indicates that the force $\mathbf{F}_e$ would vary inversely with the flow rate of dispersed phase, as well as having a square-law dependence on drop diameter (as confirmed).

The above derivation is approximate, but it does confirm the trend observed whereby $k$ decreases with flow rate, although the observed power-law exponent of $-0.57$ differ somewhat from the predicted exponent of $-1.0$.

## 6.4 Droplet Dispersion in the Electric Field

The video images show that the drops detach rapidly from the nozzle and then decelerate over a distance of several cm, indicating that they are moving to a region of lower field strength. It was not possible to obtain detailed velocity histories, but the average velocities $\mathbf{U}_{tip}$ over 1–3 cm were obtainable from the video images through frame by frame analysis. Figure 6.5 shows that $\mathbf{U}_{tip}$ increases sharply with applied voltage, despite the decrease in drop size. A surprisingly good correlation of the results is obtained by a double logarithmic plot of velocity against the corresponding drop diameter, as shown in Figure 6.6. It appears that velocity varies as the inverse square of drop diameter. The limiting case of zero applied voltage (gravitational effects only) is represented by the Hadamard-Rybczinski and Stokes expressions, Equations (5.15) and (5.24), with velocity proportional to the square of diameter. Equation (5.24) approaches the data at 4 mm diameter which is the approximate drop size in the absence of electric field effects.

The inverse square correlation between velocity and diameter can be derived subject to several assumptions. First, a steady state is assumed, with the electric force on the moving drop assumed to be given by Equation (6.2) and the balancing drag force expressed by Stokes' law.

$$\mathbf{F}_e = kV^2d^2 = 3\pi\mu d\mathbf{U}_{tip} \tag{6.19}$$

The drag force may be overestimated by Stokes' law since the drops follow each other in a closely spaced succession (Figure 6.1) and because of electrical effects. The final assumption is that drop size is the simple function of applied voltage given in

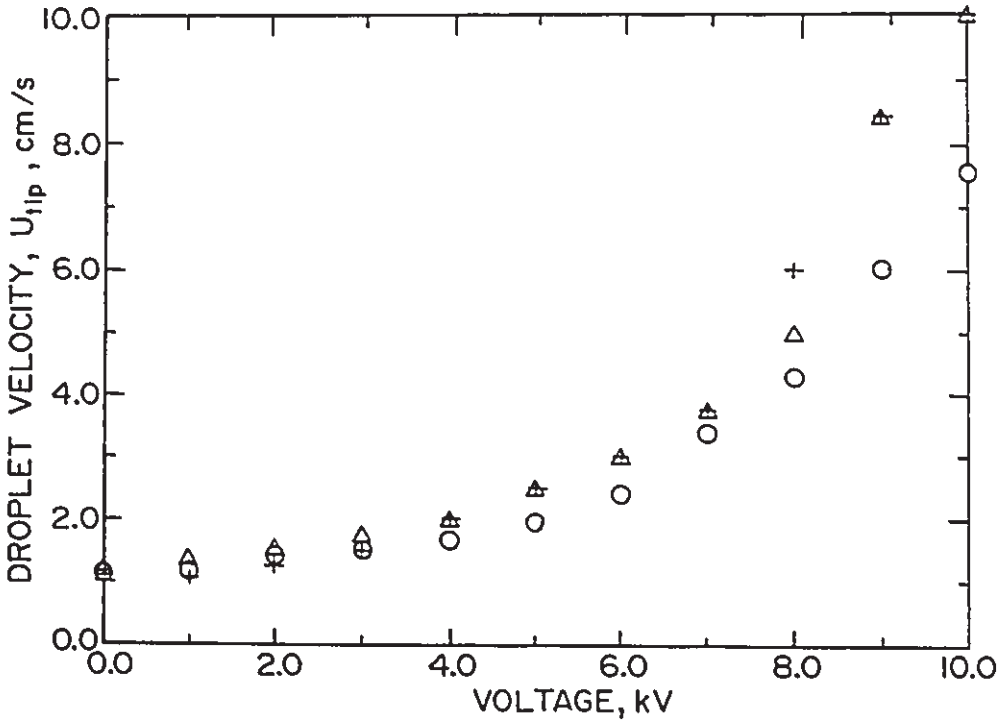


Figure 6.5: Effect of applied voltage on average droplet velocity

$Q = 26.0$ $\mu$L/s and $d_0 = 0.71$ mm

| Inclination: | 3.0° | 30° | 90° |
|---|---|---|---|
| Symbol: | ○ | △ | + |

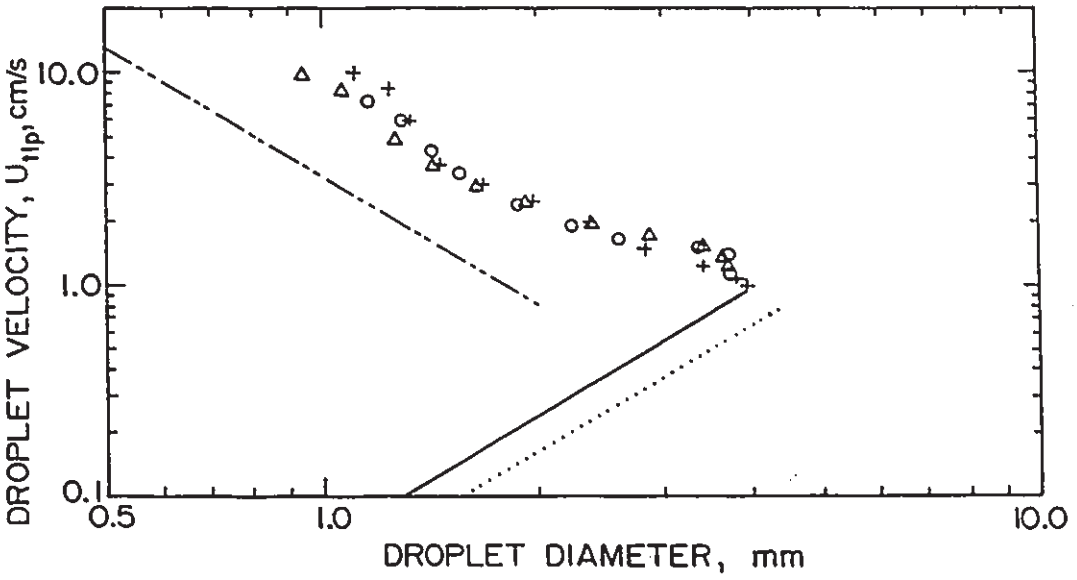


Figure 6.6: Relation between average drop velocity and drop diameter

$Q = 26.0$ $\mu$L/s and $d_0 = 0.71$ mm

| Inclination: | 3.0° | 30° | 90° |
|---|---|---|---|
| Symbol: | ○ | △ | + |

——— Hadamard-Rybczinski Equation, Equation (5.24)
····· Stokes Equation, Equation (5.15)
- - - - - - Equation (6.20)

Equation (6.13). With these simplifying assumptions, the $kV^2$ term and the viscosity can be eliminated between Equations (6.13) and (6.15) to give the result

$$U_{tip} = \frac{4Q}{\pi d^2} \tag{6.20}$$

This simplified derivation has been plotted on Figure 6.6 and it is seen to run parallel to but below the band of data points by a factor of about 2.5. One factor in this difference is the wake effect of the drops following each other closely, whereby the drag is reduced below the value expected from Stokes' law (Happel and Brenner, 1965). However, this effect is only in the order of 10% at the drop separations observed in this work. A more likely reason for the discrepancy is an increase in electrical force due to the repulsion between drops and hollow electrode tip which would be greatest just after the charged drop detaches from the hollow electrode tip. This is consistent with the observed rapid acceleration of the drops just after detachment.

## 6.5 Current-Voltage Characteristics of the System

### 6.5.1 Effect of two different electrode connection modes

As has been described in Chapter 3, two different electrode connection modes were used in this work mainly to compare the differences in the time-averaged current-voltage (I-V) characteristics from which the efficiency of the energy input can be determined. The two connection modes have shown significant difference in the time-averaged I-V characteristics at zero drop phase flow rate.

The effect of two connection modes on the I-V characteristics can be clearly shown in Figure 6.7, where the currents are expressed as the absolute values. As seen in the figure, the current measured at hollow electrode is much higher when the hollow

electrode was connected to the DC power supply than when it was connected to the ground because of the significant differences in electric field distribution. According to the numerical results of electric field modelling (reported in Chapter 4), the electric field intensity near the hollow electrode is much higher when it is applied by the high voltage connection boundary conditions than when it is applied by the ground connection boundary conditions. This corresponds to the electric current measured at hollow electrode as shown in Figure 6.7.

Since there were no visible effects of the two connection modes on the droplet formation and dispersion from experimental observations in this work using mineral oil of low electrical conductivity as continuous phase, the I-V characteristics of the present system as seen in Figure 6.7 indicates that the major current flow path from hollow electrode may be caused by surface leak current at the wall of LUCITE cell when the hollow electrode was connected to the power supply. As has been described in Chapter 3, the hollow electrode is made of stainless steel which is immersed and directly exposed in the continuous phase of low conductivity mineral oil. There is a connection leads to the hollow electrode through the top end plate. On the other hand, the planar electrode is made of copper wire-strips which are well insulated by a layer of ceramic coating material. Therefore, most of the current would flow to the ground from power supply through the connections along the surface of equipment cell if the power supply is directly connected to the hollow electrode. Such surface conductance effect can not exist if the power supply is connected to the planar electrodes due to the structure and geometry differences of the electrodes. Thus the current measured in this connection mode is significantly reduced with the difference of 4–5 orders of magnitude lower compared with the other connection mode. The surface conductance phenomena has also been reported in the other EHD type equipment (Chang, *et. al.*, 1990).

The results indicate that it is more energy efficient to make the connection of hollow electrode to the ground while make the connection of planar electrodes to the

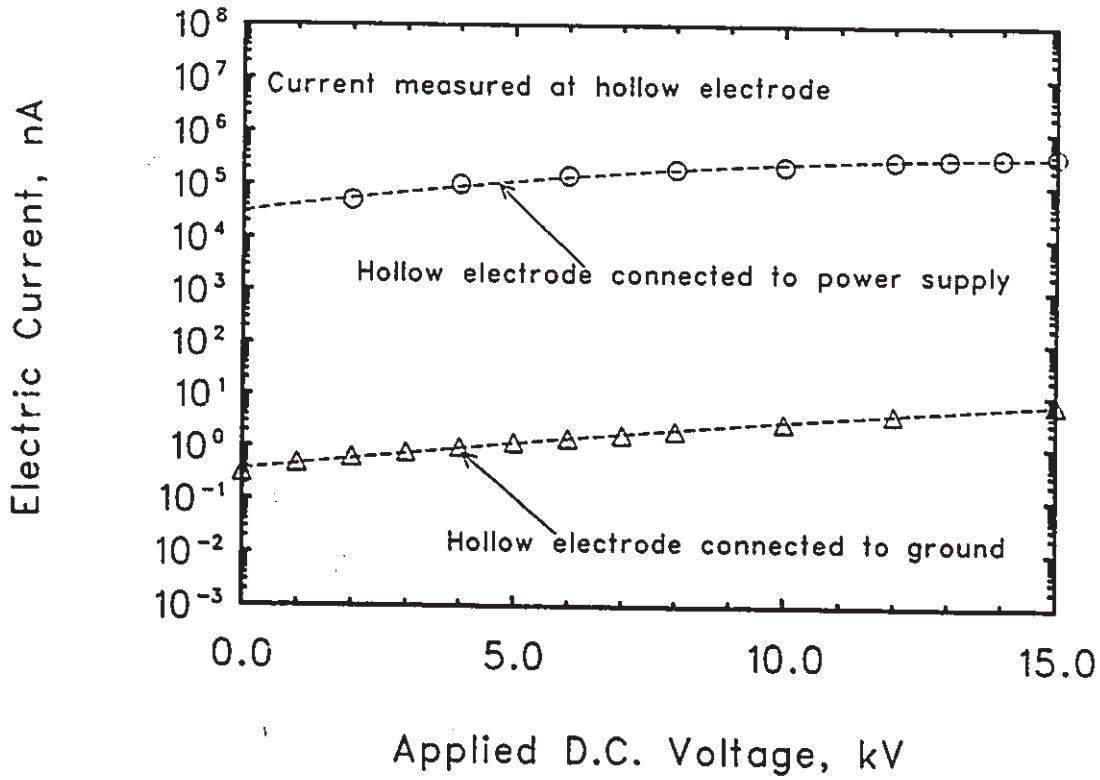


Figure 6.7: Effect of electrode connection modes on I-V characteristics (background current with $Q = 0$)

high voltage power supply.

### 6.5.2 Effect of the conductivity of continuous phase

The background current, *i.e.* current at zero drop phase flow rate, was measured from the experimental cell filled with either pure unused mineral oil or filled with used recirculating oil which had been saturated with small amount of distilled water and possibly had been contaminated as well. The electric conductivities of these two different kinds of continuous phase have been given in Table 3.3.

The effect of the conductivity of continuous phase on I-V characteristics is shown in Figure 6.8. As illustrated in Figure 6.8(a),(b), the effect of the conductivity of continuous phase on I-V characteristics is also significant except for the current measured at the hollow electrode with the second connection mode, *i.e.* it is connected to the power supply. This is the case that the current may be consisted with the leak current due to surface conduction as postulated in the previous section, therefore the background current measured mainly depends on the field strength not the conductivity of continuous phase. Thus the results shown in Figure 6.8(a) also support the surface conduction phenomena as described before.

In all other cases, the current measured from the continuous phase of pure mineral oil were all lower than those measured from the continuous phase of reused mineral oil saturated with water and contaminated with other impurities due to the difference of the conductivities. As has been known that the recirculation of the mineral oil in the present work would cause contamination by dissolved water and dusts which may contain some free ions and therefore, gives relatively higher conductivity (Kitahara, 1984).

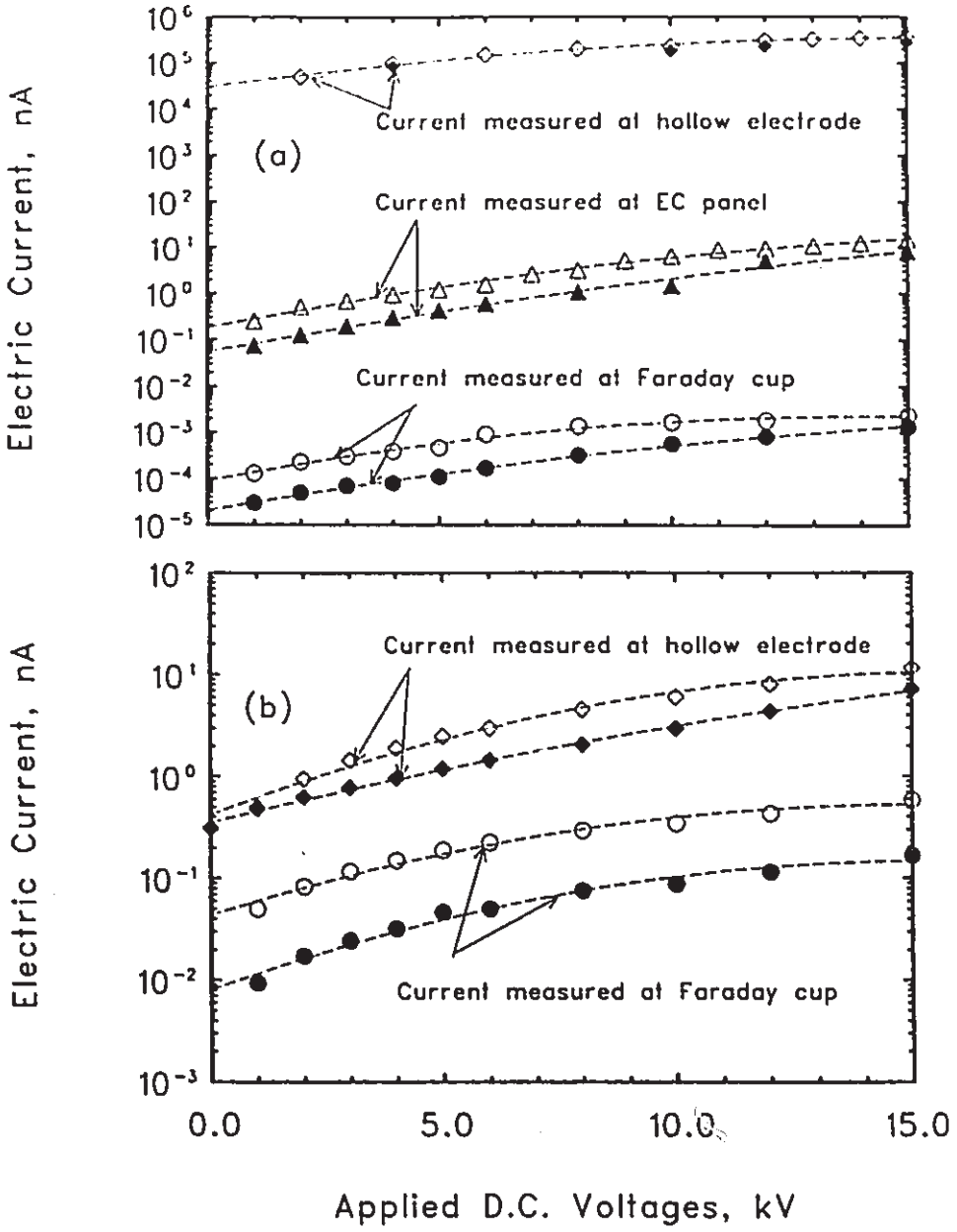


Figure 6.8: Effect of the conductivity of continuous phase on I-V characteristics (background current with $Q = 0$)

Hollow electrode connected to: (a) power supply; (b) ground

* Open symbols: Oil saturated with water; Closed symbols: Pure oil

### 6.5.3 Effect of the drop phase flow rate

Figure 6.9 shows the typical current waveforms when droplets formed continuously from hollow electrode which was electrically connected to the ground. As seen in Figure 6.9, the current increases with the droplet growing and decreases to the minimum values upon the droplet detachment from hollow electrode, due to the charge accumulation on the growing droplet. Therefore, the wave forms shown in Figure 6.9 give exactly the same droplet forming frequency as measured by other means (*e.g.* stroboscope).

The effect of drop phase flow rate on I-V characteristics is shown in Figure 6.10 for the case of hollow electrode connected to ground. The results shown in Figure 6.10 are the net current values for two different drop phase flow rates after background current correction, *i.e.* the current measured at zero flow rate is subtracted, while the background current is also shown in the figure for comparison. As seen in Figure 6.10, the non-linear feature of I-V characteristics suggests that the enhanced current flow with the droplet phase flow rate is due to unipolar charge injection as well as charge induction at very high applied voltages. It is noted also that a larger flow rate through the hollow electrode carries more current as shown in Figure 6.10. This is consistent with Equation (2.8) or the simplified form, Equation (6.16) where the charge mobility and the charge diffusion effects were assumed negligible.

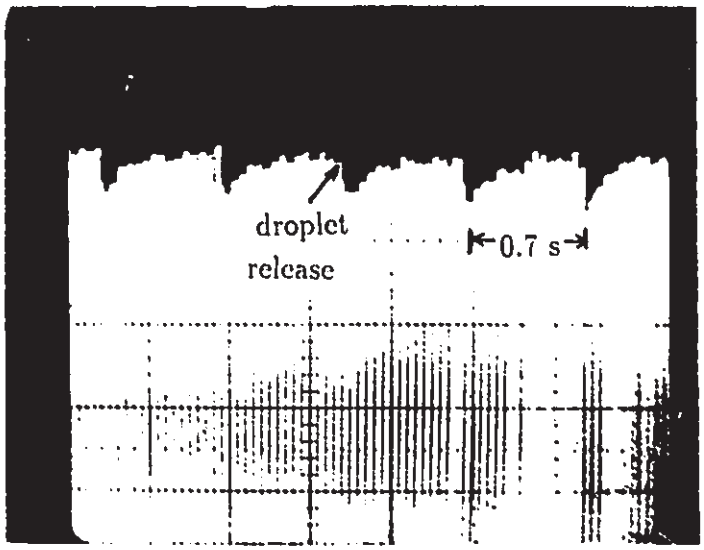


Figure 6.9: Effect of drop phase flow on current waveforms at hollow electrode (hollow electrode connected to ground)

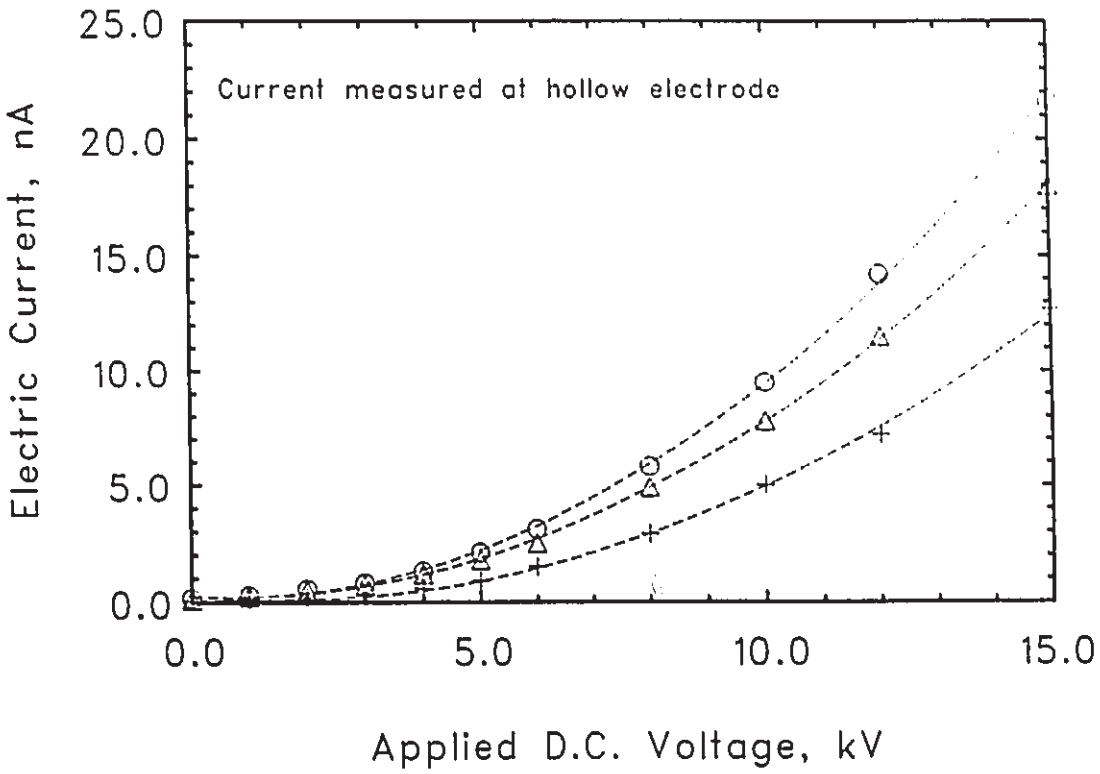


Figure 6.10: Effect of drop phase flow rate on I-V characteristics at hollow electrode (hollow electrode connected to ground)

| $Q$ ($\mu$L/s) : | 0 | 8.45 | 20.0 |
|---|---|---|---|
| Symbol: | + | △ | ○ |

## 6.6 Charge Acquired during EHD Droplet Formation

### 6.6.1 Induced maximum charge by electric field on detached drops

When a droplet is forming from the hollow electrode in an applied electric field, a net electric charge acquired on a dielectric liquid may reside at the interface of the drop and exerts an outward electric force which opposes the interfacial tension. Several different mechanisms for charge acquisition may apply in this case. If sufficient charge is acquired by the forming drop to overcome the interfacial tension, it will detach from the hollow electrode. Therefore the droplet total charge acquired during the formation period will influence the detached droplet size.

There do not appear to be many publications on droplet charge in liquid-liquid two-phase systems and most of the literature related to droplet charge only considers gas-liquid systems. The Rayleigh instability model, for example, is still very popular for the maximum charge limit evaluation on the droplet in gas-liquid systems although it has been derived for more than a century (Rayleigh, 1882).

Figure 6.11 shows the average volume charge density acquired on the forming droplets at the hollow electrode as a function of applied DC voltages. The charge acquired on the droplets can be determined via the access current measurement at hollow electrode as described in Chapter 3. As seen in the figure, the electric field induced volume charge density on the droplet is increased with the increasing of applied voltages; and charge acquired on the droplet is larger with the smaller drop phase flow rate.

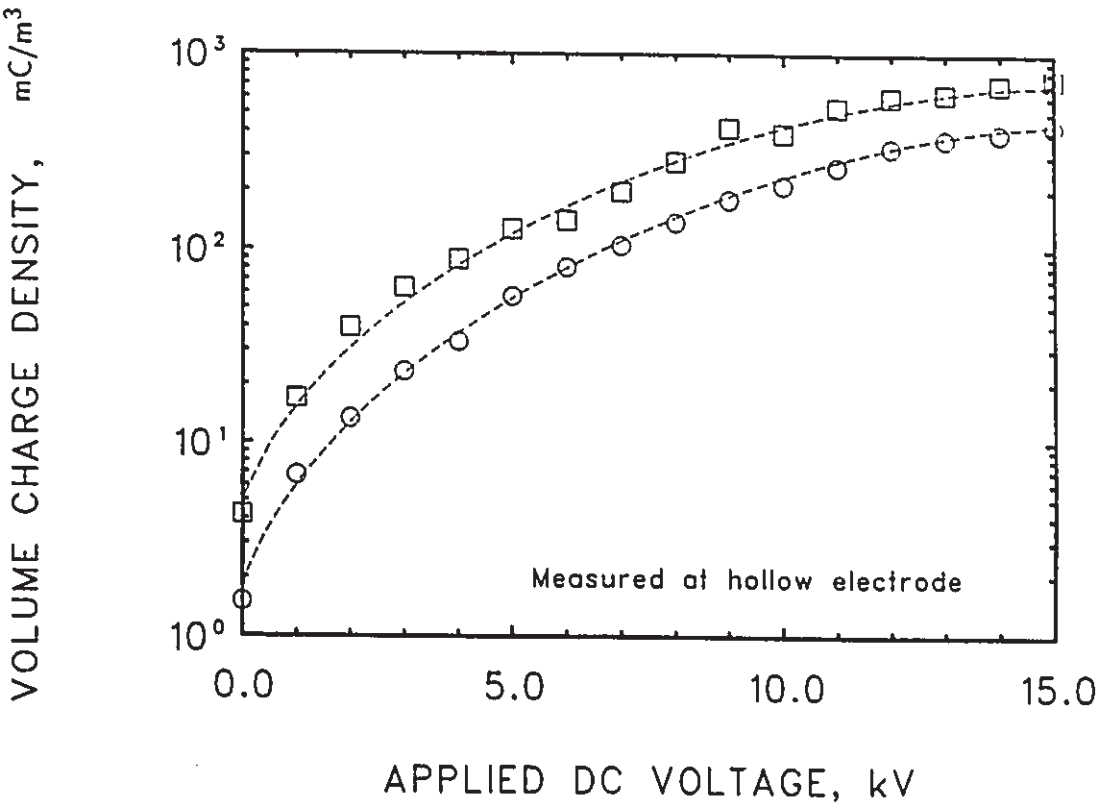


Figure 6.11: Charge acquired by droplet as a function of applied DC voltage (Hollow electrode connected to ground)

□ — 7.1 $\mu$L/s; ○ — 21.0 $\mu$L/s

### 6.6.2 Correlations and comparisons of charge acquired on detached droplet

The maximum charge acquired during the droplet formation in the present work may be correlated by the modified Rayleigh instability model, or modified Vonnegut & Neubauer model, which is similar to the modified Rayleigh instability model with the only difference in a constant by factor of 1/2, as has been described in Chapter 2. These modified correlation models are not only useful as a criterion to correlate and check the consistency of the experimental results but also useful to investigate the mechanisms of EHD droplet formation and dispersion. The different forms of the modified Rayleigh instability model are listed bellow:

- expressed as the total charge on droplet in terms of droplet diameter,

$$q = (8\pi^2 \epsilon_{eff} \sigma d^3)^{1/2} = \{8\pi^2 [\frac{3\epsilon_c(\epsilon_d - \epsilon_c)}{2\epsilon_c + \epsilon_d}] \sigma d^3\}^{1/2} \tag{6.21}$$

- expressed as the volume charge density in terms of the droplet volume,

$$\frac{q}{V_d} = (\frac{48\pi\epsilon_{eff}\sigma}{V_d})^{1/2} = \{\frac{48\pi\sigma}{V_d} \cdot [\frac{3\epsilon_c(\epsilon_d - \epsilon_c)}{2\epsilon_c + \epsilon_d}]\}^{1/2} \tag{6.22}$$

  where $V_d$ is the droplet volume.

- or expressed as droplet charge-to-mass ratio which is quite often used in gas-liquid systems:

$$\frac{q}{m_d} = \frac{12}{\rho_d}(\frac{2\epsilon_{eff}\sigma}{d^3})^{1/2} = \frac{12}{\rho_d}\{\frac{\sigma}{d^3}[\frac{6\epsilon_c(\epsilon_d - \epsilon_c)}{2\epsilon_c + \epsilon_d}]\}^{1/2} \tag{6.23}$$

  where $\rho_d$ is the density of the drop phase and $m_d$ is the mass of one droplet.

Figure 6.12 shows the absolute values of droplet charge measured both at the hollow electrode and the Faraday cup, with two different electrode connection modes. For the hollow electrode connected to ground, droplet charge was measured at both

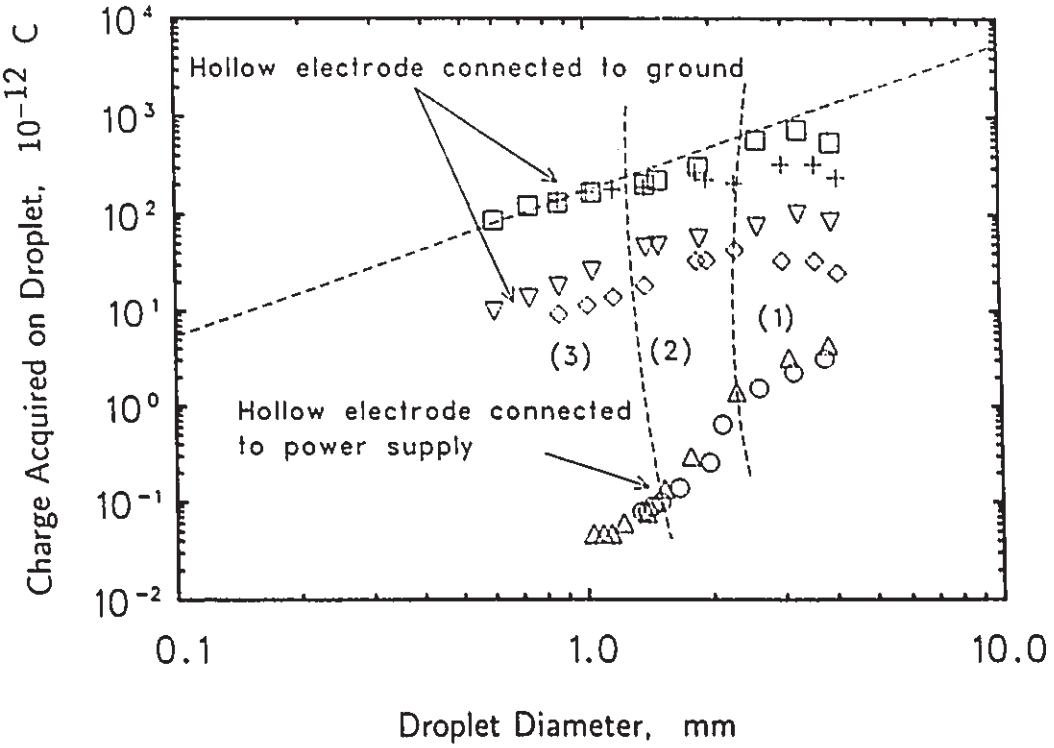


Figure 6.12: Total charge on the droplet as a function of droplet diameter

| $Q$ ($\mu$L/s) : | 8.45 | 8.57 | 16.67 | 20.0 |
|---|---|---|---|---|
| at hollow electrode: | □ | — | — | + |
| at Faraday cup: | ▽ | △ | ○ | ◇ |

····· Modified Rayleigh instability limit model, Equation (6.21)
- - - - - Modified Vonnegut & Neubauer model, $\frac{1}{2}\times$ Equation (6.21)

locations; while for the hollow electrode connected to the power supply droplet charge was measured only at Faraday cup. The results shown in Figure 6.12 indicate that droplet can acquire relatively higher electric charge initially from the hollow electrode possibly due to unipolar charge injection (Atten and Moreau, 1972) and induction charging (Cross, 1987) mechanisms under high electric field intensity, and then gradually lose most of its acquired charge on the way travelling downstream probably due to recombination with other charged species in bulk dielectric continuous phase (Kitahara, 1984) or by discharging to the grounded planar electrode wall (Chang, *et al.*, 1990). On the other hand, the charge on the droplet measured at Faraday cup is much lower if the hollow electrode is connected to the power supply instead to the ground, as seen in Figure 6.12. This is consistent with the results of numerical electric field modelling. When the hollow electrode is connected to the power supply, there is only one high electric field intensity region which is near the hollow electrode. However, when the hollow electrode is connected to the ground, there are two high electric field intensity regions (as described in Chapter 4): one is near the hollow electrode the other is located at planar electrodes which is connected to the power supply. Therefore the magnitude of charge acquired or loss on the droplet in two different connection modes is expected to be different.

As shown in Figure 6.12, the modified Rayleigh instability model (Equation (6.21)) together with the modified Vonnegut & Neubauer model have been included for comparison with the experimental results. The modified Vonnegut & Neubauer model can correlate most of the experimental results obtained at hollow electrode where the electric field intensity is high, except for the large drop size which is equivalent to the single droplet regime with low applied voltages as seen in the figure. Therefore based on the modified Vonnegut & Neubauer model, the mechanism of droplet break up at hollow electrode may be postulated: the EHD instability generated at high applied voltages probably due to over-charging of the droplet at hollow electrode is dominated by charge injection and induction charging mechanisms

as already discussed in previous section.

Figure 6.13 compares the results in terms of droplet volume charge density at hollow electrode while Figure 6.14 compares the results in terms of droplet charge-to-mass ratio with those reported in previous work (Thornton, 1968; Bailes, 1981; Takamatsu *et al.*, 1981), when hollow electrode is grounded in the present liquid-liquid system. As seen in Figures 6.13 and 6.14, all the previous results which are obtained from three different sources are located at the lower right side of the figure, since the previous work only covers single discrete droplets at lower applied voltages. Therefore the drops are relatively large and the gravitation effect on the forming drop is still important as well as the electric field effect (He *et al.*, 1991). The results reported for the present work extend from single discrete droplet regime (at low applied voltage) to dispersed multi-droplet regime (at high applied voltage).

Figures 6.13 and 6.14 also indicate that the modified Vonnegut & Neubauer model is also better than the modified Rayleigh model for the correlation of maximum droplet charge density as well as the maximum charge-to-mass ratio in the present liquid-liquid system, as it correlates most of the experimental results obtained in this work and the results of reported previous work when the applied electric field is high enough and charge injection becomes dominant.

## 6.7 Mechanisms of EHD Droplet Formation and Dispersion

The mechanisms of EHD droplet formation and dispersion from hollow electrode have been proposed based on the results obtained from present liquid-liquid two phase system and from reported previous work (Thornton, 1968; Bailes, 1981; Takamatsu *et al.*, 1981). This can be explained in terms of three different droplet formation modes, which have been described in Chapter 5 and this chapter.

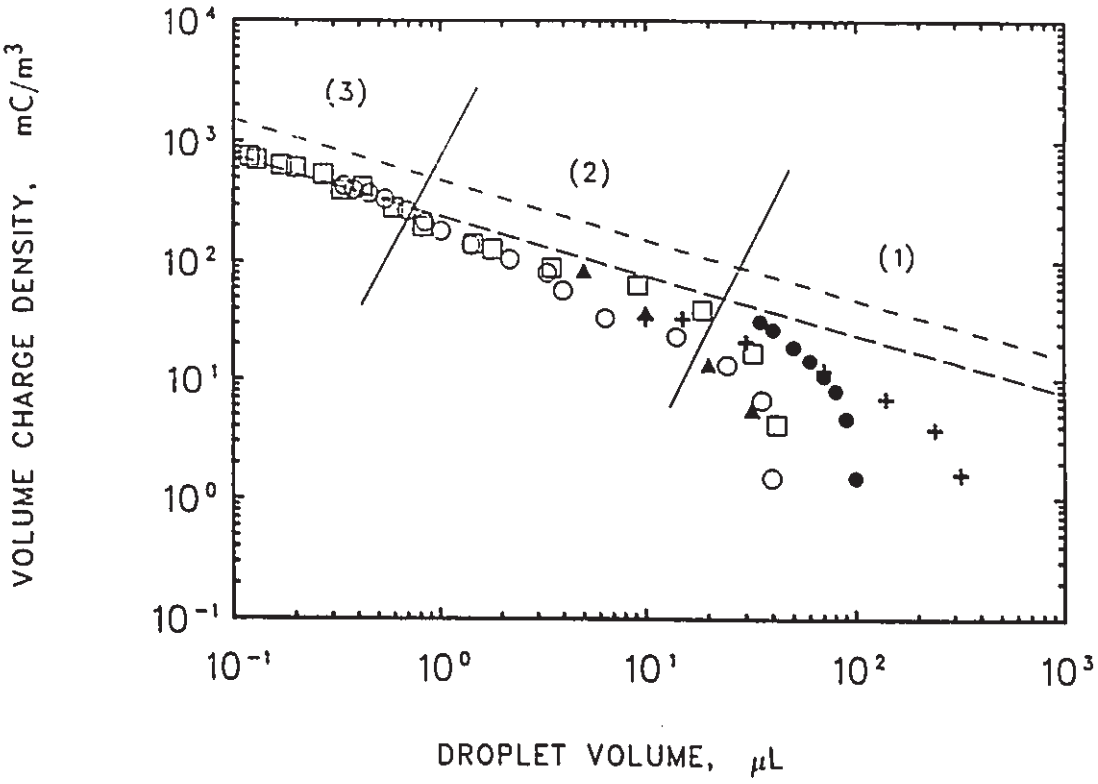


Figure 6.13: Comparison of volume charge density with models and literature (hollow electrode connected to ground)

□ — 7.1 μL/s ○ — 21.0 μL/s
▲ — Thornton (1968) ● — Bailes (1981)
\+ — Takamatsu *et al.*(1981)

- - - - - Modified Rayleigh instability limit model, Equation (6.22)
– – – – Modified Vonnegut & Neubauer model, $\frac{1}{2}\times$ Equation (6.22)

(1) Single droplet regime controlled by gravitational force;
(2) Single droplet regime controlled by EHD force;
(3) Multi-droplet regime controlled by EHD force.

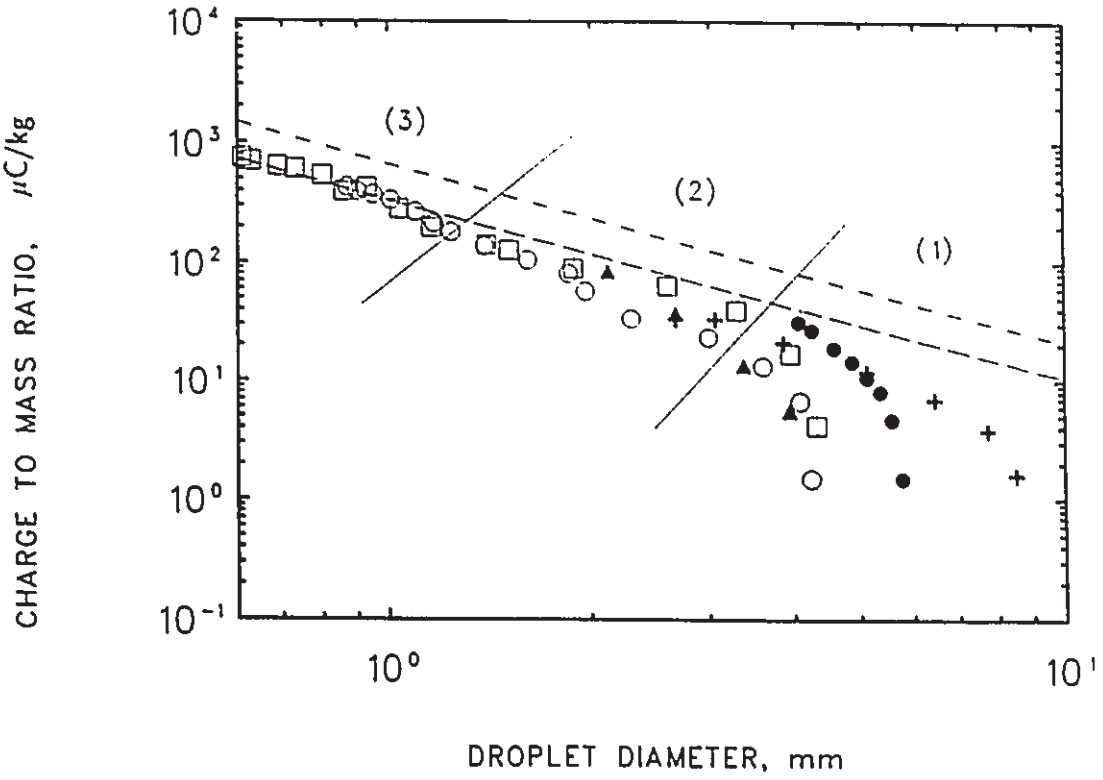


Figure 6.14: Comparison of droplet charge-to-mass ratio with models and literature (hollow electrode connected to ground)

□ — 7.1 μL/s ○ — 21.0 μL/s
▲ — Thornton (1968) ● — Bailes (1981)
\+ — Takamatsu *et al.*(1981)

- - - - - Modified Rayleigh instability limit model, Equation (6.23)
– – – – Modified Vonnegut & Neubauer model, $\frac{1}{2}\times$ Equation (6.23)

(1) Single droplet regime controlled by gravitational force;
(2) Single droplet regime controlled by EHD force;
(3) Multi-droplet regime controlled by EHD force.

**Single droplet regime controlled by gravitational force with applied voltages less than 2 kV:**

Droplets formed at applied voltages less than 2 kV would behave as those formed in the absence of electric fields as described in Chapter 5, *i.e.* single droplet detaches from hollow electrode vertically downward. The gravitation is still the dominant body force and the EHD forces are negligible. Therefore the droplet could not acquire enough induced charge to reach the maximum value before it detaches from hollow electrode, and the charge induced on droplet could be mainly from charge induction in dispersed phase or possibly from the effect of flow electrification (Cross, 1987). As shown in Figures 6.12 to 6.14, the area marked (1) which covers the data scattered below the modified Vonnegut & Neubauer model represent this kind of droplet formation mode. It is noted that most of the data from reported previous work are located in this mode, since all these work was conducted at single droplet region. After droplet detaches from hollow electrode, its initial velocity is very close to the droplet terminal velocity of those in the absence of applied electric field.

**Single droplet regime controlled by EHD force with applied voltages 2–7 kV:**

Droplets formed at applied voltages between 2 to 7 kV would behave as shown in the photograph of Figure 6.1(a), featuring smaller droplets and higher detachment frequencies than those observed in the first formation mode. The detached drops do not move off vertically but show alternating diverging paths which indicate the EHD force effect on both droplet size reduction and its subsequent repulsion due to the acquired charge. The charge acquired on droplet could be mainly from charge induction in dispersed phase.

As shown in Figures 6.12 to 6.14, the area marked (2) which covers the data very close to but still below the modified Vonnegut & Neubauer model represent this

type of droplet formation mode. This means that the charge acquired on the forming droplet does not reach the maximum charge limit. After droplet detaches from hollow electrode, its initial velocity is higher than the terminal velocity because of the droplet acceleration caused by charged droplets repulsion (He *et al.*, 1991).

**Multi-droplet regime controlled by EHD force with applied voltages above 7 kV:**

Droplets formed at applied voltages above 7 kV would behave as shown in the photograph of Figure 6.1(b). A multi-droplet formation would occur in which a fine dispersion of drops bursts from the hollow electrode at very high velocities, then gradually decelerated away to reach their terminal velocities. The fine droplet size and very high initial droplet velocity indicate the dominant EHD force at high electric field intensity. The charge induced on these dispersed droplets could be mainly from unipolar charge injection and charge induction in dispersed phase based on the postulated mechanism made on current flow in Section 6.5.

As shown in Figures 6.12 to 6.14, the area marked (3) which covers the data coincide with the predictions of modified Vonnegut & Neubauer model. This means that the charges acquired on these fine dispersed droplets have all reached their maximum charge limit which determines and controls the droplet size. Then the EHD force generated at high electric field would contribute to the dispersion and acceleration of the droplets as observed. Thus the initial velocities of these droplets are significantly enhanced, as shown in Figures 6.5 and 6.6.

# Chapter 7

# Electric Field Effect on Droplet Mass Transfer

## 7.1 Introduction

The application of high voltage electric field to enhance the rate of mass transfer in liquid-liquid extraction has been an active subject of investigation for past 25 years. Among the large amount of published work, there have been several review papers and short articles which have summarized most of the work to date (Thornton, 1968; Baird, 1983; Scott, 1989; Weatherley, 1992; Ptasinski and Kerkhof, 1992). The general idea of directly using an electric field to improve the performance of mass transfer in liquid-liquid extraction was initially described by Stewart and Thornton (1967). The improvement of interfacial mass transfer may be achieved in several ways due to the additional electrohydrodynamic (EHD) forces on the droplet-continuum interface: (1) reducing the effective interfacial tension; (2) increasing interfacial area for mass transfer and (3) enhancing interfacial disturbance and drop circulation.

It has been realized that a proper mass transfer system, appropriate experimental variables as well as the interpretation schemes are important to the investigation of the electric field effect on liquid-liquid mass transfer mechanisms. Chapter 6 has mainly focused on the droplet hydrodynamics under an imposed electric field (He *et al.*, 1991). Both drop size and velocity were experimentally determined. Information about electric charge (including free charge and induced charge) on the forming droplets and the electric field intensity inside the experimental cell are also very important to study the EHD effects on the mechanisms of drop formation and motion in another immiscible liquid phase (see Chapter 4 and Chapter 6). This chapter reports drop mass transfer experiments in the creeping flow regime, with distilled water as dispersed phase. Mass transfer of benzoic acid from the dispersed phase to the continuous phase has been investigated, without and with an imposed d.c. non-uniform electric field.

## 7.2 Mass Transfer in the Absence of Electric Field

Considerable experimental and theoretical work has been done on mass transfer to or from an isolated drop moving through a continuous phase without any external force imposed except gravity. In general, mass transfer occurs in three different stages (Skelland and Minhas, 1971): (1) during formation at a hollow nozzle; (2) during free rise or free fall; and (3) during coalescence at an interface. In order to investigate the mechanisms of drop mass transfer during its free rise or free fall period, the proportion of the mass transfer that occurs during drop formation and coalescence periods, the so called "end effects", must be evaluated.

The magnitude of the "end effects" has usually been estimated by varying the height for steady rise or fall of the drop and extrapolating the amount of mass transfer to zero height (Slater *et al.*, 1988), with precautions to minimize the effect

of droplet coalescence. An experimental technique in which drops are formed and withdrawn at the same nozzle, without release (Popovich *et al.*, 1964; Streicher and Schügerl, 1977), provides data on the rate of mass transfer while a drop is growing at a nozzle. The third approach is of using various plotting techniques for combining "end effects" analysis and the examination of the mass transfer mechanism (Johnson and Hamielec, 1960). It is this approach that has been used in this work to investigate the drop mass transfer mechanism for both charged and uncharged drops.

Mass transfer from the drop phase to a continuous phase may be expressed as the changes in solute concentration inside the drop based on the three stage mechanism with the assumption of concentration homogeneity within the drop:

$$C_0 \xrightarrow{\text{forming}} C_1 \xrightarrow{\text{falling}} C_2 \xrightarrow{\text{coalescing}} C_3$$

The fractional approaches to each concentration equilibrium (mass transfer efficiency) during drops' formation, free fall and coalescence, respectively have been defined by Johnson and Hamielec (1960) as follows:

$$E_{df} = \frac{C_0 - C_1}{C_0 - C^*} \tag{7.1}$$

$$E_{ff} = \frac{C_1 - C_2}{C_1 - C^*} \tag{7.2}$$

$$E_{dc} = \frac{C_2 - C_3}{C_2 - C^*} \tag{7.3}$$

where $E_{df}$, $E_{ff}$ and $E_{dc}$ are the efficiencies for drop mass transfer at different stages respectively and $C^*$ is the solute concentration in a drop which is in equilibrium to that in the continuous phase. It is assumed that $C^*$ is the same for each of the three mass transfer steps. In practice only $C_0$ and $C_3$ are directly measurable, and the corresponding overall (total) efficiency is related to the three contributing efficiencies:

$$E_t = \frac{C_0 - C_3}{C_0 - C^*} = 1 - (1 - E_{df})(1 - E_{ff})(1 - E_{dc}) \tag{7.4}$$

It is assumed in this work that the very low diffusivity of the benzoic acid in mineral oil and very high viscosity of the continuous phase as well as the specially

designed experimental setup make the mass transfer during drop coalescence stage negligible. Therefore $E_{dc}$ is considered to be zero in this work, so that $C_2 \simeq C_3$; then Equation (7.4) can be simplified and rearranged in logarithmic form:

$$\ln(1 - E_t) = \ln(1 - E_{df}) + \ln(1 - E_{ff}) \tag{7.5}$$

Generally, the overall mass-transfer coefficient based on the dispersed phase is defined as $K_{od}$, which may be expressed as:

$$\frac{1}{K_{od}} = \frac{1}{k_d} + \frac{1}{m\,k_c} \tag{7.6}$$

The subscript *od* will be omitted for the sake of simplicity in the following descriptions. Then, $K_{df}$ is defined as overall mass-transfer coefficient during drop formation stage and $K_{ff}$ is defined as overall mass-transfer coefficient during drop free fall stage. Obviously, both $K_{df}$ and $K_{ff}$ are based on the dispersed phase.

Since in the present mass-transfer system, $\mathcal{D}_c \ll \mathcal{D}_d$ (refer to the property table 3.3) and the equilibrium distribution constant, $m$, of benzoic acid concentration is approximately equal to unity as shown in Chapter 3, the dispersed phase offers negligible resistance. Therefore Equation (7.6) may be simplified as (Licht and Pansing, 1953):

$$K \simeq m\,k_c \simeq k_c \tag{7.7}$$

### 7.2.1 Single droplet mass transfer during droplet formation

The expression for $K_{df}$ is obtained from a mass balance based on the time averaged drop surface area and drop volume during drop formation:

$$-V_{av}\frac{dC}{dt} = K_{df}A_{av}(C - C^*) \tag{7.8}$$

The integrated form of Equation (7.8) is

$$-\int_{C_0}^{C_1}\frac{dC}{(C - C^*)} = K_{df}\left(\frac{A_{av}}{V_{av}}\right)\int_0^{t_{df}} dt \tag{7.9}$$

or

$$\ln(1 - E_{df}) = \ln(\frac{C_1 - C^*}{C_0 - C^*}) = -K_{df}(\frac{A_{av}}{V_{av}})t_{df} \tag{7.10}$$

Where $A_{av}$ is the time averaged droplet surface area during its formation period. For a spherical growing droplet with $d_t$ as diameter and surface area of $\pi d_t^2$ at time $t$, it is noted that

$$Q\ t = \frac{1}{6}\pi d_t^3, \quad \text{and} \quad dt = (\frac{\pi d_t^2}{2Q})dd_t$$

in which $d_t = d$ when $t = t_{df}$. Therefore the expressions for $A_{av}$ and $V_{av}$ are as follows:

$$A_{av} = \frac{1}{t_{df}}\int_0^{t_{df}} \pi d_t^2 dt = \frac{3}{5}\pi d^2 \tag{7.11}$$

and

$$V_{av} = \frac{1}{t_{df}}\int_0^{t_{df}} \frac{1}{6}\pi d_t^3 dt = \frac{1}{12}\pi d^3 \tag{7.12}$$

The time averaged area and volume are respectively 3/5 and 1/2 of the final values. Equations (7.11) and (7.12) are substituted into Equation (7.10) to obtain:

$$-\ln(1 - E_{df}) = (\frac{36}{5})(\frac{K_{df}t_{df}}{d}) \tag{7.13}$$

Various mechanisms proposed in the literature for mass transfer during droplet formation (Popovich *et al.*, 1964) were based on the unsteady-state diffusion theory with different assumptions about the hydrodynamics of the drop formation process. All these models can be considered as modifications of the Higbie's penetration theory (1935), according to which mass transfer is determined only by the molecular diffusivity and the contact time:

$$K_c = \mathcal{Z}(\frac{\mathcal{D}_c}{\pi\ t_{df}})^{\frac{1}{2}} \tag{7.14}$$

where $\mathcal{Z}$ is a dimensionless constant which depends upon the assumptions made for diffusion combined with the growth rate of drop volume and interfacial area.

Equation (7.14) is used in combination with Equation (7.7) to substitute for the $K_{df}$ term in Equation (7.13) which is then combined with Equation (7.5) to obtain

the following correlation equation:

$$-\ln(1-E_t) = [(\frac{36}{5})(\frac{\mathcal{Z}}{d})(\frac{\mathcal{D}_c}{\pi})^{\frac{1}{2}}]t_{df}^{\frac{1}{2}} - \ln(1-E_{ff}) = \mathcal{C}\, t_{df}^{\frac{1}{2}} - \ln(1-E_{ff}) \qquad (7.15)$$

where $\mathcal{C}$ is a proportionality constant subject to the assumption that $d$ in Equation (7.13) is constant. Therefore if the experimental values of $-\ln(1-E_t)$ are plotted against the square root of the drop formation time, $t_{df}^{\frac{1}{2}}$, a straight line should be obtained with the slope of $\mathcal{C}$ and an intercept of $-\ln(1-E_{ff})$. Then the dimensionless constant $\mathcal{Z}$ can be determined from the measured slope $\mathcal{C}$:

$$\mathcal{Z} = \mathcal{C}\,(\frac{5d}{36})\,(\frac{\pi}{\mathcal{D}_c})^{\frac{1}{2}} \qquad (7.16)$$

Figure 7.1 shows the plot of the single drop mass transfer results in the absence of electric field based on Equation (7.15). The least square linear regression gives the following correlation results: $\mathcal{C} = 0.015, s^{-\frac{1}{2}}$; $-\ln(1-E_{ff}) = 0.183$ with the correlation coefficient $R = 0.88$. Figure 7.2 (a) shows the droplet diameters observed at different drop phase flow rates. Given the observed average drop diameter 0.43 cm and molecular diffusivity $0.215 \times 10^{-6}$ cm$^2$/s, it can be shown from Equation (7.16) that $\mathcal{Z} = 3.42$.

Heertjes (1954) had proposed a model in which diffusion occurred in a very thin boundary layer near the drop surface, and was enhanced by the stretching of the surface as the drop grew. According to the Heertjes model,

$$k_c = \frac{24}{7}(\frac{\mathcal{D}_c}{\pi\, t_{df}})^{\frac{1}{2}} \qquad (7.17)$$

Hence $\mathcal{Z} = 3.43$ which is in good agreement with the present result.

### 7.2.2 Single droplet mass transfer during drop free fall

The mass balance equation derived for single drop mass transfer during its free fall is similar to that for drop formation. The assumptions that the drop size and mass

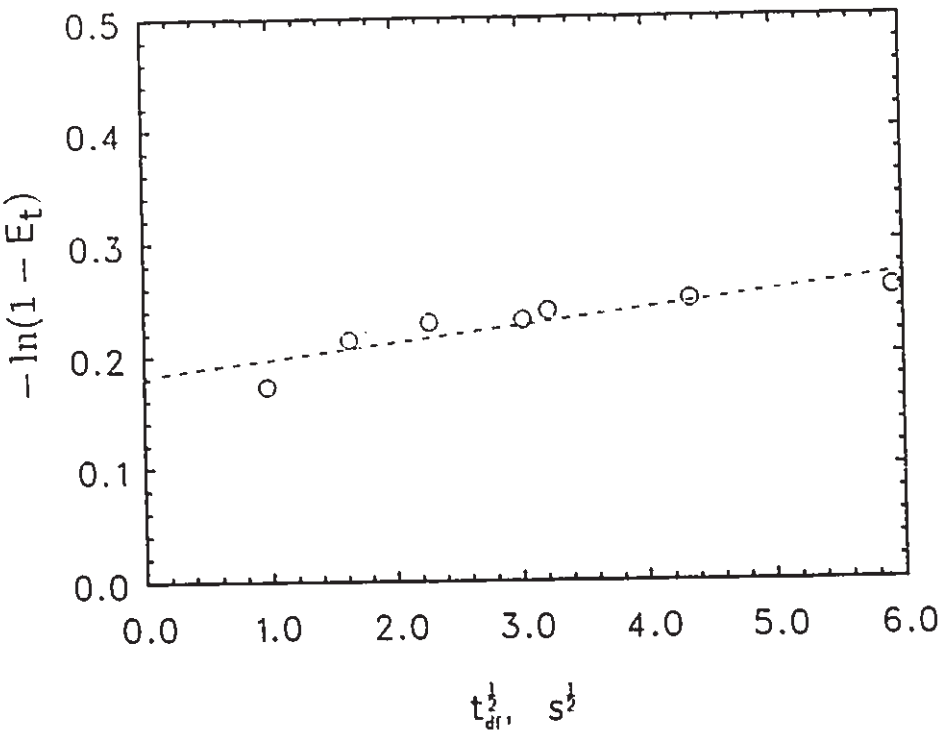


Figure 7.1: Correlations of observed mass transfer data in accordance with Equation (7.15)

Slope = 0.015, $s^{-1/2}$ Intercept = 0.183

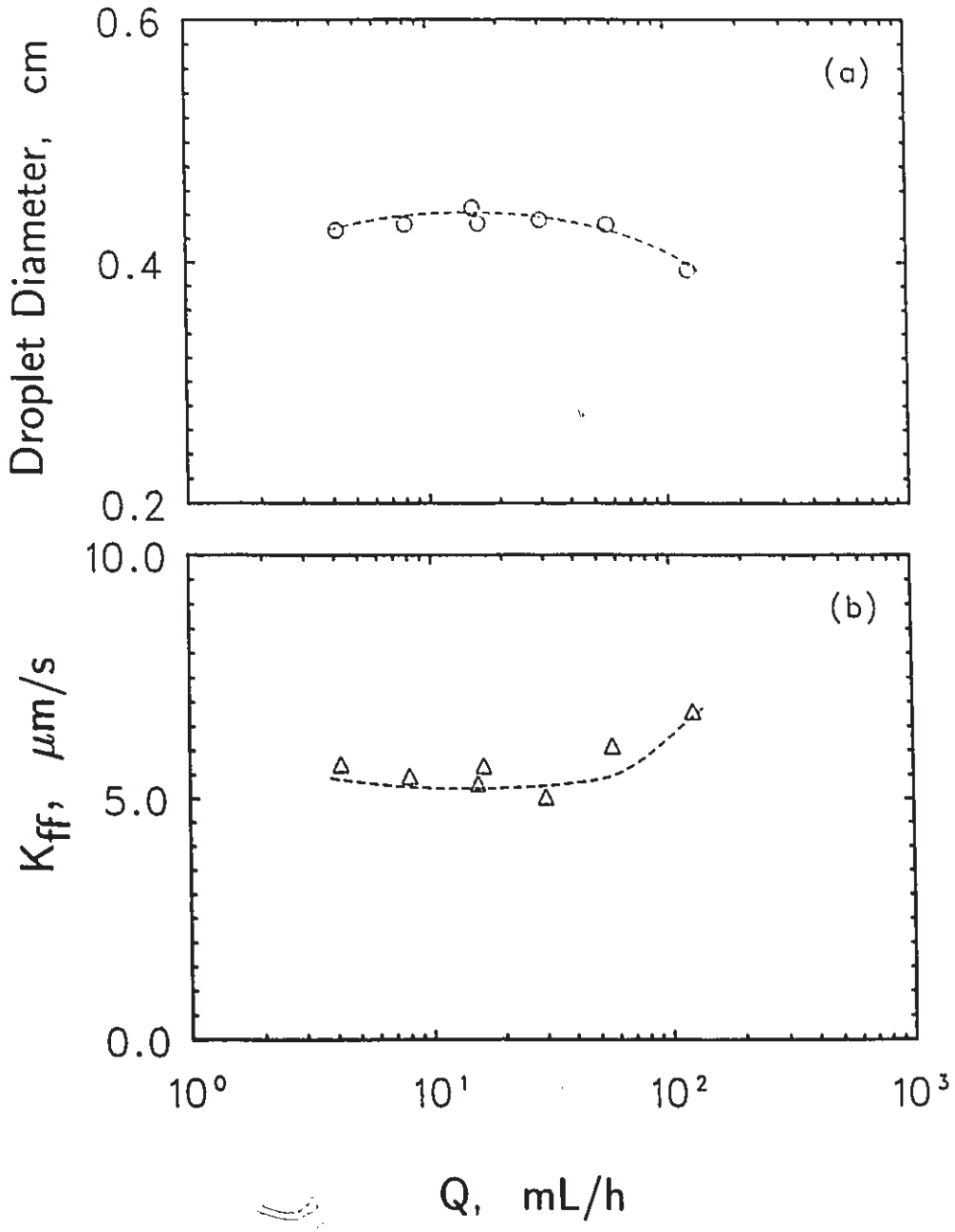


Figure 7.2: Detached droplet diameters and mass transfer coefficients during drop free fall in the absence of electric field

(a) droplet diameters
(b) droplet mass transfer coefficients

transfer coefficient remain constant during its free fall lead to the equation:

$$-\ln(1-E_{ff}) = (\frac{6}{d})\, K_{ff}\, t_{ff} \tag{7.18}$$

therefore

$$K_{ff} = -(\frac{d}{6\, t_{ff}})\, \ln(1-E_{ff}) = -(\frac{d\, v_t}{6\, H})\, \ln(1-E_{ff}) \tag{7.19}$$

where $v_t$ is the terminal velocity of the drops and $H$ is the total distance for drop free fall in the continuous phase. Experimentally,

$$-\ln(1-E_{ff}) = 0.183$$

based on the intercept shown in Figure 1.

As seen in Figure 7.2 (b) which shows individually calculated values of $K_{ff}$ as a function of dispersed phase flow rate, the mass-transfer coefficient during drop free fall is generally constant except at the two highest flow rates in the present experimental conditions. The explanation of the increased $K_{ff}$ at the higher drop phase flow rates is that the interactions between the consecutive drops at the higher drop detachment rate probably enhance the disturbance on the drops surface as well as internal circulation of the drops.

Higbie's model (1935) assumes that the drop surface is mobile with surface renewal occurring at time interval of $t = d/v_t$. This corresponds to

$$K_{ff} = 2(\frac{\mathcal{D}_c v_t}{\pi d})^{\frac{1}{2}} \tag{7.20}$$

A good agreement between the experimental correlations of $K_{ff}$ and the Higbie's penetration model as shown in Figure 7.3 indicates that the drops were circulating during droplet free fall for the present mass transfer system in the absence of applied electric field.

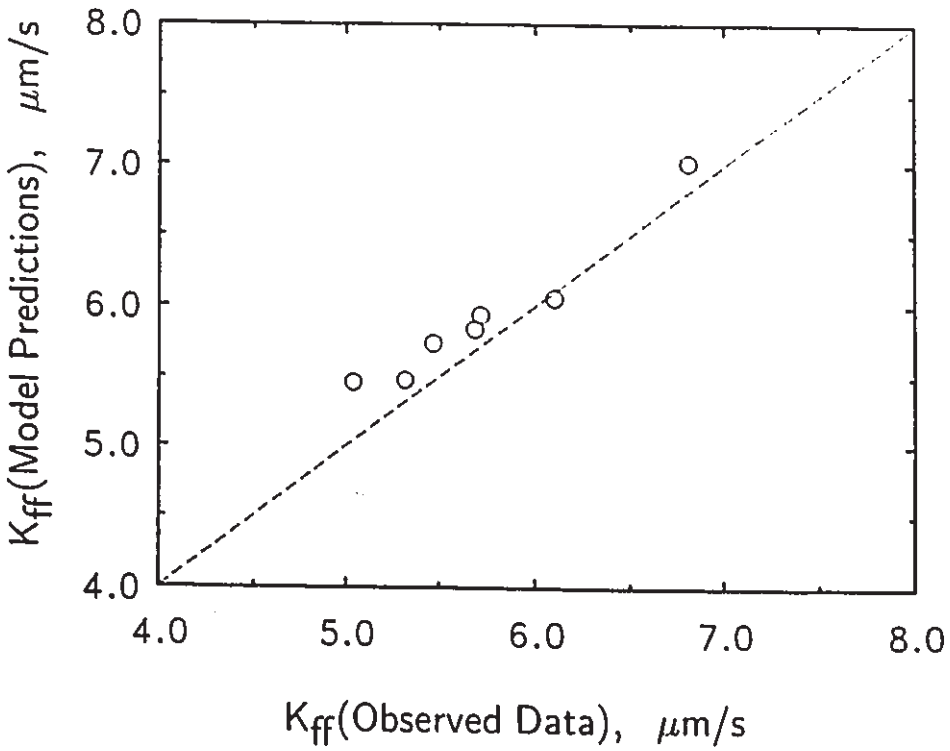


**Figure 7.3: Comparison of observed single droplet mass transfer coefficient with the Higbie penetration model, Equation (7.20)**

## 7.3 Mass Transfer in the Presence of Electric Field

The observed behavior of charged droplets formed under the applied electric field during mass transfer experiments was similar to that described in Chapter 6 and by He *et al.* (1991). The results for the diameters of charged droplets at two different drop phase flow rates during mass transfer are plotted against the applied voltages as shown in Figure 7.4. Under the effect of electric field both drop size reduction and enhancement of drop initial velocity were significant, especially at higher applied voltages. Therefore larger interfacial areas were generated and interfacial disturbance might be enhanced as well, compared with the results obtained in the absence of electric field. These phenomena provide the possibilities for enhancing the mass transfer rate in liquid-liquid extraction processes.

The total mass transfer performances were enhanced based on the experimental results conducted in this work. As shown in Figure 7.5 (a), the total mass transfer efficiencies, $E_t$ measured at 10 kV applied voltages are much higher than those measured in the absence of electric field for various drop phase flow rates. As seen in Figure 7.5 (b), the total mass transfer efficiency is increased approximately by 2–4 times in the present range of investigation. The relative total mass transfer efficiency, $R$ has been defined as the ratio of $E_t$ with electric field divided by the $E_t$ without electric field, for the same drop phase flow rate. Figure 7.6 shows that the total mass transfer efficiency, $E_t$, for two different drop phase flow rates is significantly enhanced in the presence of high voltage electric field, with a greater enhancement at the lower flow rate.

It was observed during experiments that in the presence of electric field the drop formation period was much shorter than the duration of its free fall. The droplets formed were of uniform size at a fixed applied voltage, even in the drop dispersion regime at very high applied voltages. Therefore the mass transfer enhancement during the drop formation stage may be primarily due to the effect of increased specific

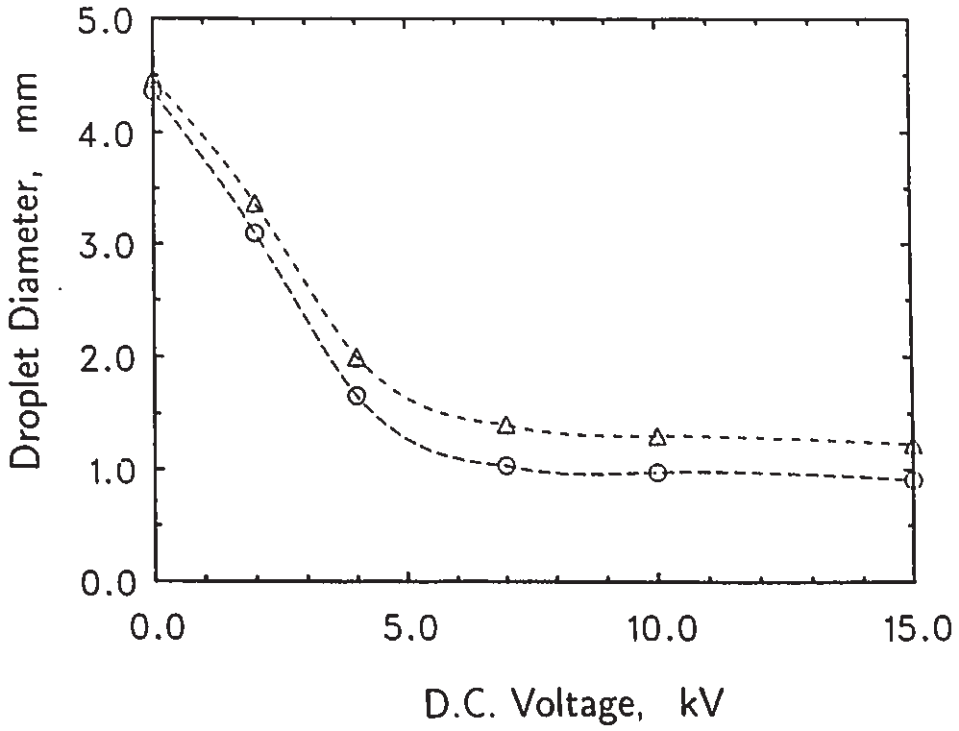


**Figure 7.4: Droplet diameters as a function of applied D.C. voltages and drop phase flow rate, with mass transfer**

○ — 8.33 $\mu$L/s  △ — 16.67 $\mu$L/s

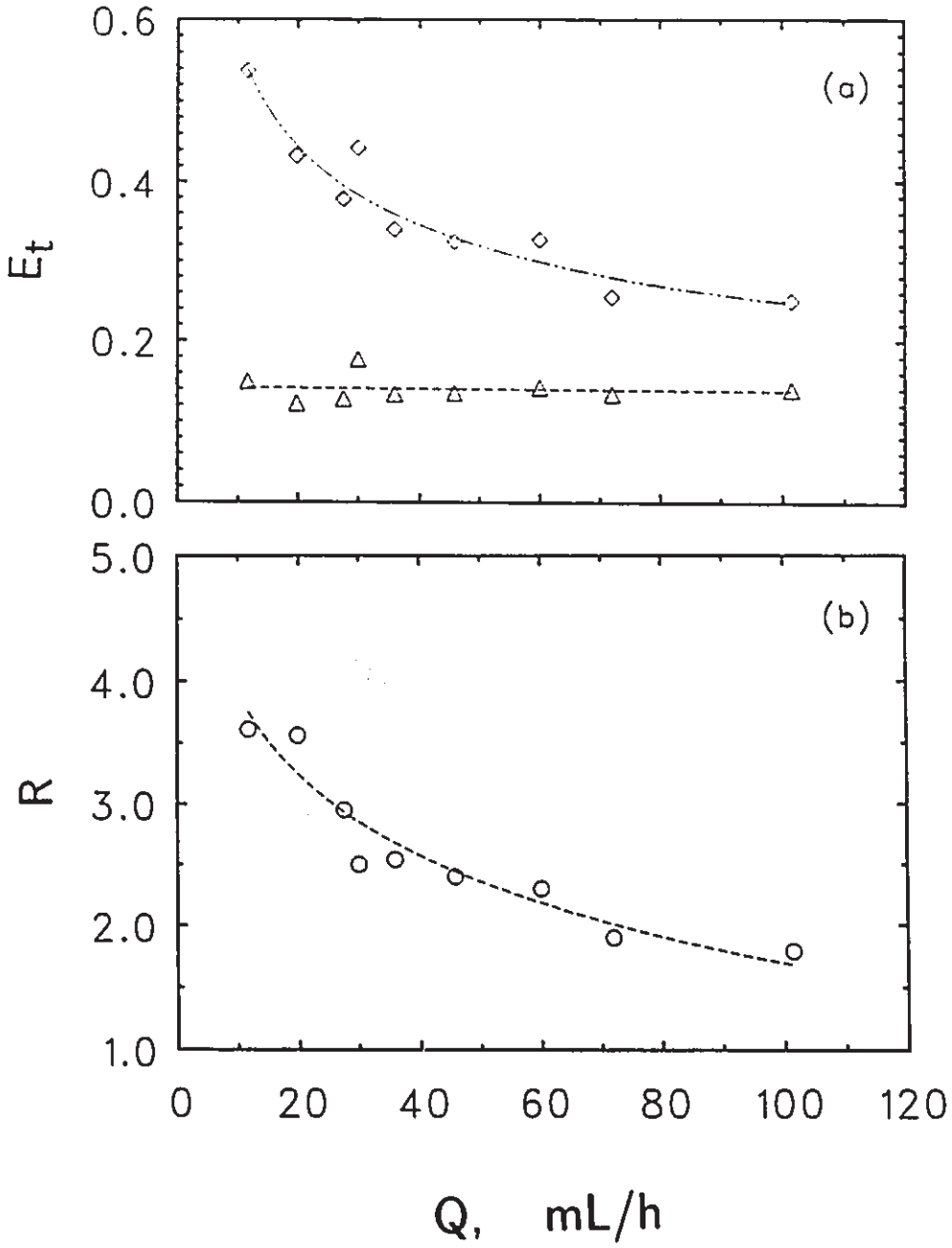


Figure 7.5: Total mass transfer efficiency as the function of drop phase flow rate

(a) ◇ — voltage: 10 kV  △ — voltage: 0 kV
(b) relative ratio of total mass transfer efficiency

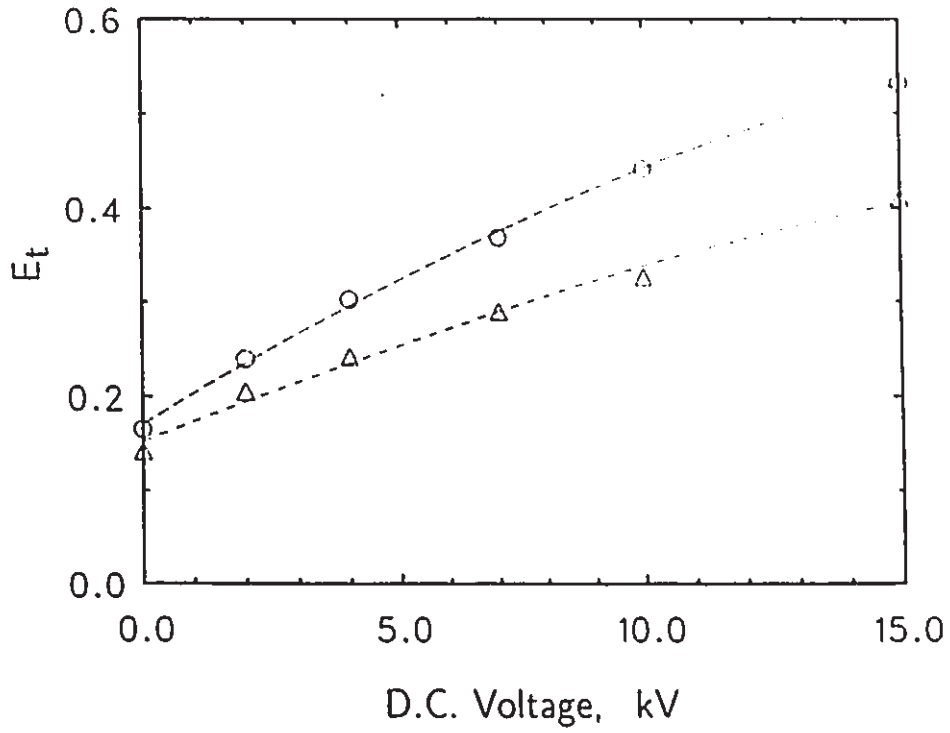


Figure 7.6: Total mass transfer efficiency as a function of DC applied voltage and drop phase flow rate

○ — 8.33 $\mu$L/s  △ — 16.67 $\mu$L/s

interfacial area associated with reduced drop diameter. This confirms that droplets formed *of the same drop size* have the equivalent mass transfer characteristics during formation for a given setup geometry and system, as postulated by Bailes (1981). The drop coalescence contribution to mass transfer with the applied voltage ($E_{dc}$) is still considered negligible, as in the absence of electric field. Then Equation (7.15) may still be used to evaluate $K_{df}$ for the charged drop mass transfer during drop formation provided the drop size be considered as a variable as well as the time duration for drop formation. In the case of imposed electric field at a fixed drop phase flow rate, different drop diameters indicate the implicit values of different applied voltages. Equation (7.15) may be written in terms of droplet diameter and drop phase flow rate with the substitutions of $t_{df}(=\frac{\pi d^3}{6Q})$ and Equations (7.14) and (7.16) then lead to:

$$K_{df} = C'(\frac{Q}{d})^{\frac{1}{2}} \tag{7.21}$$

where $C' = C(\frac{5}{36})(\frac{6}{\pi})^{\frac{1}{2}}, s^{-\frac{1}{2}}$ and $C$ is obtained experimentally (see Figure 7.1). Therefore the modified model of Equation (7.21) can be used to estimate mass transfer coefficient during drop formation for both uncharged and charged droplet mass transfer cases. Once $K_{df}$ can be estimated for charged drop mass transfer using Equation (7.21), the mass transfer efficiency for charged drop formation stage, $E_{df}$, can also be calculated through Equation (7.13).

Figure 7.7 shows the results of the extended model of Equation (7.21), where the mass transfer coefficient, $K_{df}$ is plotted as the function of $Q/d$ together with the results for uncharged droplets. It is noted from Equation (7.21) that larger $K_{df}$ values can be obtained by either reducing drop size or increasing drop phase flow rate. In the case of uncharged drops, the drop size is constant; while for the charged drops, drop size becomes smaller when increasing the applied voltages. Obviously, the higher the applied voltage in the present mass transfer system, the larger the $K_{df}$ is obtained.

The mass transfer efficiency for charged drops in the free fall stage, $E_{ff}$, is

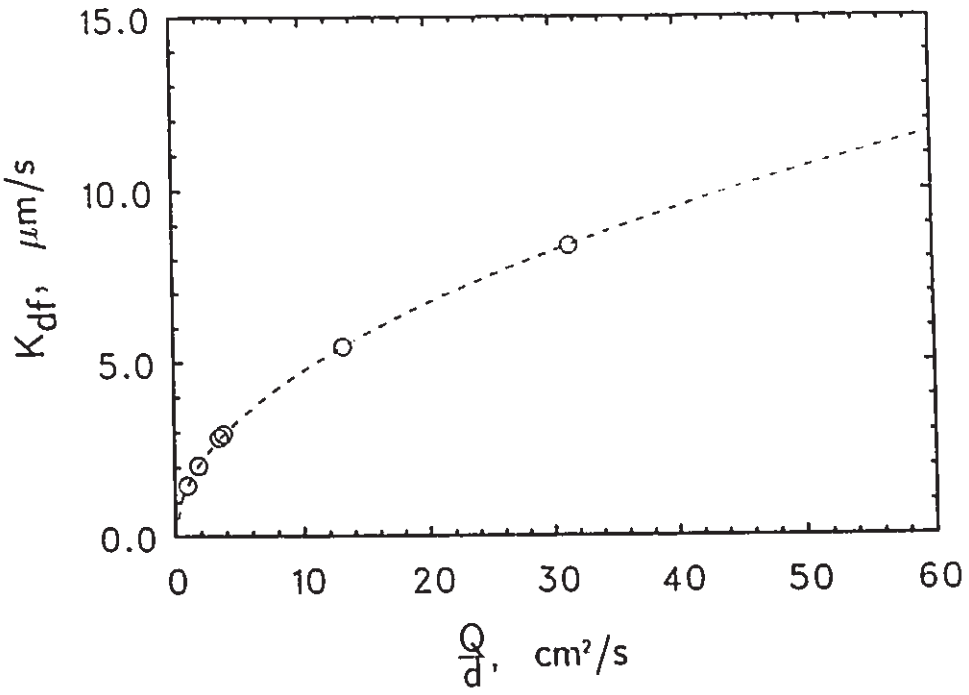


Figure 7.7: Mass transfer coefficient during drop formation as a function of the ratio of drop flow rate to drop diameter

○ — 0 kV, 1.16-34.36 μL/s - - - - - - Equation (7.21)

readily estimated using Equation (7.5) from the total measured mass transfer efficiency and correcting for $E_{df}$ evaluated from Equations (7.13) and (7.21) as described previously. Finally the mass transfer coefficient for charged drops in free fall, $K_{ff}$, can be calculated using Equation (7.19). The terminal velocity for charged droplets is evaluated using Stokes equation, since the electric field intensity in most of the cell downstream of the hollow electrode nozzle was so weak that the induced charges on the reduced drops were negligible based on the experimental results.

Mass transfer coefficients during drop free fall (found from Equation (7.19)) for both charged and uncharged drops are plotted as the function of drop diameter as shown in Figure 7.8. As seen in Figure 7.8, the mass transfer coefficient during drop free fall can be correlated quite well for all experimental results in this work in terms of droplet diameters. The $K_{ff}$ is reduced when the droplet size becomes smaller, irrespective of the flow rates or the applied voltage. This suggests that in this work there is no difference in the mass transfer mechanism during drop free fall, regardless of whether drops are formed in an electric field or not. According to the results of numerical modelling (reported in Chapter 4), the electric field intensity is highest at the region very near the hollow electrode nozzle and is sharply decreased in the other regions for the electrical field without space charge. Once the droplets are formed and dispersed away from the hollow electrode nozzle at the high applied voltages they behave in the same way as uncharged drops since their initial high velocities are rapidly decelerated in the highly viscous medium. Therefore, as long as the droplets formed have the same size, then they travel at virtually the same average terminal velocities during drop free fall, as observed experimentally. This is also consistent with the results from electric charge measurement as described in Chapter 6.

Figure 7.9 shows the correlations between Sherwood numbers and Reynolds numbers while Figure 7.10 shows the correlations between Sherwood numbers and Peclet numbers for the mass transfer results obtained in this work. Both figures give linear correlations on the log-log plots and are compared with two well-known existing

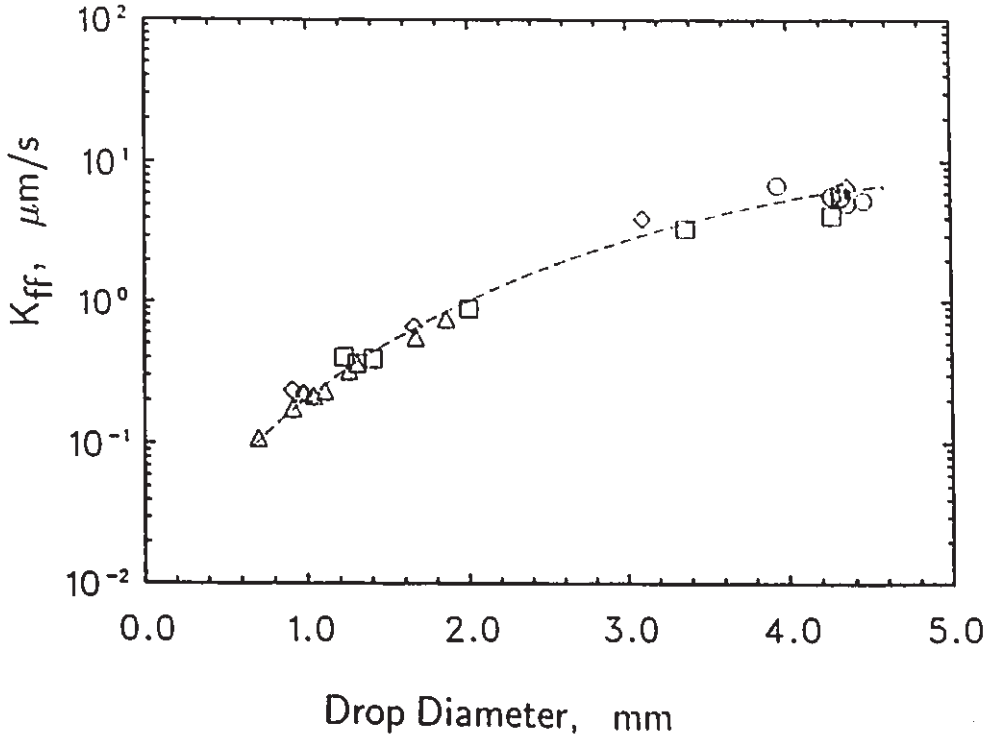


Figure 7.8: Mass transfer coefficient during drop free fall as a function of drop diameter

○ — 0 kV, 1.16-34.36 $\mu$L/s  △ — 10 kV, 3.25-28.17 $\mu$L/s
◇ — 0-15 kV, 8.33 $\mu$L/s  □ — 0-15 kV, 16.67 $\mu$L/s

models as shown in these two figures.

The Higbie model given by Equation (7.20) can be written as:

$$\mathrm{Sh}_c = (\frac{2}{\pi^{\frac{1}{2}}})(\frac{dv_t}{\mathcal{D}_c})^{\frac{1}{2}} = 1.13\,\mathrm{Pe}_c^{\frac{1}{2}} \tag{7.22}$$

The Ranz and Marshall (1955) equation has been widely applied to mass transfer from solid spheres or from drops or bubbles with immobile surfaces:

$$\mathrm{Sh}_c = 2.0 + 0.6\,\mathrm{Re}_d^{\frac{1}{2}}\,\mathrm{Sc}_c^{\frac{1}{3}} \tag{7.23}$$

The shift from Higbie model at relatively higher Reynolds numbers or Peclet numbers to the Ranz and Marshall model at relatively lower Reynolds numbers or Peclet numbers suggests that the drops were circulating during drop free fall when the drop size were relatively large (in the absence of electric field or at low applied voltages); as the applied voltage is increased, the drops became gradually rigid due to the reduced drop size and the increasing relative importance of trace interfacial contaminants.

The results indicate that the application of the electric field to the drop formation process does not change the fundamental mass transfer mechanisms and the mass transfer results obtained in this work both in the absence and in the presence of electric field can be described and correlated by existing mass transfer models. This leads to the conclusion that drops of the same size have equivalent mass transfer behavior, even for the case where drops are formed in the dispersion regime at high applied voltages. The results also suggest that the high viscosity of the continuous phase inhibits the drops oscillation as well as circulation during droplet free fall stage when the drop sizes become smaller under the applied high voltage electric field. Therefore the significant enhancement of mass transfer efficiency in the present work is mainly contributed by significantly increased specific interfacial area due to droplet size reduction and by enhanced droplet initial velocity due to strong local electrical forces

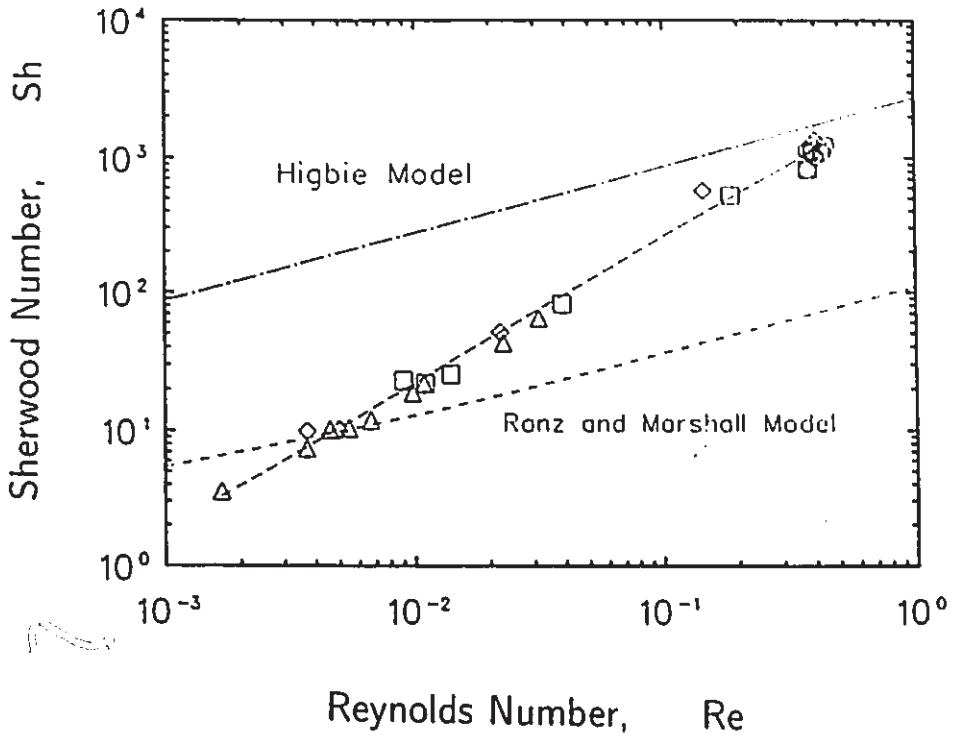


**Figure 7.9:** Correlation of Sherwood Number as a function of Reynolds Number

○ — 0 kV, 1.16–34.36 $\mu$L/s  △ — 10 kV, 3.25–28.17 $\mu$L/s
◇ — 0–15 kV, 8.33 $\mu$L/s  □ — 0–15 kV, 16.67 $\mu$L/s

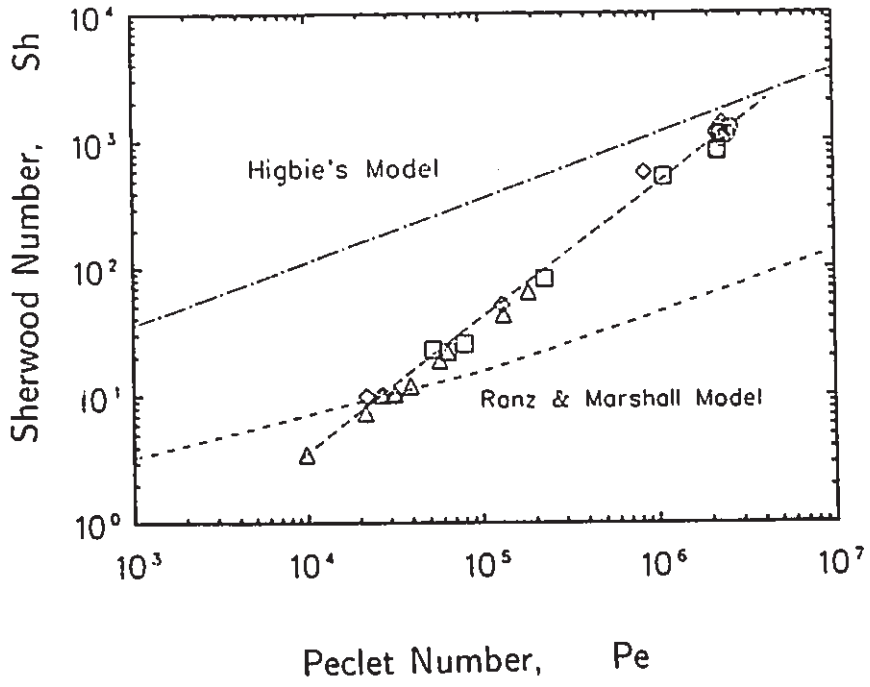


Figure 7.10: Correlation of Sherwood Number as a function of Peclet Number

○ — 0 kV, 1.16–34.36 $\mu$L/s  △ — 10 kV, 3.25–28.17 $\mu$L/s
◇ — 0–15 kV, 8.33 $\mu$L/s  □ — 0–15 kV, 16.67 $\mu$L/s

promoting rapid detachment of drops from the hollow electrode, which increases the mass transfer coefficient during the droplet formation stage.

# Chapter 8

# Conclusions

## 8.1 Conclusion on EHD Droplet Formation and Dispersion

Experimental investigations on droplet formation and dispersion in a viscous mineral oil have been conducted with and without the presence of an imposed DC non-uniform electric field. Attention has been concentrated on the relatively low dispersed phase flow rate region where discrete droplets form directly at the hollow electrode. Droplets formed in this system are spherical and of uniform size whether in the presence or in the absence of the electric field. This not only simplifies the data analysis in this work but also provides a special feature for the potential industrial applications.

The results obtained in the absence of electric field indicate that the formation and behavior of drops can be well described by the theory of low Reynolds number flow. The forming droplet diameters can be well predicted using mechanistic models based on a force balance. These provide a basis for comparison with the results obtained in the case when the electric field is applied.

The results obtained in the presence of a non-uniform DC electric field indicate

that droplets formed at hollow electrode are reduced significantly in size and show mutual repulsion and dispersion at high applied voltages; the droplet velocity near the hollow electrode is also significantly increased. Since the forming droplet diameter can be significantly reduced with the applied voltage increase, therefore the specific interfacial area can be significantly increased.

The model for EHD droplet formation has been derived with the inclusion of electric force component based on the force balance upon droplet detachment from hollow electrode. The dependences of electric force component on the applied voltage, droplet diameter and the drop phase flow rate have also been verified. It has been found that the electric field generated EHD force is proportional to the square of applied DC voltage as well as to the square of droplet diameter; but it is proportional to the $-0.57$ power of the dispersed phase flow rate.

## 8.2 Conclusion on EHD Droplet Mass Transfer

Mass transfer of benzoic acid from droplets in this two-phase liquid-liquid system has been studied with and without the presence of an imposed DC non-uniform electric field. Total mass transfer efficiency was significantly enhanced in the presence of the applied electric field. The experimental results indicate that total mass transfer efficiency can be increased by up to fourfold by an applied electric field (at 10 kV applied voltage).

The results have been correlated with a two stage mass transfer mechanism: the drop formation stage and the drop free fall stage, with the effect during drop coalescence stage being ignored. The results obtained from drop mass transfer investigation indicate that the mass transfer mechanisms of these electrically charged droplets during the droplet formation and its subsequent free fall are similar to those of droplets in the absence of electric field and can be correlated using the existing

mass transfer models, although these models were originally derived for single drop mass transfer. This leads to the conclusion that drops of the same size have equivalent mass transfer behavior, even for the case where drops are formed in the dispersion regime at high applied voltages. The increased specific interfacial area and the accelerated drop initial velocity in the presence of electric field are the main contributions to the enhanced efficiency of mass transfer performance in the present investigation.

## 8.3 Conclusion on Acquired Droplet Charge

The mechanisms of current conduction in the dielectric continuous phase and electrification of the droplets during EHD droplet formation have been postulated and discussed based on the observations of current-voltage characteristics of the system, the electric charge acquired by the droplet and the results from numerical electric field modelling.

The results obtained from current-voltage (I-V) characteristics of the liquid-liquid two-phase system suggest that the major part of current flow through hollow electrode when it is connected to the power supply may be due to the surface leak current through the LUCITE cell wall. Since there were no visible effects of the two connection modes on the droplet formation and dispersion from experimental observations in this work, it is therefore more energy efficient to connect the hollow electrode to the ground while connecting the planar electrodes to the high voltage power supply.

The modified Vonnegut & Neubauer model is better than the modified Rayleigh model for the correlation of maximum droplet charge density as well as the charge-to-mass ratio in the present liquid-liquid system, as it can correlate most of the experimental results obtained in this work and the results of reported previous work when the applied electric field is high enough.

The mechanisms of EHD droplet formation and dispersion from hollow electrode have been suggested based on comparisons of the modified Vonnegut & Neubauer model with the results obtained from present liquid-liquid two phase system and from reported previous work (Thornton, 1968; Bailes, 1981; Takamatsu *et al.*, 1981), as well as the results of numerical electric field modelling. This can be explained in terms of three different droplet formation modes.

- **Single droplet regime controlled by gravitational force:**
  Droplets formed at applied voltages less than 2 kV behave as those formed in the absence of electric fields, *i.e.* single droplet detaches from hollow electrode vertically downward. The gravitation is still the dominant body force and the EHD forces are negligible. Therefore droplet may not acquire enough induced charge to reach the maximum charge limit before it breaks up and detaches from hollow electrode, and the charge acquired on droplet could be mainly from charge induction in dispersed phase or possibly from the effect of flow electrification.

- **Single droplet regime controlled by EHD force:**
  Droplets formed at applied voltages 2–7 kV are featuring smaller droplets and higher detachment frequencies than those observed in the absence of electric field. The detached drops do not move off vertically but show alternating diverging paths which indicate the EHD force effect on both droplet size reduction and its subsequent repulsion. The charge acquired on droplet mainly by charge induction in the dispersed phase has not reached its maximum value before it released from the hollow electrode.

- **Multi-droplet regime controlled by EHD force:**
  Droplets are formed at applied voltages above 7 kV by a multi-droplet formation mode in which a fine dispersion of drops bursts from the hollow electrode at very high velocities, then gradually decelerates away to reach the steady

terminal velocities. The fine droplet size and very high initial droplet velocity indicate the dominant EHD force at high electric field intensity. The electric field induced charges on these dispersed droplets have all reached their maximum charge limit possibly due to the unipolar charge injection and charge induction in the dispersed phase. This maximum charge limit determines and controls the droplet size. Then the EHD force generated at high electric field would contribute to the dispersion and acceleration of the droplets. Thus the initial velocities of these droplets are significantly enhanced.

## 8.4 Conclusion on Numerical Electric Field Model and Results

In parallel to the experimental investigations, a numerical electric field model has been derived based on the axial symmetric approximation and with the appropriate coordinate transformations. A finite difference algorithm with the control volume approach has been used to conduct numerical calculations.

The numerical results of electric field profiles have been compared with the approximate analytical models in order to confirm the validity of the numerical model derived. The prediction of EHD forces on droplets has also been performed with some additional assumptions on electric charge information.

The numerical results obtained from the electric field profiles and predictions of the EHD force components on the droplet can provide much useful information to support the results obtained from experimental investigation such as (1) the effect of electrode connection mode on the current-voltage characteristics of the present liquid-liquid system (discussed in Chapter 6); (2) the charge acquired on the drops at different locations (discussed in Chapter 6); and (3) the mass transfer efficiency during droplet formation and during droplet free fall (discussed in Chapter 7). Therefore a

better understanding on the mechanisms of EHD droplet formation, dispersion and mass transfer conducted in this work has been achieved from numerical electric field modelling.

# Chapter 9

# Recommendations for Future Work

A number of potential research directions exist which could lead to productive future work from the results obtained in the present investigations.

- Fundamental research on droplet formation/dispersion should consider the interactions of electric field and electric-field-induced charge on hydrodynamics of the forming drop, in order to verify the postulated mechanisms and to derive a better droplet formation/dispersion model which can be used to calculate drop sizes and velocity profiles. These results can then be used to predict the EHD coupled mass transfer during droplet formation.

- The research on electric field enhanced mass transfer can be conducted on different mass transfer systems (continuous phase, dispersed phase and mass transfer species), and with different mass transfer directions. Although the choice of such systems is limited to liquids with appropriate electric properties, a significant number of liquid pairs with practical interest meet these requirements.

- Further research can be conducted on the modifications of apparatus geometry and electrode design to obtain higher electric field intensity downstream therefore the enhanced mass transfer during droplet free fall can be achieved, and droplet velocity can also be controlled by the applied electric field.

- The use of a pulsed electric field source to conduct research on electric field enhanced mass transfer is another approach to achieve better efficiency on energy consumption than the DC electric field source.

- A solution-adaptive mesh scheme strategy may be used in the numerical electric field modelling to reduce the error and to increase the resolution of the numerical solution. In this way, a fixed number of grid points can be adjusted to provide a "best" solution using the error message selected. The best choice on numerical electric field modelling is to consider a 3-D model which will be more close to the geometry of the real experimental cell.

# References


Abdel-Alim, A.H. and A.E. Hamielec, "A Theoretical and Experimental Investigation of the Effect of Internal Circulation on the Drag of Spherical Droplet Falling at Terminal Velocity in Liquid Media", Ind. Eng. Chem. Fundam. **14**, 308–312 (1975).

Allan, R.S. and S.G. Mason, "Particle Behaviour in Shear and Electric Fields I. Deformation and Burst of Fluid Drops", Proc. Roy. Soc. **267A**, 45-61 (1962).

Anderson, D.A., J.C. Tannehill and R.H. Pletcher, "Computational Fluid Mechanics and Heat Transfer", McGraw-Hill, New York (1984).

Atten, P. and R. Moreau, "Electrohydrodynamic Stability of Insulating Liquids subject to Unipolar Injection", J. Mécanic **11**, 471-520 (1972).

Austin, L.J., L. Banczyk and H. Sawistowski, "Effect of Electric Field on Mass Transfer across a Plane Interface", Chem. Eng. Sci. **26**, 2120–2121 (1971).

Bailes, P.J. and J.D. Thornton, "Electrically Augmented Liquid-liquid Extraction in a Two-component System, I. Single Droplet Studies", Proc. Intl. Solvent Extn. Conf. **ISEC'71** (J.G. Gregory, B. Evans and P.C. Weston, eds.), Soc. Chem. Ind., London, 1431–1439 (1971).

Bailes, P.J. and J.D. Thornton, "Electrically Augmented Liquid-liquid Extraction in a Two-component System, II. Multidroplet Studies", Proc. Intl. Solvent Extn.

Conf. **ISEC'74** (G.V. Jeffreys, ed.), Soc. Chem. Ind., London, 1011-1027 (1974).

Bailes, P.J. "Electrostatic Extraction for Metals and Non-metals", Proc. Intl. Solvent Extn. Conf. **ISEC'77** (B.H. Lucas, ed.), Can. Inst. Mining Met., Montreal, 233-241 (1977).

Bailes, P.J. and I. Wade, "Extraction of Copper(II) by Hydroxyoximes in An Electric Field", Proc. Intl. Solvent Extn. Conf. **ISEC'80**, Association des Ingenieurs Sortis de l'Université de Liège, 80-196 (1980).

Bailes, P.J."Solvent Extraction in An Electric Field", Ind. Eng. Chem. Process Des. Dev. **20**, 564-570 (1981).

Baird, M.H.I. "Electrostatic Effects on Extraction", in Chapter 8: Special Techniques, Handbook of Solvent Extraction (T.C. Lo, M.H.I. Baird and C. Hanson Eds.) 268-269, John Wiley & Sons, New York, N.Y. (1983).

Baird, M.H.I. and I. Nirdosh, "Surface and Interfacial Tension Measurement by Drainage Methods", Can. J. Chem. Eng. **59**, 369-376 (1981).

Basaran, O.A., Scott, T.C. and Byers, C.H., "Drop Oscillations in Liquid-Liquid Systems", AIChE J. **35**, 1263-1270 (1989).

Basaran, O.A., "Electrohydrodynamics of Drops and bubbles", Ph.D. Thesis, University of Minnesota (1984).

Bird, R.B., W.E. Stewart and E.N. Lightfoot, "Transport Phenomena", John Wiley & Sons, New York (1960).

Byers, C.H. and J.J. Perona, "Drop Formation from an Orifice in an Electric Field", AIChE J. **34**, 1577-1580 (1988).

Carleson, T.E. and J.C. Berg, "The Effect of Electric Fields on the Absorption of Pure Sulfur Dioxide by Water Drops", Chem. Eng. Sci. **38**, 871–876 (1983).

Carleson, T.E. and J.C. Berg, "Marangoni and Electric Field Effects upon Mass Transfer to Translating Drops", Chem. Eng. Commun. **25**, 117–131 (1984).

Carleson, T.E. and E. Fuller, "The Effects of Electrical Charge upon Mass Transfer from Drops Exhibiting Interfacial Turbulence", Chem. Eng. Comm. **57**, 277–287 (1987).

Chang, J.S., S. Mielke, S. Ogata and R.C. Scott, "Electromechanics and Fluidization Characteristics of Co-flow Type Electrofluidized Beds", J. Electrostat. **25**, 135–144 (1990).

Chang, J.S., "Electromagnetic Hydrodynamics – The Role of Electromagnetic Field on the Fluid Flow", Proc. 1986 Japanese Electrostatic Soc. EHD Symposium, **1**, 1–40 (1986).

Chang, J.S., "EHD Chemical Reactors: A Critical Review", Conf. Rec. IEEE IAS 1987 Annual Conference, 1471–1479 (1987).

Chang, J.S., "Industrial Dielectrophoresis and Electrohydrodynamics: Its Applications to Multi-phase Flow Apparatus" in Particle Phenomena and Multi-phase Transport, (T.N. Veziroglu ed.), **5**, 35–59, Hemisphere, Washington (1988).

Chang, L.S., T.E. Carleson, and J.C. Berg, "Heat and Mass Transfer to a Translating Drop in an Electric Field", Int. J. Heat Mass Trans. **25**, 1023–1030 (1982).

Chang, L.S. and J.C. Berg, "Fluid Flow and Transfer Behaviour of a Drop Translating in an Electric Field at Intermediate Reynolds Numbers", Int. J. Heat Mass Transfer **26**, 823–832 (1983).

Chang, L.S. and J.C. Berg, "Electroconvective Enhancement of Mass or Heat Exchange Between a Drop or Bubble and Surroundings in the Presence of an Interfacial Tension Gradient", AIChE J. **31**, 149-151 (1985a).

Chang, L.S. and J.C. Berg, "The Effect of Interfacial Tension Gradients on the Flow Structure of Single Drops or Bubbles Translating in an Electric Field", AIChE J. **31**, 551-557 (1985b).

Chazal, L.E.M. and J.T. Ryan, "Formation of Organic Drops in Water", AIChE J. **17**, 1226-1229 (1971).

Chu, B.T., "Thermodynamics of Electrically Conducting Fluids", Phys. Fluids, **2**, 473-484 (1959).

Clift, R., J.R. Grace and M.E. Weber, "Bubbles, Drops, and Particles", Academic Press, New York (1978).

Cross, J.A., "Electrostatics: Principles, Problems and Applications", Adam Hilger, Bristol (1987).

Crowley, J.M., "Fundamentals of Applied Electrostatics", John Wiley & Sons, New York (1986).

Davidson, J.F. and B.O.G. Schüler, "Bubble Formation at an Orifice in a Viscous Liquid", Trans. Instn. Chem. Engrs. **38**, 144-154 (1960).

Davies, J.T., "Turbulence Phenomena", Academic Press, New York (1972).

Eringen, A. C. and G.A. Maugin, "Electrodynamics of Continua, (Vol. I, II)", Springer-Verlag, New York (1990).

Freeman, R.W. and J. Laurizio, "Mass Transfer from A Forming and Falling Drop under The Influence of An Applied Electric Field", in Chemical Separations (C.J. King and J.D. Navratil Eds.), 295-301, Litarvan, Denver (1986).

Gao, K.C., "Some Electromechanical Effects on Dielectrics", Brit. J. Appl. Phys. **12**, 629–632 (1961).

Garton, C.G. and Z. Krasucki, "Bubbles in Insulating Liquids: Stability in an Electric Field", Proc. Roy. Soc. Lond. **A280**, 211–226 (1964).

Griffiths, S.K. and Morrison, F.A., "Low Peclet Number Heat and Mass Transfer from a Drop in an Electric Field", J. Heat Transfer **101**, 484–488 (1979).

Hadamard, J.S., "Movement Permanent lent d'une Sphere Liquide et Visqueuse dans un Liquide Visqueux", Compt. Rend. Acad. Sci. **152**, 1735–1738 (1911).

Hamielec, A.E. and A.I. Johnson, "Viscous Flow Around Fluid Spheres at Intermediate Reynolds Numbers", Can. J. Chem. Eng. **40**, 41–45 (1962).

Hamielec, A.E., S.H. Storey and J.M. Whitehead, "Viscous Flow Around Fluid Spheres at Intermediate Reynolds Numbers (II)", Can. J. Chem. Eng. **41**, 246–251 (1963).

Hamielec, A.E., T.W. Hoffman and L.L. Ross, "Numerical Solution of the Navier-Stokes Equation for Flow Past Spheres: Part I. Viscous Flow Around Spheres with and without Radial Mass Efflux", A.I.Ch.E. J. **13**, 212–219 (1967).

Hamielec, A.E., A.I. Johnson and W.T. Houghton, "Numerical Solution of the Navier-Stokes Equation for Flow Past Spheres: Part II. Viscous Flow Around Circulating Spheres of Low Viscosity", A.I.Ch.E. J. **13**, 220–224 (1967).

Happel, J. and H. Brenner, "Low Reynolds Number Hydrodynamics", 2nd. ed., Noordhoff. Intern. Publ., Netherlands (1973).

Harker, J.H. and J. Ahmadzadeh, "The Effect of Electric Fields on Mass Transfer from Falling Drops", Int. J. Heat Mass Transfer **17**, 1219–1224 (1974).

Harkins, W.D. and F.E. Brown, "The Determination of Surface Tension (Free Surface Energy), and the Weight of Falling Drops: The Surface Tension of Water and Benzene by the Capillary Height Method", J. Am. Chem. Soc. **41**, 499–524 (1919).

Hayworth, C.B. and R.E. Treybal, "Drop Formation in Two-Liquid-Phase Systems", Ind. Eng. Chem. **42**, 1174–1181 (1950).

He, W., M.H.I. Baird and J.S. Chang, "The Effect of Electric Field on Droplet Formation and Motion in a Viscous Liquid", Can. J. Chem. Eng. **69**, 1174–1183 (1991).

He, W., M.H.I. Baird and J.S. Chang, "The Effect of Electric Field on Mass Transfer from Drops Dispersed in a Viscous Liquid", Can. J. Chem. Eng. **71**, 366–376 (1993).

He, W. and J.S Chang, "Chapter 22: EHD Enhanced Mass Transfer Operations and Chemical Reactions" in Handbook of Electrostatic Applications, (J.S. Chang, A.J. Kelly and J.M. Crowley eds), Marcel Dekker, Inc., New York (1993, in press).

Heertjes, P.M., W.A. Holve and H. Talsma, "Mass Transfer between Isobutanol and Water in a Spray-Column", Chem. Eng. Sci. **3**, 122–142 (1954).

Hendricks, C.D., "Charged Droplet Experiments", J. Colloid Sci. **17**, 249–259 (1962).

Higbie, R., "The Role of Absorption of a Pure Gas into a Still Liquid during Short Period of Exposure", Trans. Am. Inst. Engrs. **31**, 365–389 (1935).

Hu, S. and R.C. Kintner, "The Fall of Single Liquid Drops through Water", AIChE J. **1**, 42–48 (1955).

Hughes, W.F. and F.J. Young, "Electromagnetodynamics of Fluids", John Wiley & Sons, New York (1966).

Hund, M. and F. Lancelot, "Interfacial Transfer Under Electrostatic Field in Solvent Extraction", Proc. Intl. Solvent Extn. Conf. **ISEC'86**, Dechema, Frankfurt, FRG, pp. I-510-517 (1986).

Iyer, P.V.R. and H. Sawistowski, "Effect of Electric Field on Mass Transfer Across a Plane Interface", Proc. **ISEC'74**, 1029-1046 (1974).

Johnson, A.I. and A.E. Hamielec, "Mass Transfer Inside Drops", A.I.Ch.E. J. **6**, 145-149 (1960).

Kitahara, A., "Chapter 5: Nonaqueous Systems" in Electrical Phenomena at Interfaces, (A. Kitahara and A. Watanabe eds.) Marcel Dekker, Inc. New York (1984)

Kowalski, W and Z. Ziolkowski, "Increase in Rate of Mass Transfer in Extraction Columns by Means of An Electric Field", Int. Chem. Eng. **21**, 323-327 (1981).

Kumar, R. and N.R. Kuloor, "The Formation of Bubbles and Drops", Adv. Chem. Eng. **8**, 256-368 (1970).

Lam, S.H., "A General Theory for the Flow of Weakly Ionized Gases", AIAA J. **2**, 256-262 (1964).

Landau, L.D. and E.M. Lifshitz, Electrodynamics of Continuous Media, Pergamon Press, London (1960).

Levich, V.G., "Physicochemical Hydrodynamics", Prentice-Hall, New York (1962).

Licht, W. and W.F. Pansing, "Solute Transfer from Single Drops in Liquid-liquid Extraction", Ind. Eng. Chem. **45**, 1885-1896 (1953).

Lo, T.C. and M.H.I. Baird, "Extraction, Liquid-Liquid", in Kirk-Othmer: Encyclopedia of Chemical Technology, 3rd ed., **9**, 672–721, John Wiley & Sons, New York , N.Y. (1980).

Lo, T.C., M.H.I. Baird and C. Hanson (Eds.), "Handbook of Solvent Extraction", John Wiley & Sons, New York, N.Y. (1983).

Masuda, S., K. Fujibayashi and H. Inaba, "Confinement and Transportation of Charged Aerosol Clouds via Electric Curtain", Elec. Eng. Japan **92**, 43–52 (1972).

Martin, L., P. Vignet, C. Fombawlet and F. Lancelot, "Electrical Field Contactor for Solvent Extraction", Sep. Sci. & Tech. **18**, 1455–1471 (1983).

Maxwell, J.C. "A Treatise on Electricity and Magnetism", (2nd Vol., 3rd edn.), Oxford University Press, Oxford (1892).

Melcher, J.R. and G.I. Taylor, "Electrohydrodynamics: a Review of the Role of Interfacial Shear Stresses", Ann. Rev. Fluid Mech., **1**, 111–146 (1969).

Melcher, J.R., "Continuum Electromechanics", MIT Press, Cambridge (1981).

Millar, M.K. and L.R. Weatherley, "Whole Broth Extraction in An Electrically Enhanced Liquid-liquid Contact System", Chem. Eng. Res. Des. **67**, 227–231 (1989).

Minkowycz, W.J., E.M. Sparrow, G.E. Schneider, and R.H. Pletcher, "Handbook of Numerical Heat Transfer", Wiley, New York (1988).

Moon, P. and D.E. Spencer, "Field Theory for Engineers", Ch. 9, D. Van Nostrand Company, Inc. Princeton, N.J. (1961).

Moore, A.D. (ed.), "Electrostatics and Its Applications", John Wiley & Sons, New York (1973).

Morrison, F.A., "Transient Heat and Mass Transfer to a Drop in an Electric Field", J. Heat Transfer **99**, 269-273 (1977).

Ogata. S., T. Kawashima, O.Nakaya and H. Shinohara, "Stability of Charged Drop Issuing from Fine Capillary", J. Chem. Eng. Japan **9**, 440-444 (1976).

Ogata. S. and H. Shinohara, "Specific Charge and Size of Droplets Electrohydrodynamically Produced", Memoirs of the Faculty of Engineering, Kyushu University **38**, 143-152 (1978).

Ogata, S., K. Tan, K. Nishijima and J.S. Chang, "Development of Improved Bubble Disruption and Dispersion Technique by an Applied Electric Field Method", AIChE J. **31**, 62-69 (1985).

Patankar, S.V., "Numerical Heat Transfer and Fluid Flow", McGraw-Hill, New York (1980).

Pfeifer, R.J. and C.D. Hendricks, "Charge-to-Mass Relationships for Electrohydrodynamically Sprayed Liquid Drops", Phys. Fluid **10**, 2149-2154 (1967).

Pohl, H.A., "Dielectrophoresis, Chapter 14 Nonuniform Field Effects:", in Electrostatics And Its Applications, (A. D. Moore, ed.), John Wiley & Sons, New York, (1973).

Popovich, A.T., R.E. Jervis and O. Trass, "Mass Transfer during Single Drop Formation", Chem. Eng. Sci. **19**, 357-365 (1964).

Ptasinski, K.J. and P.J.A.M. Kerkhof, "Electric Field Driven Separations: Phenomena and Applications", Sep. Sci. and Tech. **27**, 995-1021 (1992).

Ranz, W.E. and W.R. Marshall, "Evaporation from Drops, Part I & Part II", Chem. Eng. Prog. **48**, 141-146, 173-180 (1952).

Rao, E.V.L.N., R. Kumar and N.R. Kuloor, "Drop Formation Studies in Liquid-Liquid Systems", Chem. Eng. Sci. **21**, 867-880 (1966).

Raithby, and Schneider, "Chapter 5" in Handbook of Numerical Heat Transfer, (Minkowycz, W.J., E.M. Sparrow, G.E. Schneider, and R.H. Pletcher eds.) Wiley, New York (1988).

Ritcey, G.M. and A.W. Ashbrook, "Solvent Extraction—Principles and Applications to Process Metallurgy, Part II", Elsevier, Amsterdam (1979).

Rayleigh, J.W.S., "On the Equilibrium of Liquid Conducting Masses Charged with Electricity", Phil. Mag. (Ser. 5)**14**, 184-186 (1882).

Rosensweig, R.E., "Magnetic Stabilization of the State of Uniform Fluidization", Ind. Eng. Chem. Fundam. **18**, 260-268 (1979).

Roth, and A.J. Kelly, "Analysis of Disruption of Electrostatically Charged Droplets", IEEE Trans. Ind. Appl. **IA-19**, 771-775 (1983)

Rybczynski, W., "Translatory Motion of a Fluid Sphere in a Viscous Medium", Bull. Int. Acad. Pol. Sci. Lett., Cl. Sci. Math. Nat., **Ser. A**, 40-46 (1911).

Sato, M. and Sakai, T., "Reduction of Liquid Surface Tension under Electrostatic Fields", Kagaku Kogaku Ronbunshu **2**, 317-319 (1976).

Scaife, B.K.P., Principles of Dielectrics, Oxford Press, New york (1989).

Scheele, G.F. and B.J. Meister, "Drop Formation at Low Velocities in Liquid-Liquid Systems", AIChE J. **14**, 9-15 (1968).

Scott, T.C. "Surface Area Generation and Droplet Size Control Using Pulsed Electric Fields", AIChE J. **33** 1557-1559 (1987).

Scott, T.C. and W.G. Sisson, "Droplet Size Characteristics and Energy Input Requirements of Emulsions Formed Using High-Intensity-Pulsed Electric Fields", Sepr. Sci. and Tech. **23** 1541–1550 (1988).

Scott, T.C. "Use of Electric Fields in Solvent Extraction: a Review and Prospects", Sepn. and Purif. **18**, 65–109 (1989).

Scott, T.C. and Byers, C.H., "A Model for Mass Transfer in Oscillating-Circulating Liquid Drops", Chem. Eng. Commun. **77**, 67–89 (1989).

Scott, T.C., Basaran, O.A. and Byers, C.H., "Characteristics of Electric-Field-Induced Oscillations of Translating Liquid Droplets", Ind. Eng. Chem. Res. **29**, 901–909 (1990).

Skelland, A.H.P. and S.S. Minhas, "Dispersed Phase Mass Transfer during Drop Formation and Coalescence in Liquid-Liquid Extraction", AIChE J. **17**, 1316–1324 (1971).

Slater, M.J., M.H.I. Baird and T.-B. Liang, " Drop Phase Mass Transfer Coefficients for Liquid-liquid Systems and The Influence of Packings", Chem. Eng. Sci. **43**, 233–245 (1988).

Stewart, G. and J.D. Thornton, "Charge and Velocity Characteristics of Electrically Charged Droplets, Part I: Theoretical Considerations", "Part II: Preliminary Measurements of Droplet Charge and velocity", Symp. Sers. **No. 26**, Instn. Chem. Engrs., 29-42 (1967).

Stokes, G.G., "On the Effect of the Internal Friction of Fluids on the Motion of Pendulums", Trans. Cambridge Phil. Soc. **9**, 8–27 (1851).

Streicher, R. and K. Schügerl, "Interchange of Fluid Mechanics and Mass Exchange in Droplets", Chem. Eng. Sci. **32**, 23–33 (1977).

Taylor, G. I., "Disintegration of Water Drops in An Electric Field", Proc. Roy. Soc. Lond. **280A**, 383-397 (1964).

Taylor, G.I., "Studies in Electrohydrodynamics I. The Circulation Produced in a Drop by an Electric Field", Proc. Roy. Soc. Lond. **291A**, 159-166 (1966).

Takamatsu, T., Y. Hashimoto, M. Yamaghchi and T. Katayama, "Theoretical and Experimental Studies of Charged Drop Formation in A Uniform Electric Field", J. Chem Eng Japan **14**, 178-182 (1981).

Takamatsu, T., M. Yamaghchi and T. Katayama, "Formation of Single Charged Drops in Liquid Media under a Uniform Electric Field", J. Chem Eng Japan **15** 349-355 (1982).

Takamatsu, T., M. Yamaghchi and T. Katayama, "Formation of Single Charged Drops in a Non-Uniform Electric Field", J. Chem Eng Japan **16** 267-272 (1983a).

Takamatsu, T., M. Yamaguchi, and T. Katayama, "Terminal Velocity of Single Charged Drops Through Dielectric Liquid in a Uniform Electric Field", J. Chem. Eng. Japan **16**, 324-326 (1983b).

Thornton, J.D. "The Application of Electrical Energy to Chemical and Physical Rate Processes", Rev. Pure and Appl. Chem. **18**, 197-218 (1968).

Thornton, J.D. "Electrically Enhanced Liquid-liquid Extraction", Birmingham University Chem. Engr. **27**, 6-13 (1976).

Treybal, R.E., "Mass Transfer Operations", Third ed., McGraw-Hill, New York (1980).

Tsukada, T., M. Sato, N. Imaishi, M. Hozawa and K. Fujinawa, "A Theoretical and Experimental Study on the Oscillation of a Hanging Drop", J. Chem. Eng. Japan **20** 88-93 (1987).

Vonnegut, B. and R.L. Neubauer, "Production of Monodisperse Liquid Particles by Electrical Atomization", J. Colloid Sci. **7**, 616-622 (1952).

Vu, N. and Carleson, T.E., "Electric Field Effects on Drop Size and Terminal Velocity in Liquid-liquid Systems", AIChE J. **32**, 1739-1742 (1986).

Waterman, L. C., "Electrical Coalescers", Chem. Eng. Prog. **61**, 51-57 (1965).

Weatherley, L.R., I. Campbell, D. Kirton and J.C. Slaughter, "Electrically Enhanced Extraction of Penicillin G into Dichloromethane", J. Chem. Tech. Biotech. **48**, 427-438 (1990).

Weatherley, L.R. "Electrically Enhanced Extraction", Section 5.6 in Chapter 5: Development and Extraction Techniques, Science and Practice of Liquid-Liquid Extraction (Vol. 2), (J.D. Thornton Ed.) 407-419, Oxford, U.K. (1992).

Wham, R.M. and C.H. Byers, "Mass Transport from Single Droplets in Imposed Electric Fields", Sepn. Sci. and Tech. **22**, 447-466 (1987).

Wilke, C.R. and P.C. Chang, "Correlation of Diffusion Coefficients in Dilute Solutions", AIChE J. **1**, 264-270 (1955).

Yamaguchi, M. and T. Katayama, "Drag Coefficients and Mass Transfer in the Continuous Phase for Single Drops at Low Reynolds Numbers", J. Chem. Eng. Japan **7**, 334-341 (1974).

Yamaguchi, M., T. Takamatsu, F. Yoshida and T. Katayama, "An Experimental Study of Mass Transfer Rate in The Dispersed Phase for Single Charged Drops in a Dielectric Liquid under a Uniform Electric Field", J. Chem. Eng. Japan **18**, 325-330 (1985).

Yamaguchi, M., H. Sugaya and T. Katayama, "Liquid-liquid Extraction Characteristics of A Spray Column with A D.C. Electric Field", Proc. Intl. Solvent Extn. Conf. **ISEC'88**, Moscow, pp. 210-213 (1988).

Yamaguchi, M., H. Sugaya and T. Katayama, "Liquid-liquid Extraction Characteristics of A Spray Column with A D.C. Electric Field", J. Chem. Eng. Japan **22**, 25-29 (1989).

Yang, W. and T.E. Carleson, "Several Effects of Electric Fields on Liquid Extraction", IEEE Trans. Ind. Appl. **26**, 366-373 (1990).

Yang, W. and T.E. Carleson, "Linear Oscillations of a Drop in Uniform Alternating Electric Fields", AIChE J. **37**, 1601-1606 (1991).

Yoshida, F., M. Yamaguchi and T. Katayama, "An Experimental Study of Electrohydrodynamic Dispersion from a Liquid Film Flowing down an Inclined Plate into a continuous Liquid Phase", J. Chem. Eng. Japan, **19**, 1-7 (1986).

Yoshida, F., M. Yamaguchi and T. Katayama, "Characteristics of Electrical Dispersion from Water Film Flowing down an Inclined Plate into a Dielectric Liquid Phase: Drop Diameter, Drop Velocity and Dispersed-Phase Holdup", J. Chem. Eng. Japan, **21**, 123-129 (1988).

# Appendix A

# Derived Equations from Coordinates Transformations

The derivations for the transformed partial derivatives as well as the inverse functions for both coordinates are presented in the following sections. These equations are used in the transformations to the governing Laplace's equation and boundary conditions of Equations (4.1)-(4.11).

## A.1 Transformations of Partial Derivatives

The Laplace's Equation (4.1) can be expanded as follows

$$\nabla^2\phi = \frac{\partial^2\phi}{\partial r^2} + \frac{1}{r}\frac{\partial\phi}{\partial r} + \frac{\partial^2\phi}{\partial z^2} = 0 \tag{A.1}$$

The transformations for $r$ and $z$ can be expressed as:

$$\phi = f(\bar{r},\bar{z}), \quad \bar{r} = f_1(r), \quad \bar{z} = f_2(z) \tag{A.2}$$

Then, the following derivatives can be obtained:

$$\frac{\partial\phi}{\partial r} = \frac{\partial\phi}{\partial\bar{r}}\frac{\partial\bar{r}}{\partial r} \tag{A.3}$$

$$\frac{\partial^2\phi}{\partial r^2} = \frac{\partial\phi}{\partial\bar{r}}\frac{\partial^2\bar{r}}{\partial r^2} + \frac{\partial^2\phi}{\partial\bar{r}^2}(\frac{\partial\bar{r}}{\partial r})^2 \tag{A.4}$$

$$\frac{\partial^2\phi}{\partial z^2} = \frac{\partial\phi}{\partial\bar{z}}\frac{\partial^2\bar{z}}{\partial z^2} + \frac{\partial^2\phi}{\partial\bar{z}^2}(\frac{\partial\bar{z}}{\partial z})^2 \tag{A.5}$$

where the transformation for the derivatives of $\frac{\partial\bar{r}}{\partial r}$, $\frac{\partial^2\bar{r}}{\partial r^2}$, $\frac{\partial\bar{z}}{\partial z}$ and $\frac{\partial^2\bar{z}}{\partial z^2}$ can be derived from Equations (4.15)-(4.17) respectively as follows:

$$\frac{\partial\bar{r}}{\partial r} = \frac{2\beta}{r_1\{\beta^2 - [1-(r/r_1)]^2\}\ln[(\beta+1)/(\beta-1)]} \tag{A.6}$$

$$\frac{\partial^2\bar{r}}{\partial r^2} = -\frac{4\beta[1-(r/r_1)]}{r_1^2\ln[(\beta+1)/(\beta-1)]\{\beta^2 - [1-(r/r_1)]^2\}^2} \tag{A.7}$$

$$\frac{\partial\bar{z}}{\partial z} = \frac{\sinh(\tau B)}{\tau L_2\{1+[(z/L_2)-1]^2\sinh^2(\tau B)\}^{0.5}} \tag{A.8}$$

$$\frac{\partial^2\bar{z}}{\partial z^2} = -\frac{\sinh^3(\tau B)[(z/L_2)-1]}{\tau L_2^2\{1+[(z/L_2)-1]^2\sinh^2(\tau B)\}^{\frac{3}{2}}} \tag{A.9}$$

## A.2 Inverse Transformations for $r$ and $z$

The inverses transformations for $r$ and $z$ from Equations (4.15)-(4.17) can be derived respectively as follows:

$$r = r_1\{\frac{(\beta+1)-(\beta-1)[(\beta+1)/(\beta-1)]^{1-\bar{r}}}{[(\beta+1)/(\beta-1)]^{1-\bar{r}}+1}\} \tag{A.10}$$

$$z = L_2\{1+\frac{\sinh[\tau(\bar{z}-B)]}{\sinh(\tau B)}\} \tag{A.11}$$

# Appendix B

# Analytical Solutions of Electric Field Near Hollow Electrode

## B.1 Ellipsoidal Coordinates

Ellipsoidal, or prolate spheroidal, Coordinates $(\eta, \theta, \Psi)$ are generated by rotating ellipses about their major axis. The relation between the ellipsoidal and Cartesian coordinates are given by the following equations (Moon and Spencer, 1961):

$$x = a \sinh \eta \sin \theta \cos \Psi \tag{B.1}$$

$$y = a \sinh \eta \sin \theta \sin \Psi \tag{B.2}$$

$$z = a \cosh \eta \cos \theta \tag{B.3}$$

The surfaces of constant $\eta$ are prolate spheroids:

$$\frac{x^2}{b^2} + \frac{y^2}{b^2} + \frac{z^2}{c^2} = 1 \tag{B.4}$$

which is the equation of an ellipsoid with semi-axes: $b = a \sinh \eta$ and $c = a \cosh \eta$.

Laplace's equation in prolate spheroidal coordinates with two-dimensional geometry $(\eta, \theta)$ can be obtained as:

$$\frac{1}{a^2(\sinh^2\eta + \sin^2\theta)}\{\frac{\partial^2\phi}{\partial\eta^2} + \coth\eta\frac{\partial\phi}{\partial\eta} + \frac{\partial^2\phi}{\partial\theta^2} + \cot\theta\frac{\partial\phi}{\partial\theta}\} = 0 \tag{B.5}$$

## B.2 Electric Field along the Hollow Electrode Axis

Suppose an isolated metal spheroid as shown in Figure B.1, where $\eta = \eta_0$ is at potential $V_0$. Then the boundary conditions are specified as:

$$\eta = \eta_0, \quad \phi = V_0 \tag{B.6}$$

and

$$\eta \to \infty, \quad \phi = 0 \tag{B.7}$$

The solution of Laplace's equation with the above boundary conditions is a function of $\eta$ only ($\theta = 0$ along the axis) and can be expressed as follows (Moon and Spencer, 1961):

$$(\frac{\phi}{V_0}) = \frac{\ln\coth(\eta/2)}{\ln\coth(\eta_0/2)} \tag{B.8}$$

The electric field strength along $z$ axis is obtained from Equation (B.3):

$$\mathbf{E} = (\frac{V_0}{a})\frac{1}{\ln\coth(\eta_0/2)\sinh^2\eta} \tag{B.9}$$

and its dimensionless form is expressed as:

$$(\frac{\mathbf{E}}{\mathbf{E}_0}) = \frac{\sinh^2\eta_0}{\sinh^2\eta} \tag{B.10}$$

The hollow electrode used in this work, where DC voltage applied at potential $V_0$, is considered as the metal spheroid with the following two different assumptions being made:

$$\begin{cases} \eta = \eta_0, & \phi = V; \\ \eta \to \infty, & \phi = 0. \end{cases}$$

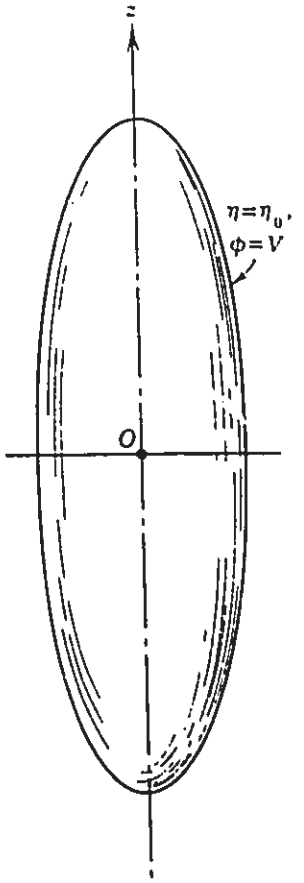


Figure B.1: Schematic diagram of a metal spheroid

- **model 1** assumes that the length of the hollow electrode is equivalent to the total length of the metal spheroid as schematically illustrated in Figure B.2a, and the following approximate expressions can be obtained from Moon and Spencer (1961):

$$l \approx 2a, \quad \text{and} \quad b = a \sinh \eta_0 \approx a\eta_0 \quad (\text{for } b \ll a) \tag{B.11}$$

The $z$ distance along the hollow electrode axis is

$$z = a(1 + \cosh \eta) \approx \frac{l}{2}(1 + \cosh \eta) \tag{B.12}$$

- **model 2** assumes that the length of the hollow electrode is equivalent to the half length of the metal spheroid as schematically illustrated in Figure B.2b, and the following approximate expressions can be obtained from Moon and Spencer (1961):

$$l \approx a, \quad \text{and} \quad b = a \sinh \eta_0 \approx a\eta_0 \quad (\text{for } b \ll a) \tag{B.13}$$

The $z$ distance along the hollow electrode axis is

$$z = a \cosh \eta \approx l \cosh \eta \tag{B.14}$$

It is noted that both analytical solutions derived above are only accurate at the region near the hollow electrode due to the constraint of the second boundary condition. The analytical solutions also break down at very close to the hollow electrode due to actual cylindrical nature of the electrode geometry.

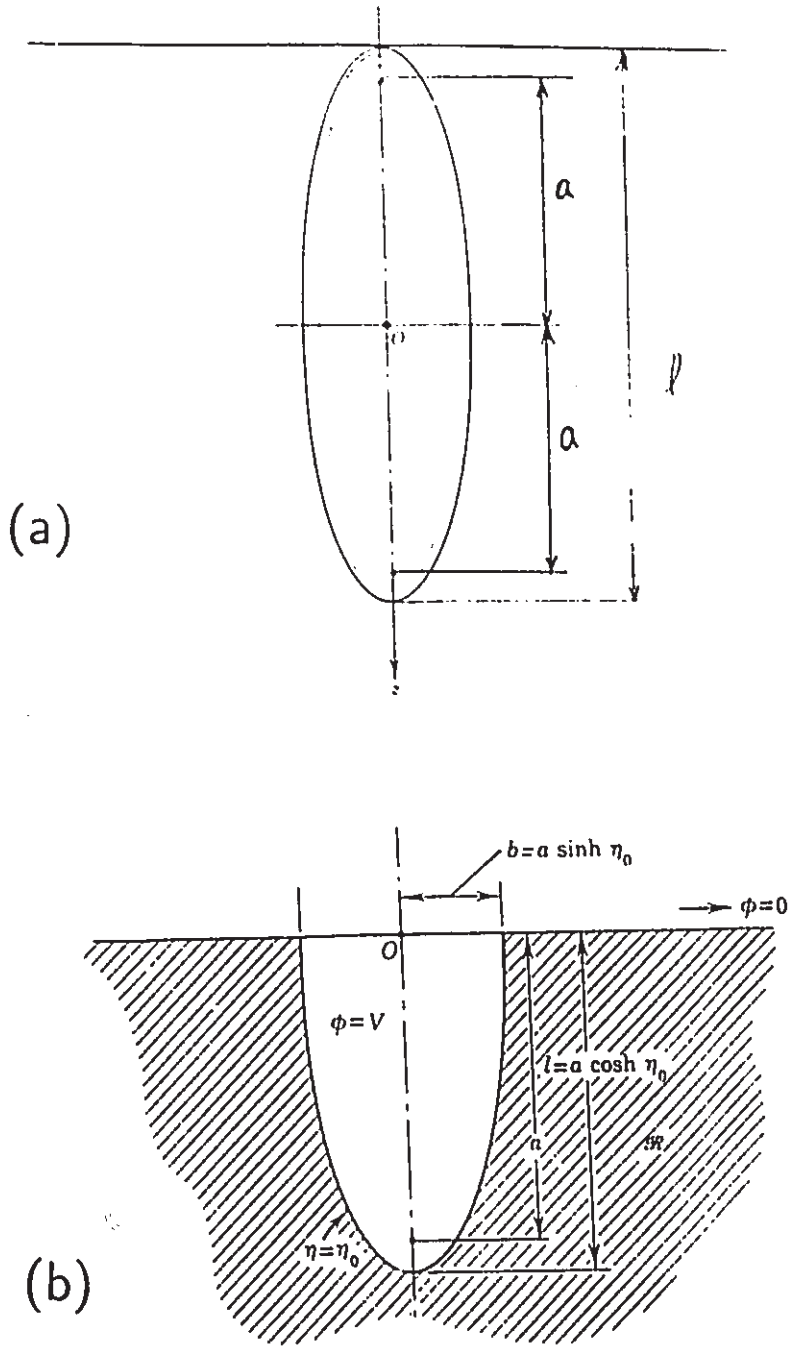


Figure B.2: Schematic diagram of analytical models: (a) model 1; (b) model 2

# Appendix C

# Numerical Modelling Program

```
************************************************************
*                                                          *
*          NUMERICAL MODELLING OF THE ELECTRIC FIELD       *
*                                                          *
*        - POTENTIAL, FIELD AND GRADIENT OF FIELD SQUARE   *
*                                                          *
*                  (AXIAL SYMMETRIC GEOMETRY)              *
*                                                          *
************************************************************
      IMPLICIT DOUBLE PRECISION (A-Z)
      DIMENSION A(50), B(50), C(50), D(50), VP(50), RBAR(50),
     *  ZBAR(50), VS(21,41), V(21,41),ER(21,41),EZ(21,41),
     *  EE2(21,41),EE(21,41),DE2R(21,41),DE2Z(21,41), DE2(21,41)
      INTEGER I, J, M, N
************************************************************
*                                                          *
*  RBAR - RADIAL COORDINATES                               *
*  ZBAR - AXIAL COORDINATES                                *
*  V    - ITERATION VALUES IN RADIAL DIRECTION             *
*  VS   - ITERATION VALUES IN AXIAL DIRECTION              *
*  ER   - FIELD COMPONENT IN RADIAL DIRECTION              *
*  EZ   - FIELD COMPONENT IN AXIAL DIRECTION               *
*  EE2  - FIELD SQUARE                                     *
*  EE   - MAGNITUDE OF THE FIELD                           *
*  DE2R - GRADIENT OF FIELD SQUARE IN RADIAL DIRECTION     *
*  DE2Z - GRADIENT OF FIELD SQUARE IN RADIAL DIRECTION     *
*  DE2  - MAGNITUDE OF GRADIENT OF FIELD                   *
*  N    - NUMBER OF GRIDS IN RADIAL DIRECTION              *
*  M    - NUMBER OF GRIDS IN AXIAL DIRECTION               *
************************************************************
C
C.....INPUT AND CHECK THE PARAMETERS.....
C
      PRINT *, 'INPUT ptao, M, N, NO, L1, L2, R1, RR'
      READ *, ptao, M, N, NO, L1, L2, R1, RR'
C
      DR=1.0/(N-1.0)
      DZ=1.0/(M-1.0)
      C1=DR/DZ
```

```
      C2=1.0/C1
      C3=0.5*DR
      C4=0.5*DZ
      PBATA=1.01
      PTAO=10.0
C
      FA1=PBATA+1
      FA2=PBATA-1
      FA3=FA1/FA2
      FA4=ALOG(FA3)
C
      PB1=EXP(PTAO)-1.0
      PB2=EXP(-PTAO)-1.0
      PB3=L2/L1
      PB4=ALOG((1+PB1*PB3)/(1+PB2*PB3))
      PB=0.5*PB4/PTAO
C
C.....INPUT BOUNDARY CONDITIONS.....
C
      V0=15
      RBAR(1)=0.0
      ZBAR(1)=0.0
C
      DO 15 I=2,N
         RBAR(I)=RBAR(I-1)+DR
 15   CONTINUE
C
      R1BAR=RBAR(N)
      R2BAR=RBAR(3)
C
      DO 16 J=2, M
         ZBAR(J)=ZBAR(J-1)+DZ
 16   CONTINUE
C
      L1BAR=ZBAR(M)
      L2BAR=ZBAR(N0)
C
      WRITE (*,200) M,N,DR,DZ,RR,R1,L1,L2,
     *      R1BAR,R2BAR,L1BAR,L2BAR
C
      DO 5 I=1,N
         DO 10 J=1,M
            VS(I,J)=0.0
            V(I,J)=0.0
  10     CONTINUE
  5   CONTINUE
C
      DO 11 I=1,3
      DO 12 J=1,N0
         VS(I,J)=V0
         V(I,J)=V0
  12  CONTINUE
  11  CONTINUE
C
C
C.....CALCULATE VOLTAGES ALONG R DIRECTION.....
      ICOUNT=0
  20  ICOUNT=ICOUNT+1
C
      SUM2=SUM1
      SUM1=0.0
```

```
      DSUM=0.0
C
       DO 25 J=2, NO
C
          CALL COFER(A,B,C,D,R1,L2,RBAR,ZBAR,N,C1,C2,C3,C4,VS,
     *               PTAO,PBATA,PB,FA1,FA2,FA3,FA4,I,J,I1,J1,
     *               I2,J2,DR,DZ)
           CALL TRIDAG(4,N-1,A,B,C,D,VP)
            DO 28 I=4,N-1
               V(I,J)=VP(I)
  28        CONTINUE
  25    CONTINUE
           DO 30 J=(NO+1),M-1
            CALL COFER(A,B,C,D,R1,L2,RBAR,ZBAR,N,C1,C2,C3,C4,VS,
     *             PTAO,PBATA,PB,FA1,FA2,FA3,FA4,I,J,I1,J1,
     *             I2,J2,DR,DZ)
            CALL TRIDAG(2,N-1,A,B,C,D,VP)
C
            DO 29 I=2,N-1
               V(I,J)=VP(I)
C
  29        CONTINUE
  30    CONTINUE
C
C
C.....CALCULATE VOLTAGES ALONG Z DIRECTION.....
       DO 35 I=2,N-1
C
            CALL COFEZ(A,B,C,D,R1,L2,RBAR,ZBAR,M,C1,C2,C3,C4,V,
     *             PTAO,PBATA,PB,FA1,FA2,FA3,FA4,I,J,I1,J1,
     *             I2,J2,DR,DZ)
            IF (I.LE.3)THEN
              CALL TRIDAG (NO+1,M-1,A,B,C,D,VP)
              DO 32 J=(NO+1),M-1
                 VS(I,J)=VP(J)
  32          CONTINUE
            ELSE
              CALL TRIDAG(2,M-1,A,B,C,D,VP)
              DO 40 J=2,M-1
                VS(I,J)=VP(J)
C
  40          CONTINUE
            ENDIF
C
  35    CONTINUE
C
C.....PRINT VOLTAGES THROUGHOUT THE DOMAIN.....
C
       DO 41 J=NO+1, M-1
          SUM1=SUM1+V(2,J)+V(3,J)
  41      CONTINUE
       DO 42 I=4,N-1
           DO 43 J=2,M-1
           SUM1=SUM1+V(I,J)
  43      CONTINUE
  42   CONTINUE
C
        DSUM=ABS(SUM1-SUM2)
        IF (DSUM-RR) 45,45,20
  45   DO 50 J=NO+1,M-1
       V(1,J)=V(2,J)+(V(2,J)-V(3,J))/3
```

```
  50  CONTINUE
C
C.....CALCULATE FIELD AND FIELD SQUARE  ....................
C
         RI=RBAR(N)
         CALL FUNDR(DRI,RI,R1,PBATA,FA1,FA2,FA3,FA4)
C
      DO 75 J=1,M
         ER(1,J)=0.0
         ER(N,J)=-(1.5*V(N,J)-2.0*V(N-1,J)+0.5*V(N-2,J))/DR*DRI
  75  CONTINUE
       DO 80 J=1,M
         DO 85 I=2,N-1
            RI=RBAR(I)
            CALL FUNDR(DRI,RI,R1,PBATA,FA1,FA2,FA3,FA4)
            ER(I,J)=-(V(I+1,J)-V(I-1,J))/2.0/DR*DRI
  85     CONTINUE
  80  CONTINUE
C
      DO 90 I=1,N
         DO 95 J=2,M-1
            ZJ=ZBAR(J)
            CALL FUNDZ(DZJ,ZJ,L2,PTAO,PB)
            EZ(I,J)=-(V(I,J+1)-V(I,J-1))/2.0/DZ*DZJ
 95       CONTINUE
 90   CONTINUE
C
      DO 97 I=1,N
        ZJ=ZBAR(1)
        CALL FUNDZ(DZJ,ZJ,L2,PTAO,PB)
        EZ(I,1)=-(2.0*V(I,2)-1.5*V(I,1)-0.5*V(I,3))/DZ*DZJ
C
        ZJ=ZBAR(M)
        CALL FUNDZ(DZJ,ZJ,L2,PTAO,PB)
        EZ(I,M)=-(1.5*V(I,M)-2.0*V(I,M-1)+0.5*V(I,M-2))/DZ*DZJ
C
 97   CONTINUE
C
      DO 300 I=1, N
         DO 350 J=1, M
            EE2(I,J)=ER(I,J)*ER(I,J)+EZ(I,J)*EZ(I,J)
            EE(I,J)=SQRT(EE2(I,J))
350       CONTINUE
300   CONTINUE
C
C.....CALCULATE GRADIENT OF FIELD SQUARE  ....................
C
         RI=RBAR(N)
         CALL FUNDR(DRI,RI,R1,PBATA,FA1,FA2,FA3,FA4)
C
       DO 750 J=1,M
         DE2R(1,J)=0.0
         DE2R(N,J)=(1.5*EE2(N,J)-2.0*EE2(N-1,J)+0.5*EE2(N-2,J))/DR*DRI
  750 CONTINUE
       DO 800 J=1,M
         DO 850 I=2,N-1
            RI=RBAR(I)
            CALL FUNDR(DRI,RI,R1,PBATA,FA1,FA2,FA3,FA4)
            DE2R(I,J)=(EE2(I+1,J)-EE2(I-1,J))/2.0/DR*DRI
  850    CONTINUE
  800 CONTINUE
```

```
C
      DO 900 I=1,N
         DO 950 J=2,M-1
            ZJ=ZBAR(J)
            CALL FUNDZ(DZJ,ZJ,L2,PTAO,PB)
            DE2Z(I,J)=(EE2(I,J+1)-EE2(I,J-1))/2.0/DZ*DZJ
  950    CONTINUE
  900 CONTINUE
C
      DO 970 I=1,N
        ZJ=ZBAR(1)
        CALL FUNDZ(DZJ,ZJ,L2,PTAO,PB)
        DE2Z(I,1)=(2.0*EE2(I,2)-1.5*EE2(I,1)-0.5*EE2(I,3))/DZ*DZJ
C
        ZJ=ZBAR(M)
        CALL FUNDZ(DZJ,ZJ,L2,PTAO,PB)
        DE2Z(I,M)=(1.5*EE2(I,M)-2.0*EE2(I,M-1)+0.5*EE2(I,M-2))/DZ*DZJ
C
  970 CONTINUE

C
      OPEN(UNIT=1, FILE='F2VOLT.DAT', STATUS='NEW')
      WRITE (1,200) M,N,DR,DZ,RR,R1,L1,L2,R1BAR,R2BAR,L1BAR,L2BAR
      WRITE (*,*) 'ITREATE NUMBER ICOUNT=', ICOUNT
      WRITE (1,*) 'ITREATE NUMBER ICOUNT=', ICOUNT
      WRITE (1,*) 'TOTAL ICONT V(I,J) = ',SUM1
      WRITE (1,*) 'TOTAL ICONT-1 V(I,J) = ',SUM2
C
      DO 55 I=N,1,-1
         WRITE(*,*) 'I= ',I
         WRITE(1,*) 'I= ',I
         WRITE (*,202) (V(I,J), J=1,M)
         WRITE (1,202) (V(I,J), J=1,M)
   55 CONTINUE
      CLOSE(UNIT=1)
C
      OPEN(UNIT=2, FILE='F2EREZ.DAT', STATUS='NEW')
      WRITE (2,210) M,N,DR,DZ,RR,R1,L1,L2,R1BAR,R2BAR,L1BAR,L2BAR
       DO 65 I=N,1,-1
         WRITE(*,*) 'I= ',I
         WRITE(2,*) 'I= ',I
         WRITE(*,*) 'ER=-DVR'
         WRITE(2,*) 'ER=-DVR'
         WRITE (*,202) (ER(I,J), J=1,M)
         WRITE (2,202) (ER(I,J), J=1,M)
C
         WRITE(*,*) 'EZ=-DVZ'
         WRITE(2,*) 'EZ=-DVZ'
         WRITE(*,202) (EZ(I,J), J=1,M)
         WRITE(2,202) (EZ(I,J), J=1,M)
   65 CONTINUE
      CLOSE(UNIT=2)
C
      OPEN(UNIT=3, FILE='F2FIELD.DAT', STATUS='NEW')
      WRITE (3,220) M,N,DR,DZ,RR,R1,L1,L2,R1BAR,R2BAR,L1BAR,L2BAR
C
      DO 365 I=N,1,-1
         WRITE(*,*) 'I= ',I
         WRITE(3,*) 'I= ',I
         WRITE (*,202) (EE(I,J), J=1,M)
         WRITE (3,202) (EE(I,J), J=1,M)
```

```
365   CONTINUE
      CLOSE(UNIT=3)
C
      OPEN(UNIT=4, FILE='F2DE2.DAT', STATUS='NEW')
      WRITE (4,230) M,N,DR,DZ,RR,R1,L1,L2,R1BAR,R2BAR,L1BAR,L2BAR
      DO 265 I=N,1,-1
C
         WRITE(4,*) 'I= ',I
         WRITE(4,*) 'DE2R='
         WRITE (4,202) (DE2R(I,J), J=1,M)
         WRITE (4,*) 'DE2Z='
         WRITE (4,202) (DE2Z(I,J), J=1,M)
265   CONTINUE
      CLOSE(UNIT=4)
C
C
C.....FORMAT FOR INPUT AND OUTPUT STATEMENT........
C
200    FORMAT (10X,'NUMERICAL SIMULATION OF ELECTRIC FIELD -
     * HIGH VOLTAGE POTENTIAL'/15X 'M= ',I5/15X 'N= ',I5/
     * 15X 'DR=', F10.3/15X 'DZ=', F10.3/15X  'RR=', F10.6/
     * 15X 'R1=', F10.2/15X 'L1=', F10.2/
     * 15X 'L2=', F5.2/15X 'R1BAR=', F5.2/15X 'R2BAR=', F5.2/
     * 15X 'L1BAR=', F5.2/15X 'L2BAR=', F5.2)
C
202    FORMAT (3X, 6E12.4)
210    FORMAT (10X,'NUMERICAL SIMULATION OF ELECTRIC FIELD -
     * ELECTROSTATIC FIELD'/15X 'M= ',I5/15X 'N= ',I5/
     * 15X 'DR=', F10.3/15X 'DZ=', F10.3/15X  'RR=', F10.6/
     * 15X 'R1=', F10.2/15X 'L1=', F10.2/
     * 15X 'L2=', F5.2/15X 'R1BAR=', F5.2/15X 'R2BAR=', F5.2/
     * 15X 'L1BAR=', F5.2/15X 'L2BAR=', F5.2)
C
220    FORMAT (10X,'NUMERICAL SIMULATION OF ELECTRIC FIELD -
     * FIELD MAGNITUDE'/15X 'M= ',I5/15X 'N= ',I5/
     * 15X 'DR=', F10.3/15X 'DZ=', F10.3/15X  'RR=', F10.6/
     * 15X 'R1=', F10.2/15X 'L1=', F10.2/
     * 15X 'L2=', F5.2/15X 'R1BAR=', F5.2/15X 'R2BAR=', F5.2/
     * 15X 'L1BAR=', F5.2/15X 'L2BAR=', F5.2)
C
230    FORMAT (10X,'NUMERICAL SIMULATION OF ELETRIC FIELD -
     * GRADIENT FIELD SQUARE'/15X 'M= ',I5/15X 'N= ',I5/
     * 15X 'DR=', F10.3/15X 'DZ=', F10.3/15X  'RR=', F10.6/
     * 15X 'R1=', F10.2/15X 'L1=', F10.2/
     * 15X 'L2=', F5.2/15X 'R1BAR=', F5.2/15X 'R2BAR=', F5.2/
     * 15X 'L1BAR=', F5.2/15X 'L2BAR=', F5.2)
C
       END
C
C
       SUBROUTINE COFER(A,B,C,D,R1,L2,RBAR,ZBAR,N,C1,C2,C3,C4,VX1,
     *   PTAO,PBATA,PB,FA1,FA2,FA3,FA4,I,J,I1,J1,I2,J2,DR,DZ)
       DIMENSION A(50),B(50),C(50),D(50),RBAR(50),
     *      ZBAR(50),VX1(21,41)
       REAL R1,L2,C1,C2,C3,C4,PTAO,PBATA,PB,FA1,FA2,FA3,FA4,
     *    DDN,DDS,FFN,FFS,DDE,DDW,FFE,FFW
       DO 101 I=2,N-1
          I1=I
          J1=J-1
          I2=I
          J2=J+1
```

```
C
      CALL FUNCT(I,J,R1,L2,RBAR,ZBAR,PTAO,PBATA,PB,FA1,FA2,FA3,FA4,
     *     DDN,FFN,DDS,FFS,DDE,FFE,DDW,FFW,C1,C2,C3,C4,DR,DZ)
C
           IF (I.LE.3) THEN
C
           A(I)=DDN+DDE+DDW+FFN+FFS+FFE+FFW
           B(I)=DDN+FFN
           C(I)=FFS
           D(I)=(DDE+FFE)*VX1(I2,J2)+(DDW+FFW)*VX1(I1,J1)
C
           ELSE
C
           A(I)=DDN+DDS+DDE+DDW+FFN+FFS+FFE+FFW
           B(I)=DDN+FFN
           C(I)=DDS+FFS
           D(I)=(DDE+FFE)*VX1(I2,J2)+(DDW+FFW)*VX1(I1,J1)
C
           ENDIF
101    CONTINUE
       RETURN
       END
C
C
      SUBROUTINE COFEZ(A,B,C,D,R1,L2,RBAR,ZBAR,M,C1,C2,C3,C4,
     *       VX2,PTAO,PBATA,PB,FA1,FA2,FA3,FA4,I,J,I1,J1,I2,J2,DR,DZ)
      DIMENSION A(50),B(50),C(50),D(50),RBAR(50),
     *       ZBAR(50),VX2(21,41)
      REAL R1,L2,C1,C2,C3,C4,PTAO,PBATA,PB,FA1,FA2,FA3,FA4,
     *     DDN,DDS,FFN,FFS,DDE,DDW,FFE,FFW
C
      DO 201 J=2,M-1
         I1=I-1
         J1=J
         I2=I+1
         J2=J

      CALL FUNCT(I,J,R1,L2,RBAR,ZBAR,PTAO,PBATA,PB,FA1,FA2,FA3,FA4,
     *           DDN,FFN,DDS,FFS,DDE,FFE,DDW,FFW,C1,C2,C3,C4,DR,DZ)
C
           IF (I.LE.3) THEN
C
           A(J)=DDN+DDE+DDW+FFN+FFS+FFE+FFW
           B(J)=DDE+FFE
           C(J)=DDW+FFW
           D(J)=(DDN+FFN)*VX2(I2,J2)+(FFS)*VX2(I1,J1)
C
           ELSE
C
           A(J)=DDN+DDS+DDE+DDW+FFN+FFS+FFE+FFW
           B(J)=DDE+FFE
           C(J)=DDW+FFW
           D(J)=(DDN+FFN)*VX2(I2,J2)+(DDS+FFS)*VX2(I1,J1)
C
           ENDIF
 201   CONTINUE
       RETURN
       END
C
C
       SUBROUTINE FUNCT(I,J,R1,L2,RBAR,ZBAR,PTAO,PBATA,PB,FA1,
```

```
     * FA2,FA3,FA4,DDN,FFN,DDS,FFS,DDE,FFE,DDW,FFW,C1,C2,C3,C4,DR,DZ)
       DIMENSION RBAR(50),ZBAR(50)
C
       RN=RBAR(I)+C3
       RS=RBAR(I)-C3
       ZE=ZBAR(J)+C4
       ZW=ZBAR(J)-C4
C
       FRN1=FA3**(1.0-RN)
       FRN2=FA2*FRN1
       FRN3=1.0+FRN1
       FRN=R1*(FA1-FRN2)/FRN3
C
       FRS1=FA3**(1.0-RS)
       FRS2=FA2*FRS1
       FRS3=1.0+FRS1
       FRS=R1*(FA1-FRS2)/FRS3
C
       FZE1=PTAO*(ZE-PB)
       FZE2=PTAO*PB
       FZE3=SINH(FZE1)
       FZE4=SINH(FZE2)
       FZE=L2*(1.0+FZE3/FZE4)
C
       FZW1=PTAO*(ZW-PB)
       FZW2=PTAO*PB
       FZW3=SINH(FZW1)
       FZW4=SINH(FZW2)
       FZW=L2*(1.0+FZW3/FZW4)
C
       DRN1=1.0-FRN/R1
       DRN2=(PBATA**2)-(DRN1**2)
       DRN3=R1*DRN2*FA4
       DRN=2.0*PBATA/DRN3
C
       DRS1=1.0-FRS/R1
       DRS2=(PBATA**2)-(DRS1**2)
       DRS3=R1*DRS2*FA4
       DRS=2.0*PBATA/DRS3
C
       D2RN1=(R1**2)*FA4*(DRN2**2)
       D2RN=-4.0*PBATA*DRN1/D2RN1
C
       D2RS1=(R1**2)*FA4*(DRS2**2)
       D2RS=-4.0*PBATA*DRS1/D2RS1
C
       DZE1=(FZE/L2-1.0)**2
       DZE2=FZE4**2
       DZE3=PTAO*L2*((1.0+DZE1*DZE2)**0.5)
       DZE=FZE4/DZE3
C
       DZW1=(FZW/L2-1.0)**2
       DZW2=FZW4**2
       DZW3=PTAO*L2*((1.0+DZW1*DZW2)**0.5)
       DZW=FZW4/DZW3
C
       D2ZE0=1.0-FZE/L2
       D2ZE1=(FZE4**3)*D2ZE0
       D2ZE2=1.0+DZE1*DZE2
       D2ZE3=PTAO*(L2**2)*(D2ZE2**1.5)
       D2ZE=D2ZE1/D2ZE3
```

```
C
      D2ZW0=1.0-FZW/L2
      D2ZW1=(FZW4**3)*D2ZW0
      D2ZW2=1.0+DZW1*DZW2
      D2ZW3=PTAO*(L2**2)*(D2ZW2**1.5)
      D2ZW=D2ZW1/D2ZW3
C
      DN=C2*RN*(DRN**2)
      FN=DZ*RN*(D2RN+DRN/FRN)
C
      DS=C2*RS*(DRS**2)
      FS=DZ*RS*(D2RS+DRS/FRS)
C
      DE=C1*RBAR(I)*(DZE**2)
      FE=DR*RBAR(I)*D2ZE
C
      DW=C1*RBAR(I)*(DZW**2)
      FW=DR*RBAR(I)*D2ZW
C
      PN=FN/DN
      PS=FS/DS
      PE=FE/DE
      PW=FW/DW
C
      PPN=(1.0-0.1*ABS(PN))**5
      PPS=(1.0-0.1*ABS(PS))**5
      PPE=(1.0-0.1*ABS(PE))**5
      PPW=(1.0-0.1*ABS(PW))**5
C
      DDN=DN*(AMAX1(0.0,PPN))
      DDS=DS*(AMAX1(0.0,PPS))
      DDE=DE*(AMAX1(0.0,PPE))
      DDW=DW*(AMAX1(0.0,PPW))
C
      FFN=AMAX1(FN,0.0)
      FFS=AMAX1(-FS,0.0)
      FFE=AMAX1(FE,0.0)
      FFW=AMAX1(-FW,0.0)
C
      RETURN
      END
C
      SUBROUTINE TRIDAG(IF,L,A,B,C,D,V)
      DIMENSION A(50),B(50),C(50),D(50),V(50),BETA(101),GAMMA(101)
C
C.....COMPUTE INTERMEDIATE ARRAYS BATA AND GAMMA.....
      BETA(IF)=B(IF)/A(IF)
      GAMMA(IF)=D(IF)/A(IF)
C
      IFP1=IF+1
C
      DO 301 I=IFP1,L
         BETA(I)=B(I)/(A(I)-C(I)*BETA(I-1))
         GAMMA(I)=(D(I)+C(I)*GAMMA(I-1))/(A(I)-C(I)*BETA(I-1))
C
301   CONTINUE
C
C.....COMPUTE FINAL SOLUTION VECTOR V.....
      V(L)=GAMMA(L)
      LAST=L-IF
      DO 302 K=1,LAST
```

```
          I=L-K
          V(I)=GAMMA(I)+BETA(I)*V(I+1)
C
302     CONTINUE
        RETURN
        END
C
        SUBROUTINE FUNDR(DRI,RI,P1,PBATA,FA1,FA2,FA3,FA4)
        REAL DRI,RI,R1,PBATA,FA1,FA2,FA3,FA4
C
        FR1=FA3**(1.0-RI)
        FR2=FA2*FR1
        FR3=1.0+FR1
        FR=R1*(FA1-FR2)/FR3
C
        DR1=1.0-FR/R1
        DR2=(PBATA**2)-(DR1**2)
        DR3=R1*DR2*FA4
        DRI=2.0*PBATA/DR3
C
        RETURN
        END
C
        SUBROUTINE FUNDZ(DZJ,ZJ,L2,PTAO,PB)
C
        FZ1=PTAO*(ZJ-PB)
        FZ2=PTAO*PB
        FZ3=SINH(FZ1)
        FZ4=SINH(FZ2)
        FZ=L2*(1.0+FZ3/FZ4)
C
        DZ1=(FZ/L2-1.0)**2
        DZ2=FZ4**2
        DZ3=PTAO*L2*((1.0+DZ1*DZ2)**0.5)
        DZJ=FZ4/DZ3
C
        RETURN
        END
```

# Appendix D

# Additional Results of Numerical Modelling

## D.1 Magnitude of Electric Field Profiles

The magnitude of electric field profiles for both connection modes at various radial levels is presented in the following figures.

——— Connection mode (1): planar electrodes to power supply

- - - - - - Connection mode (2): hollow electrode to power supply

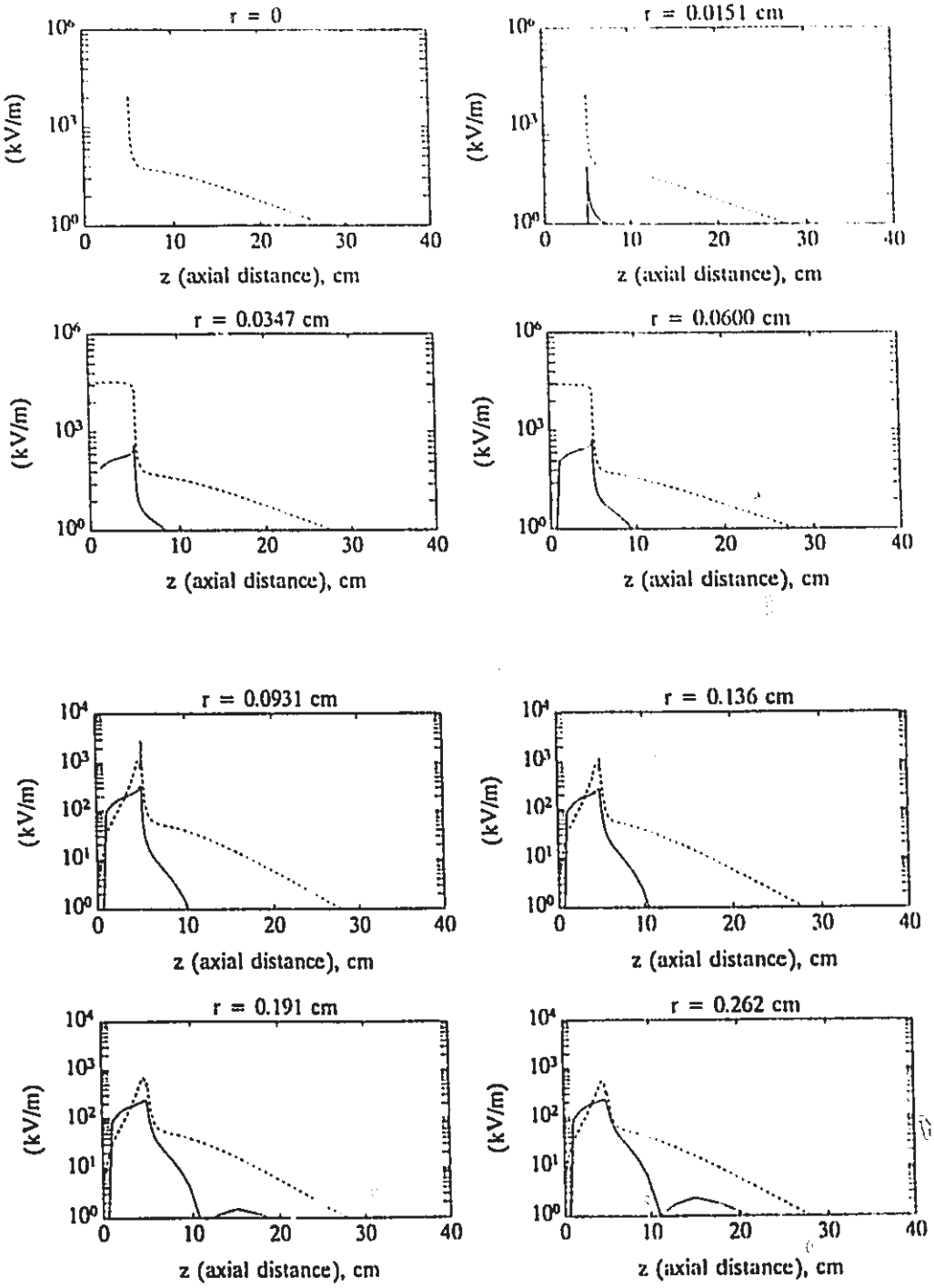
r = 0
r = 0.0151 cm
r = 0.0347 cm
r = 0.0600 cm
r = 0.0931 cm
r = 0.136 cm
r = 0.191 cm
r = 0.262 cm
(kV/m)
z (axial distance), cm

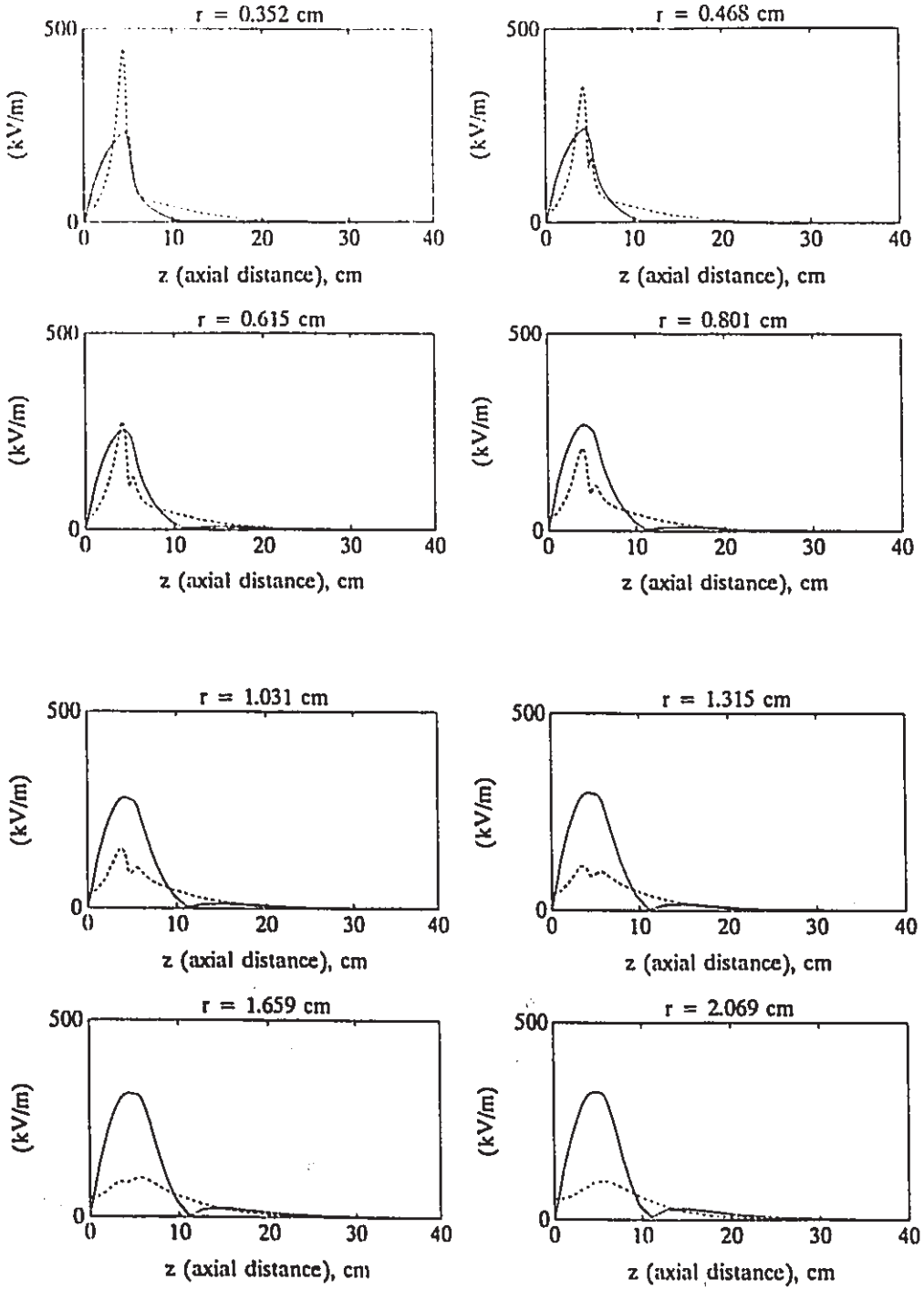
r = 0.352 cm
r = 0.468 cm
r = 0.615 cm
r = 0.801 cm
r = 1.031 cm
r = 1.315 cm
r = 1.659 cm
r = 2.069 cm
(kV/m)
500
0
0
10
20
30
40
z (axial distance), cm

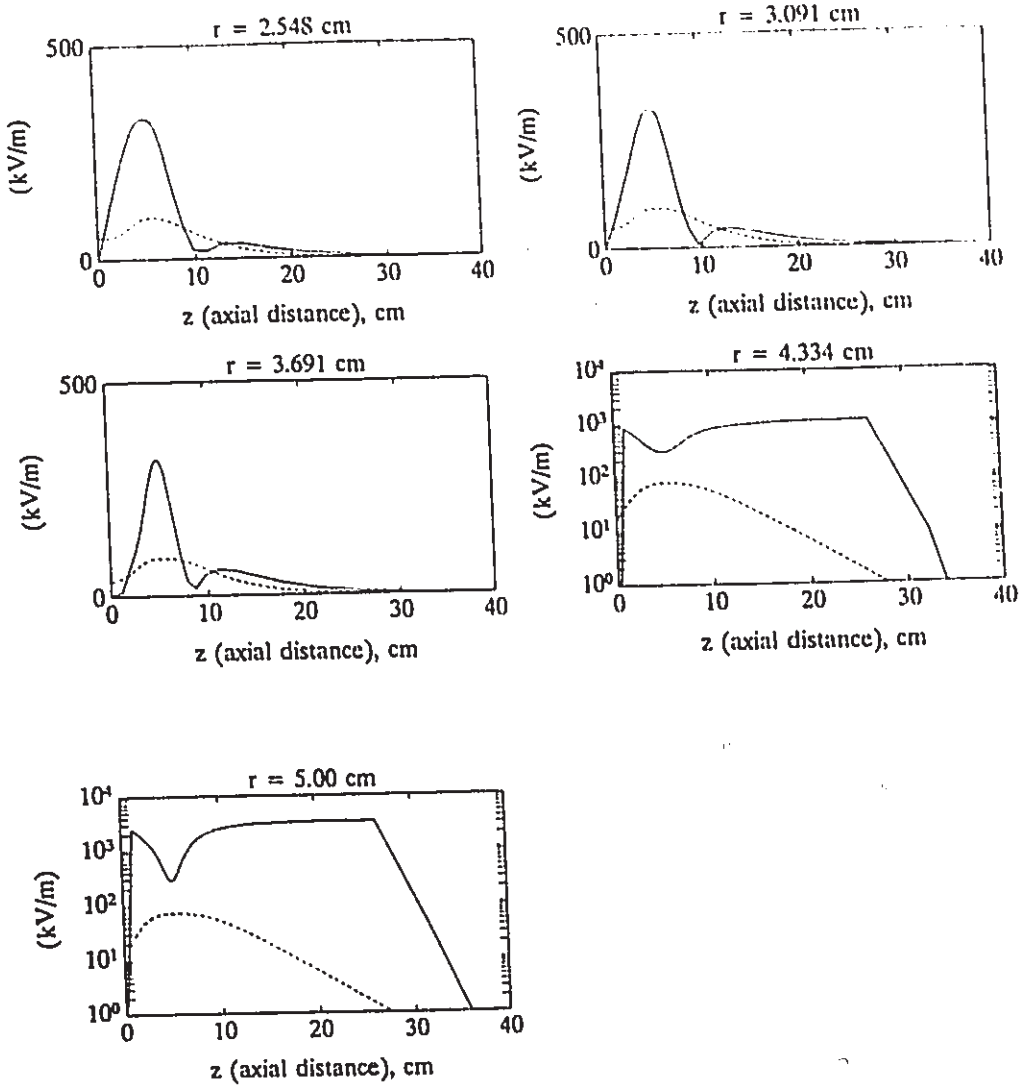
r = 2.548 cm
500
0
(kV/m)
0
10
20
30
40
z (axial distance), cm
r = 3.091 cm
500
0
(kV/m)
0
10
20
30
40
z (axial distance), cm
r = 3.691 cm
500
0
(kV/m)
0
10
20
30
40
z (axial distance), cm
r = 4.334 cm
$10^4$
$10^3$
$10^2$
$10^1$
$10^0$
(kV/m)
0
10
20
30
40
z (axial distance), cm
r = 5.00 cm
$10^4$
$10^3$
$10^2$
$10^1$
$10^0$
(kV/m)
0
10
20
30
40
z (axial distance), cm

## D.2 Magnitude of EHD Force Components—(1)

The magnitude of EHD force components profiles for connection mode (1) at various radial levels is presented in the following figures along with the gravity component (horizontal line) for comparison.

——— Electrophoretic component

- - - - - - Dielectrophoretic component

— · — · — Component of negative electric pressure gradient

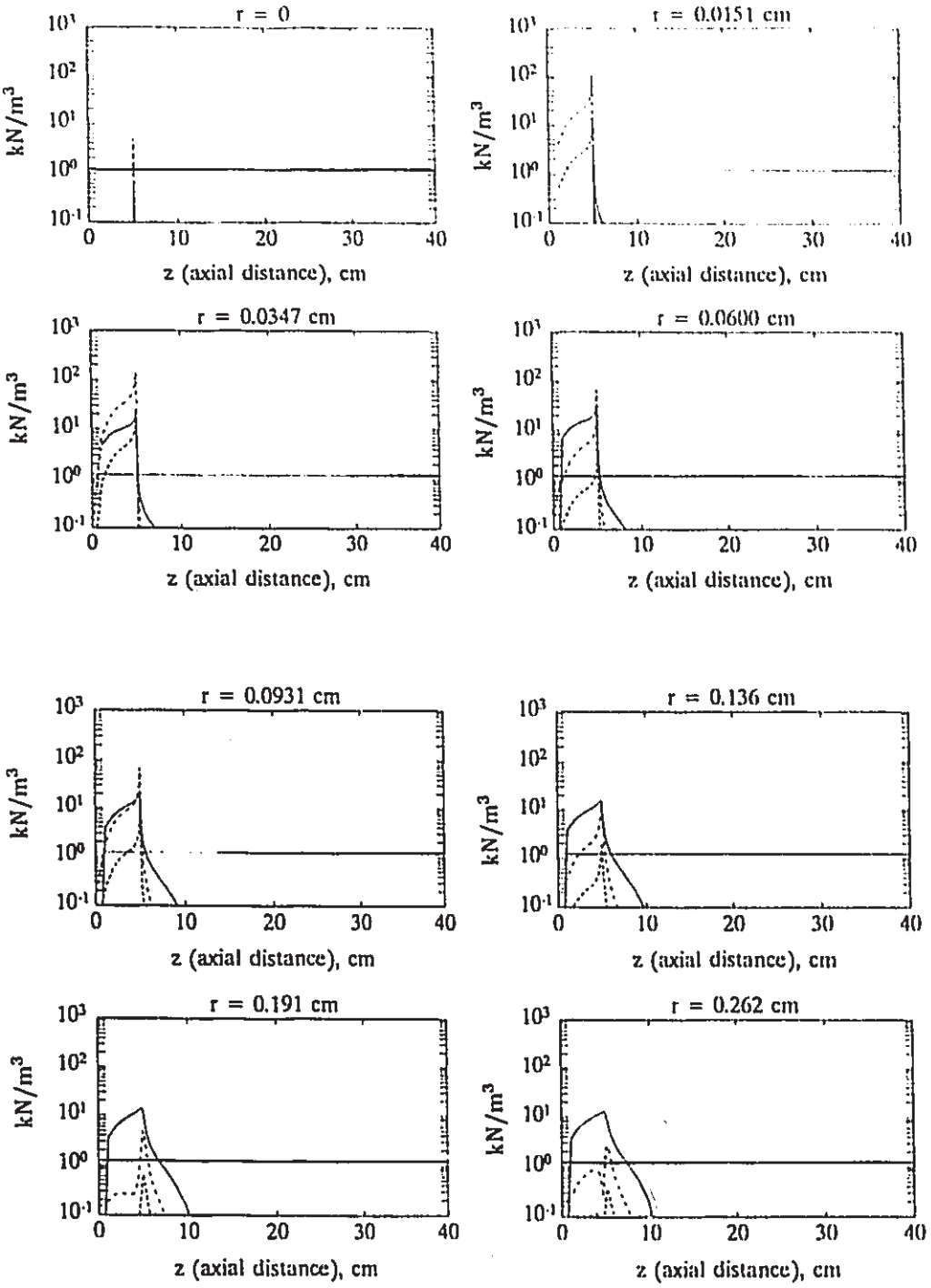
r = 0
r = 0.0151 cm
r = 0.0347 cm
r = 0.0600 cm
r = 0.0931 cm
r = 0.136 cm
r = 0.191 cm
r = 0.262 cm
kN/m³
z (axial distance), cm

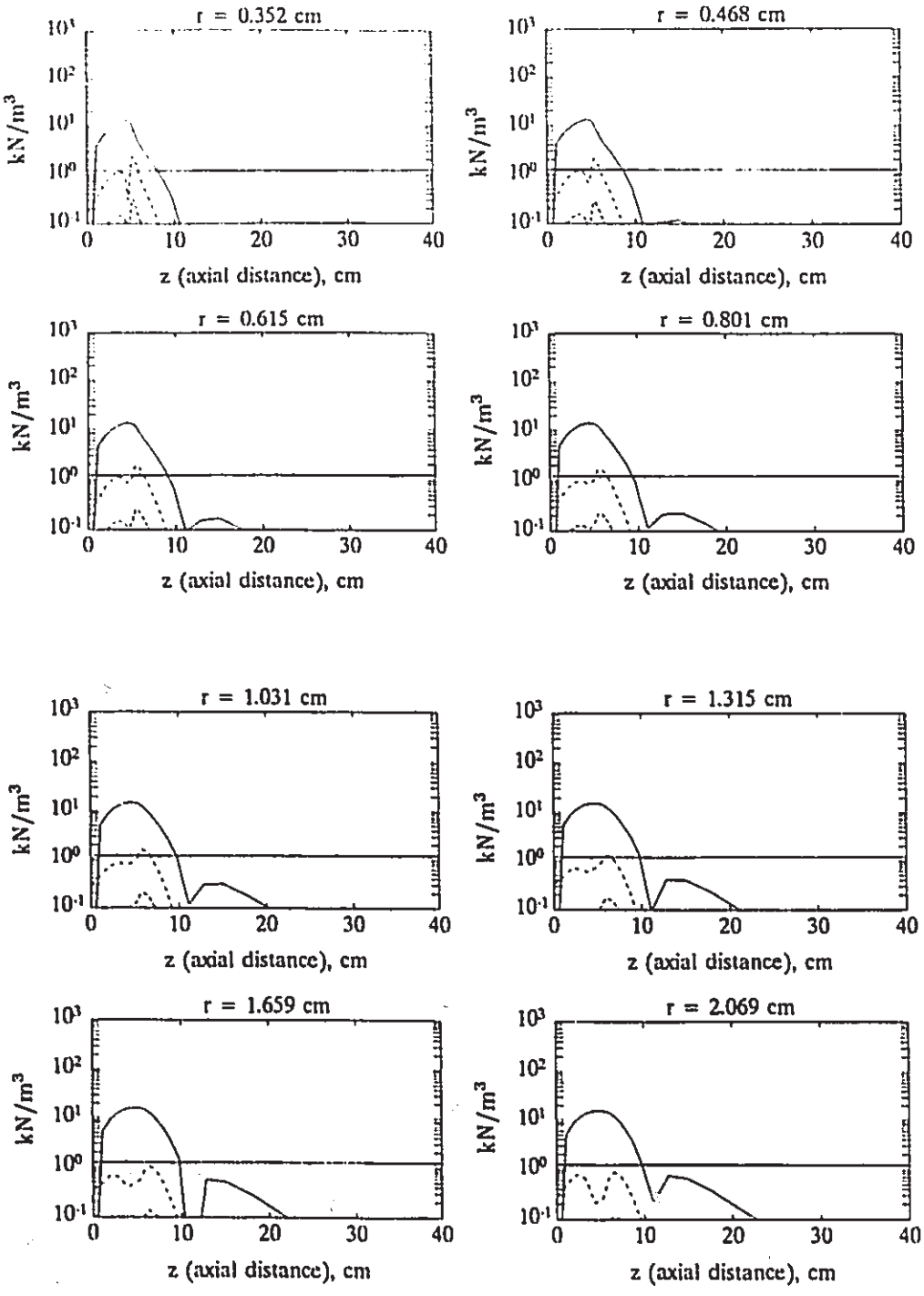
r = 0.352 cm
r = 0.468 cm
r = 0.615 cm
r = 0.801 cm
r = 1.031 cm
r = 1.315 cm
r = 1.659 cm
r = 2.069 cm
kN/m³
z (axial distance), cm

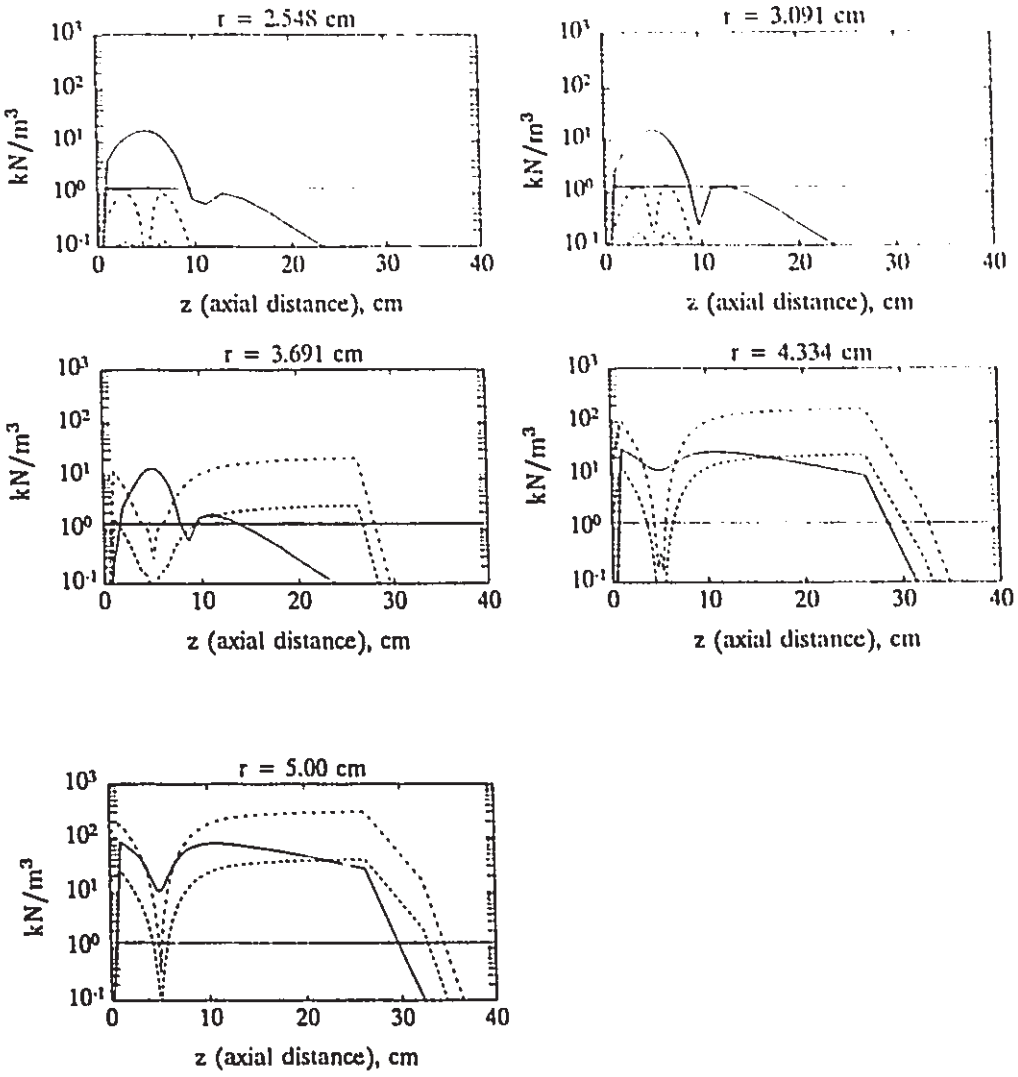
r = 2.548 cm
r = 3.091 cm
r = 3.691 cm
r = 4.334 cm
r = 5.00 cm
kN/m³
z (axial distance), cm

## D.3 Magnitude of EHD Force Components—(2)

The magnitude of EHD force components profiles for connection mode (2) at various radial levels is presented in the following figures along with the gravity component (horizontal line) for comparison.

——— Electrophoretic component

- - - - - - Dielectrophoretic component

— · — · — Component of negative electric pressure gradient

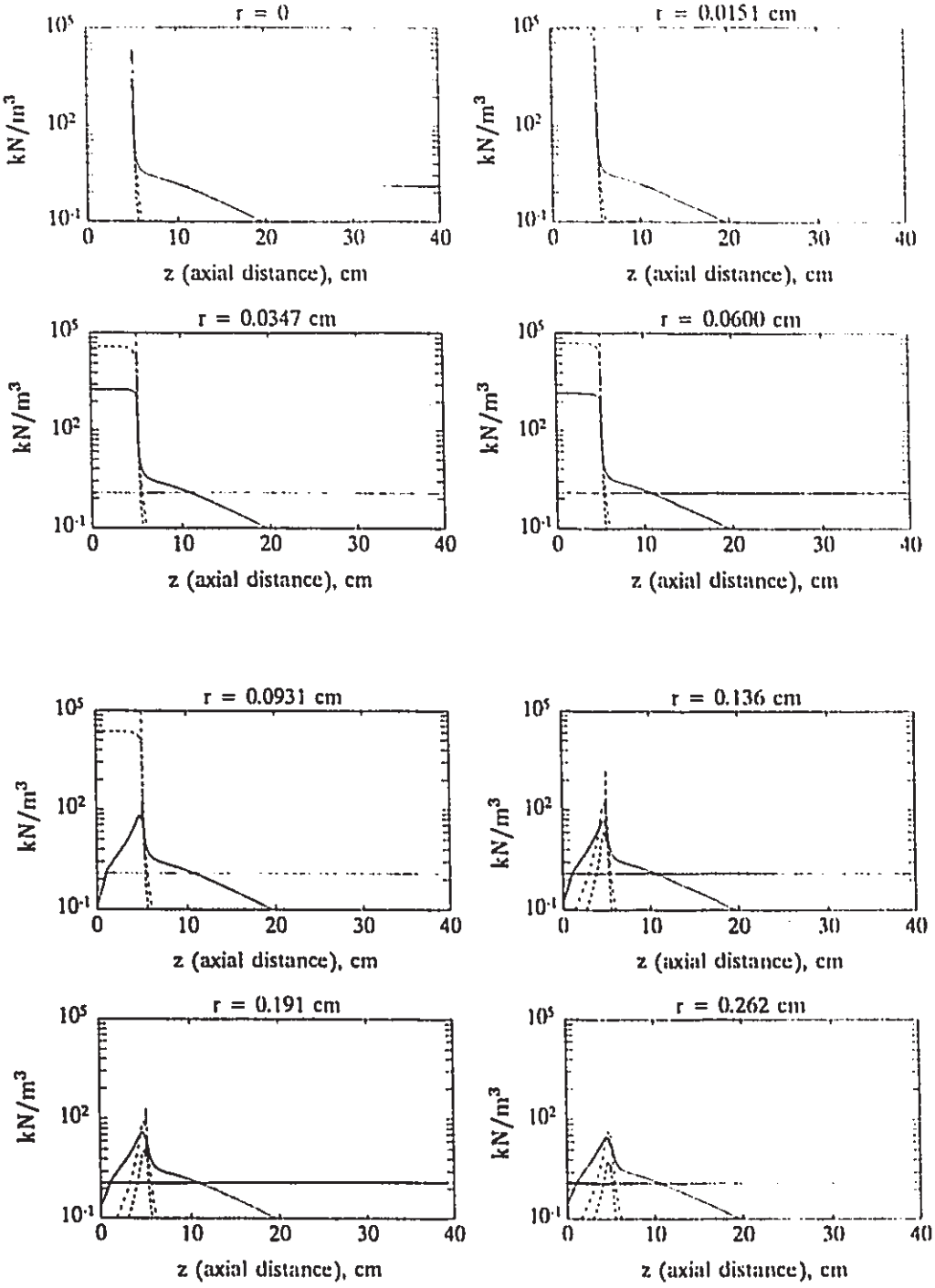
r = 0
r = 0.0151 cm
r = 0.0347 cm
r = 0.0600 cm
r = 0.0931 cm
r = 0.136 cm
r = 0.191 cm
r = 0.262 cm
kN/m³
z (axial distance), cm

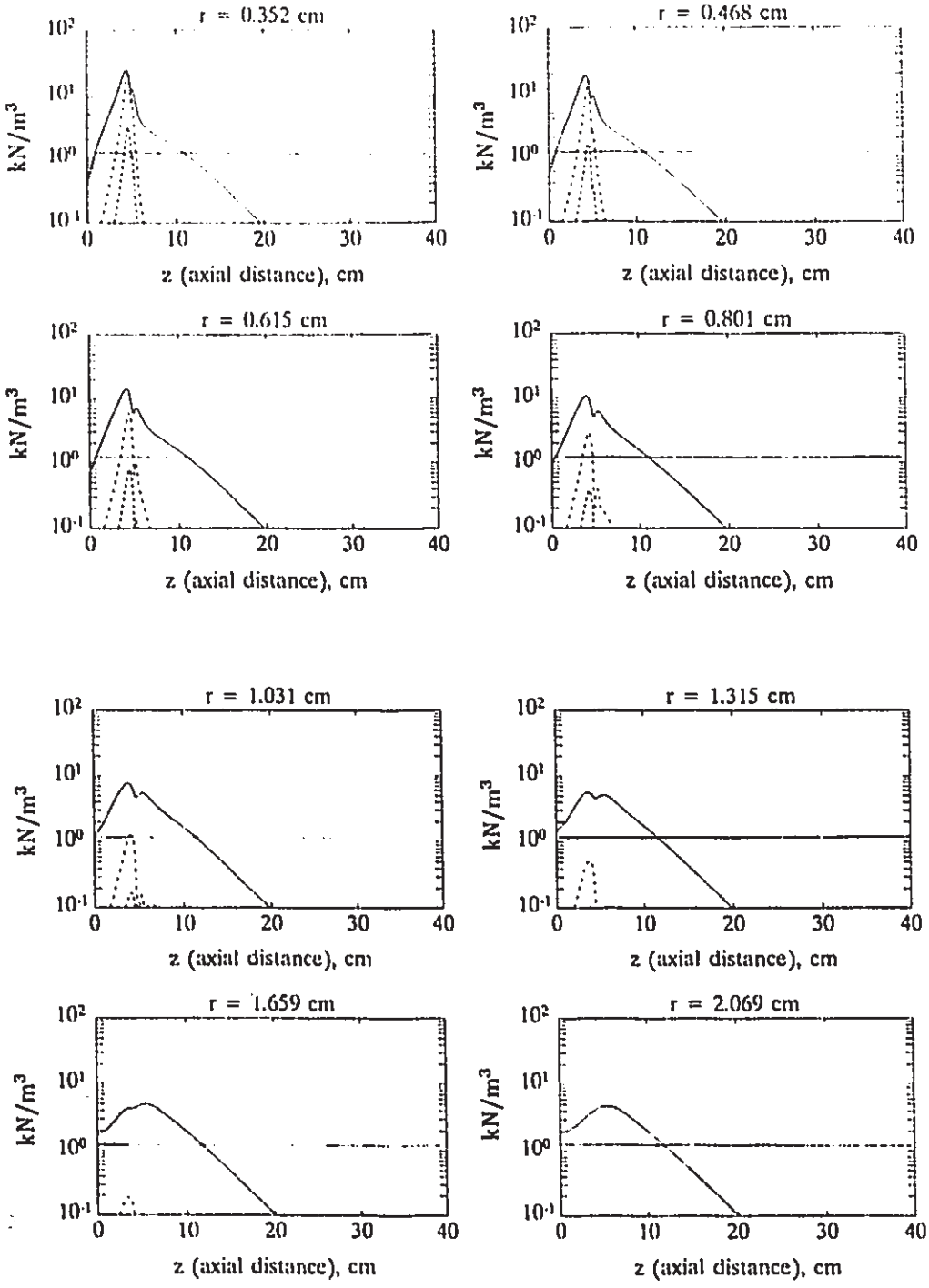
r = 0.352 cm
r = 0.468 cm
r = 0.615 cm
r = 0.801 cm
r = 1.031 cm
r = 1.315 cm
r = 1.659 cm
r = 2.069 cm
kN/m³
z (axial distance), cm

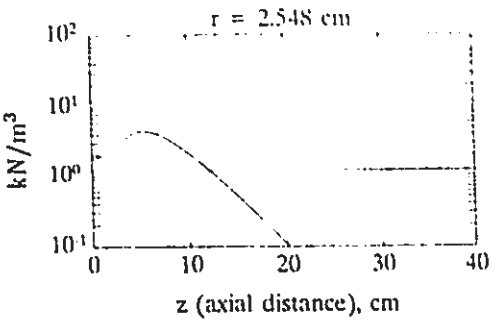
r = 2.548 cm
kN/m³
z (axial distance), cm

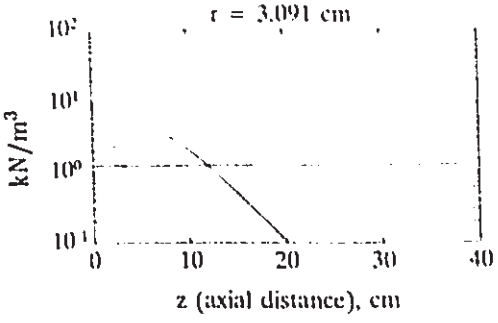
r = 3.091 cm
kN/m³
z (axial distance), cm

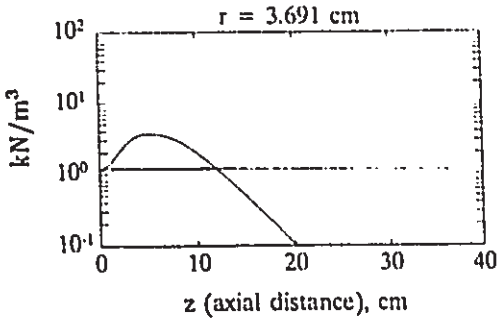
r = 3.691 cm
kN/m³
z (axial distance), cm

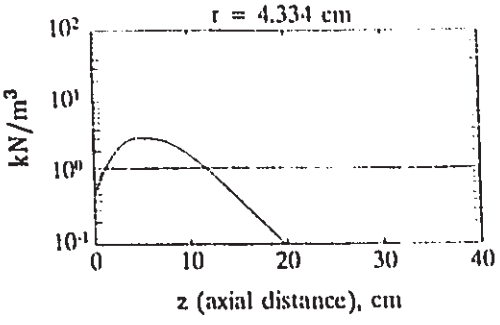
r = 4.334 cm
kN/m³
z (axial distance), cm

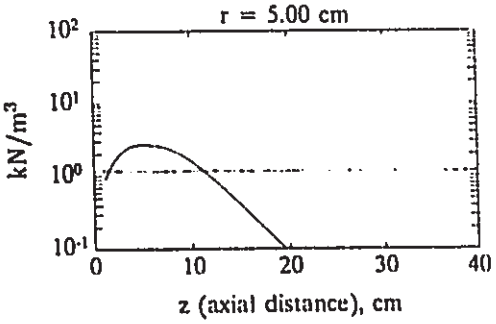
r = 5.00 cm
kN/m³
z (axial distance), cm

# Appendix E

# Contributions to Knowledge

The investigations on EHD droplet formation, dispersion and mass transfer in a viscous dielectric liquid are the main subjects of study for the potential applications of enhanced mass transfer by an imposed DC electric field in liquid-liquid extraction operations. In this dissertation several contributions to knowledge are claimed:

- Multi-droplet dispersion with uniform size can be achieved in the present work at high DC applied voltage (up to 15 kV). This provides a special feature for the potential industrial applications and also simplifies the data analysis.
- The experimental results indicate that total mass transfer efficiency can be increased by up to fourfold by an applied electric field (at 10 kV applied voltage). The increased specific interfacial area and the accelerated drop initial velocity in the presence of electric field are the main contributions to the enhanced efficiency of mass transfer performance in the present investigation.
- The effective dielectric constant has been defined as a basis for derivation of the EHD force components on a droplet. Both the "Rayleigh instability limit" model and the Vonnegut and Neubauer model have been modified successfully to evaluate the maximum charge limit on droplets in liquid-liquid systems.

Several papers and conference presentations which have been published or accepted based on this work are listed below:

W. He and J.S Chang, "Chapter 22: EHD Enhanced Mass Transfer Operations and Chemical Reactions", in Handbook of Electrostatic Applications, (J.S. Chang, A.J. Kelly and J.M. Crowley eds), Marcel Dekker, Inc., New York (1993, in press).

W. He, J.S. Chang and M.H.I. Baird, "Droplet Charge Measurement in an Electrohydrodynamic Liquid-Liquid Extraction System", Conference Record, IEEE IAS 28th Annual Meeting, (IEEE Service Centre ed.), Toronto, October 3-8, 1993 (in press).

W. He, M.H.I. Baird and J.S. Chang, "The Effect of Electric Field on Mass Transfer from Drops Dispersed in a Viscous Liquid", Can. J. Chem. Eng. **71**, 366-376 (1993).

W. He, M.H.I. Baird and J.S. Chang, "Effects of an Imposed D.C. Non-Uniform Electric Field on Liquid-liquid Mass Transfer", Proc. 42nd CSChE Annual Conference, 441-442, (CSChE ed.) Toronto, Ontario, Oct. 18-21, 1992.

W. He, M.H.I. Baird and J.S. Chang, "The Effect of Electric Field on Droplet Formation and Motion in a Viscous Liquid", Can. J. Chem. Eng. **69**, 1174-1183 (1991).

J.S. Chang, W. He, M.H.I. Baird and S. Masuda, "Development of Pulsed Travelling Wave Type EHD Powder Pump: Preliminary Results", Mater. Sci. J. **16**, 9-14 (1990).

W. He, J.S. Chang and M.H.I. Baird, "Liquid-liquid Dispersion under Pulsed Electric Fields in a Horizontal Cell", Conference Record, IEEE IAS 25th Annual

Meeting, 774–777, (IEEE Service Centre ed.) Seattle, Washington, October 7–12, 1990.

W. He, J.S. Chang and M.H.I. Baird, "Liquid Droplet Dispersion in an Insulating Fluid by EHD Techniques", Conference Record, 10th Int. Confer. on Conduction and Breakdown in Dielectric Liquids, 291–295, (P. Atten and R. Tobazeon eds.) Grenoble, France, Sept. 10–14, 1990.

W. He, "Potential Applications of Electric Field in Solvent Extraction for Nuclear Fuel Processing", Presented at the 17th Annual Student Conference of the Canadian Nuclear Association and Canadian Nuclear Society, March 27–28, 1992, Hamilton, Ontario.

W. He, M.H.I. Baird and J.S. Chang, "High Voltage Dispersion of Water in an Insulating Liquid", Presented at 29th CAGE Club Meeting, May 12–13, 1991, Hamilton, Ontario.

W. He, M.H.I. Baird and J.S. Chang, "The Effect of a Pulsed Electric Field on Droplet Formation and Motion in a Viscous Liquid", Presented at 39th CSChE Annual Conference Oct. 1–4, 1989, Hamilton, Ontario.

Regarding McMaster's policy on the ownership of intellectual property and graduate student work, it is understood that both of my supervisors, Dr. M.H.I. Baird and Dr. J.S. Chang co-own an intellectual property and copyright for the work underlying this thesis.